FACULTY OF SCIENCE
UNIVERSITY OF COPENHAGEN

Master Thesis in Geophysics

A New Ice Core Paleothermometer for Holocene and Transition

Diffusion Processes Quantified by Spectral Methods

Sebastian Bjerregaard Simonsen
Centre for Ice and Climate,
Niels Bohr Institute, University of Copenhagen

Supervisor:
Sigfús J. Johnsen

December 2008

CENTRE FOR ICE AND CLIMATE

Master Thesis

Title:	A New Ice Core Paleothermometer for Holocene and Transition
Subtitle:	Diffusion Processes Quantified by Spectral Methods
ECTS-points:	60
Supervisor:	Sigfus J. Johnsen
Name of department:	Centre for Ice and Climate Neils Bohr Institute University of Copenhagen

---

Author:	Sebastian Bjerregaard Simonsen
Date:	December 31th 2008

Abstract

Since the early 1950's stable water isotopes have been considered a temperature proxy with application in paleoclimatic reconstruction of permanently snow covered areas. In this thesis a new method of reconstructing the paleoclimatic information preserved in the isotopic records from Arctic ice cores is tested. The method is based on the definition of the differential diffusion length $\Delta\sigma^2 = \sigma^2_{^{18}O} - \sigma^2_D$. An investigation of the processes affecting the differential diffusion length is undertaken, covering the densification of firn, ice flow modelling and isotopic diffusivity in the firn and ice matrix.
Three numerical power spectra density estimation methods have been used to retrieve the differential diffusion length in 22 sections of ice from two Greenlandic ice cores, GRIP and NGRIP. None of the methods are found superior, but both Burg's algorithm and the Autocorrelation methods show promising behaviors.
The modelled and measured differential diffusion lengths form an estimate of the surface temperature at the origin of the ice core sections. The investigation of the differential diffusion length in deep sections from the NGRIP ice core shows that the temperature reconstruction based on the differential diffusion length must be limited to ice younger than about 40 kyr for the two cores. This reduces the number of ice core sections available to 12. The low number of sections limits the interpretation of the tested temperature reconstruction. However, the estimated surface temperatures are within uncertainties of paleotemperatures records derived from combined bore hole temperature and isotope profiles from the GRIP and NGRIP ice cores.

Preface

The presented thesis accounts for the final exam of a Masters Degree in Geophysics at the University of Copenhagen and covers 60-ECTS point. The study has been conducted in about a year of full time study.

A basic knowledge of mathematics and physics is required to read this thesis along with knowledge of Glaciology. If necessary terms are explained to clarify the definitions used. The abbreviations used are all summarized in the Nomenclature at the end of the thesis. All plotted time scales start at present and end at a time before present. To ease the comparison between text and plots I write that the transition into the Last Glacial follows the Holocene, despite that it is reversed in real time.
All programming has been conducted using Matlab.

Acknowledgment

I would like to thank my supervisor Sigfus J. Johnsen for the many hours of productive discussions of the problems at hand along with introducing me to the study subject. Trevor J. Popp is thanked for providing isotopic data from the NGRIP ice core and proof reading. I thank Ph.D student Hans Christian Steen-Larsen for showing interest and support for the work and proof reading, Ghita Hansen for proof reading and Lykke Pedersen for the love and support during the writing of this thesis and also for proof reading. I would also like to thank the Centre for Ice and Climate at the Niels Bohr Institute for supplying an ideal environment for working with this thesis, along with providing the opportunity to go to the NEEM drill site to experience the field work involved in drilling ice cores. Finally, my office mates deserve thanks for the productive discussions and the needed distractions.

Sebastian B. Simonsen
Copenhagen, December 2008

Preface for 2nd Edition

After handing in this master thesis December 31th 2008 a couple of errors has come to my attention. They have not been corrected in the thesis. However a list will be given here:

Page 51 : Equation (5.18) was fist described by [Johnsen et al., 2000].

Page 76 : Severinghaus et al. [1998] was not doing measurements on the GRIP ice core, but GISP2.

Equation (5.21) : On the right hand side of the equation in the denominator the subscript sam should be sec.

If further errors are found in this work I would be glad to hear about it. Send me a mail on sbs@gfy.ku.dk

Sebastian B. Simonsen
Copenhagen, February 2009

Contents

1 Introduction

In the past couple of years the climate has caught a lot of attention in the broad media picture. The global warming is on everybody's lips. Suddenly, the present warming has become a global issue. Big organizations such as the UN have turned there focus on it through the Intergovernmental Panel on Climate Change (IPCC, [IPCC, 2007]). The reason that we are talking about a global warming is due to our ability to determine the past climate, past the time scale of manmade temperature measurements. A whole science has developed around this called paleoclimatology, covering a broad range of study disciplines, e.g. tree rings, sedimentary, corals, speleotherms and ice cores. All are able to determine past climate on different time scales and time resolution. One of the most successful methods to determine the past climate for the last couple of hundred thousand years has proven to be ice cores. Depending on the site, ice cores have a climate record of different lengths; Greenland about 115 to 250 kyr[1] back in time [Dansgaard et al., 1993], and Antarctica at least 800 kyr back in time [EPICA Members, 2004]. Table 1.1 and Figure 1.1 show the ice core drilling sites in Greenland, which have reached the bedrock[2]. The first ice core was drilled by the Americans in 1966 at the Camp Century site in Northwest Greenland, [Dansgaard et al., 1969a]. After this ice core a number of cores have followed and the most resent is the NEEM ice core, which was begun in 2008, and due to reach the bedrock in the next couple of field seasons. Hopefully bringing new knowledge about the last warm period, the Eemian.

In the following chapter there is a more detailed introduction of how the climate signal is preserved in the ice. Before proceeding a number of terms must be explained in order to give a general picture of glaciology.

[1] The chronology of the very old ice may be destroyed by basal folding of the ice.
[2] The Renland ice core drilling was stopped a few meters above the bedrock.

Table 1.1: The position and length of the deep ice cores in Greenland. The length of the NEEM ice core is approximated from radar echo soundings. All shown on the Greenland map in Figure 1.1. Location reference [Dansgaard et al., 1982; Hvidberg et al., 1997; Johnsen et al., 2001; Dahl-Jensen et al., 2002; NGRIP Members, 2004; Solgaard et al., 2007].

Site (year)	Latitude	Longitude	Ice core length
Camp Century (1966)	77.2 ° N	61.1 ° W	1370 m
Dye 3 (1981)	65.2 ° N	43.8 ° W	2035 m
Renland (1988)	71.3 ° N	26.7 ° W	325 m
GRIP (1992)	72.5 ° N	37.3 ° W	3027 m
GISP2 (1993)	72.5 ° N	38.3 ° W	3053 m
Hans Tausen Ice Cap (1995)	82.5 ° N	38 ° W	345 m
NGRIP (2004)	75.1 ° N	42.3 ° W	3085 m
NEEM (2008)	77.5 ° N	51 ° W	2542 m

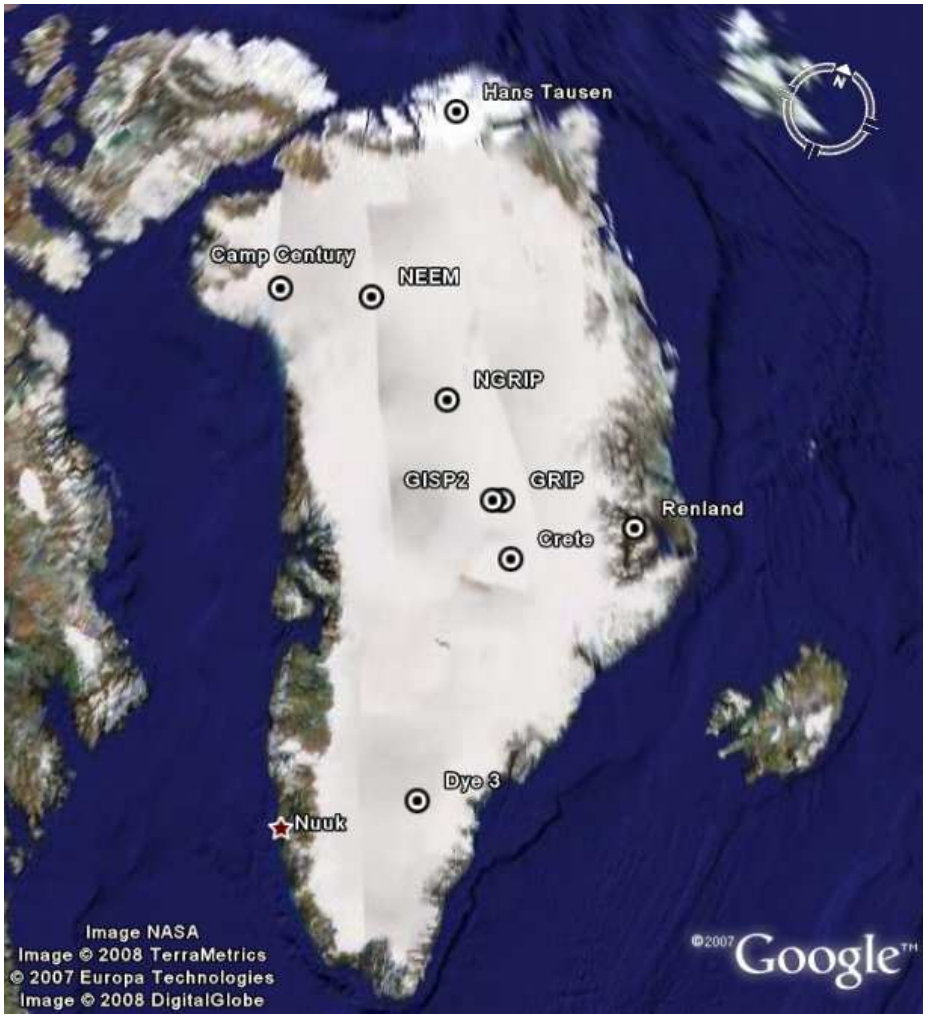

Figure 1.1: Map of the Greenland ice cores drilling sites. Listed in Table 1.1 with graphical location and depth information. The map is produced in Google Earth.

As snow is deposited on the ice sheet, the ice sheet can be divided into two main zones.

1. The accumulation zone: Here more snow is deposited than removed during the melt season, giving a net accumulation of snow each year. This zone can further be divided into a wet and a dry snow zone. The dry zone is the part of the accumulation zone which in summer does not experience melt and is often situated in the innermost parts of the ice sheet. The wet snow zone experiences some melt during summer. Surface melt water penetrates the top snow and runs off or refreezes deeper in the snow column. The refreezing happens when melt water meets an impenetrable layer.

2. The ablation zone. Here all the accumulated snow during winter is melted away or removed in calving events during summer giving a net removal of ice.

The accumulation/ablation relation gives rise to ice flow in the ice sheet, where ice moves from the accumulation zone to the ablation zone in order to have an ice sheet in steady state. The boundary between the two zones is called the equilibrium line. Due to the ice flow the surface ice gets older moving from the equilibrium line toward the margin of the ice sheet such that one could sample the ice on this transect finding a horizontal ice chronology. Whereas at the center of the ice sheet the flow can be assumed to be only vertical and the retrieved ice core samples every precipitation event of the ice sheet throughout history.
In this thesis only the dry snow zone is of interest, because the deep ice cores are located at the ice divide in central parts of the ice sheet. The snow falling here will survive each melt season. Snow which has survived a melt season is called firn and will be used frequently in the following. The firn is compressed into pure glacier ice by gravitation and as more snow is piled on year after year. This densification will be elaborated even further in Chapter 3.

1.1 Dating Ice Cores

To process the information retrieved from ice cores an accurate dating of the ice is needed. Much effort has gone into developing chronologies since the ice coring began. Concerning the Greenlandic ice cores the most comprehensive and newest dating project is called *"Greenland Ice Core Chronology 2005 "* (GICC05) which provides a common chronology for the three ice cores Dye-3, GRIP and NGRIP. The dating of these cores have been done by counting seasonally variation in different parameters. This counting has been done back to 60kyr b2k for the NGRIP core and 32kyr for GRIP. Below this depth ice flow modelling has been used to date the cores. Also other

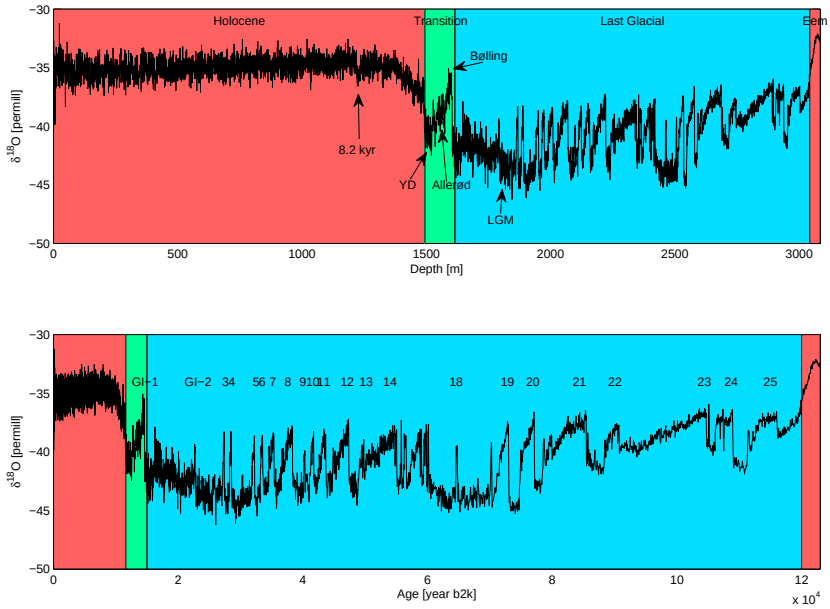

Figure 1.2: The climate proxy δ^{18}O measured in the NGRIP ice is shown both on a depth scale and on the GICC05 time scale. On the upper panel is the large scale climate periods and the lower panel shows the occurrence of the Greenland interstadials in the Last Glacial [Ditlevsen et al., 2005].

Greenlandic ice cores have been matched to this time scale using volcanic spikes in the ECM[3] record [Vinther et al., 2008b].

Figure 1.2 shows the measured δ^{18}O record of the dated NGRIP core on the GICC05 time, which reaches about 123 kyr back in time. The δ^{18}O can be considered as a temperature proxy[4]. The Holocene is the present warm period covering about half the core length. In the later chapters a lot of attention is given to the transition into the Last Glacial, which is shaded greenish in the figure. The transition is followed by the Last Glacial, also known as the late Pleistocene and the record stops at the Eemian, i.e. the last warm period about 120 kyr bp. During the glaciation rapid climate shifts are seen in the record. They are known as the Greenland interstadials (GI) starting with the Bølling/Allerød (BA) as the GI-1 and counting back to GI-25 just before the Eemian, see the lower panel of Figure 1.2. In between the GI events are the Greenland stadia (GS) starting with Younger Dryas (YD) which is located between the BA and Holocene. Two other cold periods are also highlighted in the figure; the 8.2 kyr cold event in the early Holocene and the Last Glacial Maximum (LGM).

[3]Electrical Conductivity Measurements which show the acidity of the ice [Hammer, 1980].

[4]A proxy is a parameter which acts for another.

2

Ice Cores as a Paleothermometer

This chapter introduces methods used in retrieving the paleoclimatic information recorded in arctic ice core. The main focus will be on stable water isotopes, but other methods will also be presented briefly, all used to interpret the climatic records. Classically, stable water isotopes have been of special interest to the ice core research by being a temperature proxy.

2.1 Stable Water Isotopes

In water $H_2{}^{16}O$, $HD^{16}O$ and $H_2{}^{18}O$ are the three main isotopic species, with natural abundances of 99.77%, 0.03% and 0.20%, respectively [Paterson, 2002, p. 380]. Because of the abundance of $H_2{}^{16}O$ and a stable ratio of the species in the ocean, the isotopic content of a water sample is often given as the δ-value[1] reflecting the deviation from ocean water.

$$\delta = \frac{R - R_{ocean}}{R_{ocean}} 10^3 \ \text{[‰]} \ , \tag{2.1}$$

where R is the ratio of two species $\left(\frac{^{18}O}{^{16}O} \text{ or } \frac{D}{H}\right)$ and R_{ocean} is the ratio of oceanic water. The present oceanic ratio is defined by "*Standard Mean Ocean Water*" (SMOW), which was defined by Craig [1961b] with respect to the *National Bureau of Standards reference sample 1.* An Empirical relationship between $\delta^{18}O$ and δD has been established for rivers, lakes and precipitation on the northern hemisphere as

$$\delta D = 8\delta^{18}O + 10 \ , \tag{2.2}$$

this relationship is known as the Metoric water line [Craig, 1961a; Dansgaard, 1964]. To understand the Metoric water line the processes affecting

[1] $\delta^{18}O$ and δD is used in the following as the δ-value, with respect to oxygen-18 or deuterium.

the isotopic composition of vapor from it originates in the ocean to it precipitates have to be described. The evaporation process from the ocean was described by Merlivat and Jouzel [1979], who derived the isotopic composition of the vapor δ_{v0} to be

$$\delta_{v0} = \frac{1-k}{\alpha_e(1-kh)} - 1 \ , \tag{2.3}$$

where α_e is the equilibrium fractionation coefficient of the isotopes at the ocean surface temperature, k is a parameter describing the kinetic fractionation at the ocean-air boundary and h is the relative humidity of the air mass [Johnsen et al., 1989]. The isotopic fractionation during the transport from the source area to precipitation area can be described by Rayleigh type condensation/sublimation, which is given by

$$\frac{\mathrm{d}\delta_v}{\delta_v + 1} = (\alpha - 1)\frac{\mathrm{d}w_s}{w_s} + \frac{\mathrm{d}\alpha}{\alpha} \tag{2.4}$$

$$\delta_c = \alpha\,(\delta_v + 1) - 1 \ , \tag{2.5}$$

where δ_v and δ_c is the δ-value of vapor and condensate/sublimat, respectively. α is a fractionation coefficient given by the air temperature of the air parcel, and w_s is the mixing ratio of H_2O compared to the mass of air in the parcel. Until the air parcel is cooled to -5 °C this process is happening in vapor-liquid equilibrium and $\alpha = \alpha_e$ [Johnsen et al., 1989]. As the solid phase becomes more important an additional term to fractionation coefficient in the Rayleigh condensation/sublimation has to be added to explain observations under Arctic and Antarctic conditions. Jouzel and Merlivat [1984] added a kinetic effect caused by the vapor to solid transition. This results in a kinetic fractionation constant α_k, which together with the equilibrium fractionation constant account for α in Equation (2.4) and (2.5) by

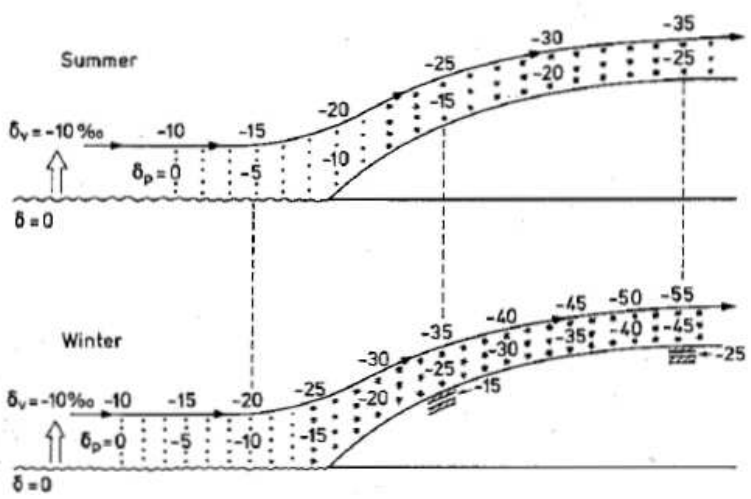

Figure 2.1: A schematic profile of $\delta^{18}O$ in Greenland in both summer and winter conditions from Dansgaard et al. [1973]. It is seen how the ocean water ration is assumed to be zero, but already in the moister transport to the clouds about 10 ‰is lost and losses continue to the deposition on the ice sheet.

the relationship

$$\alpha = \alpha_k \alpha_e \quad . \tag{2.6}$$

The kinetic fractionation constant is

$$\alpha_k = \frac{S_i}{1 + \alpha_e (S_i - 1) D_{ai}} \quad . \tag{2.7}$$

Here D_{ai} is the diffusivity of an isotopic species i in air, and will be discussed further in Chapter 5. S_i is the saturation vapor pressure for a given temperature of the ice. Hence the presented set of equations are able to account for the Metoric water line. The equations also shows the δ-values temperature dependency, which was first observed in the early 1950's. The fractionation during transport is illustrated in Figure 2.1, where an air parcel is followed from the moisture source to it is precipitating as snow on the ice sheet.

Based on the Metoric water line a measure of the non-equilibrium processes in the isotopic water cycle is defined as the deuterium excess [Dansgaard, 1964],

$$d = \delta \mathrm{D} - 8\delta^{18}\mathrm{O} \quad . \tag{2.8}$$

In ice cores, where a long climate record of the water isotopes is preserved, changes in the excess can be seen, which can be associated with climatic changes. An example is the shift from the Last Glacial to the Holocene seen in Figure 2.2, where about 20 meter of the NGRIP ice core dated to the transition is shown.

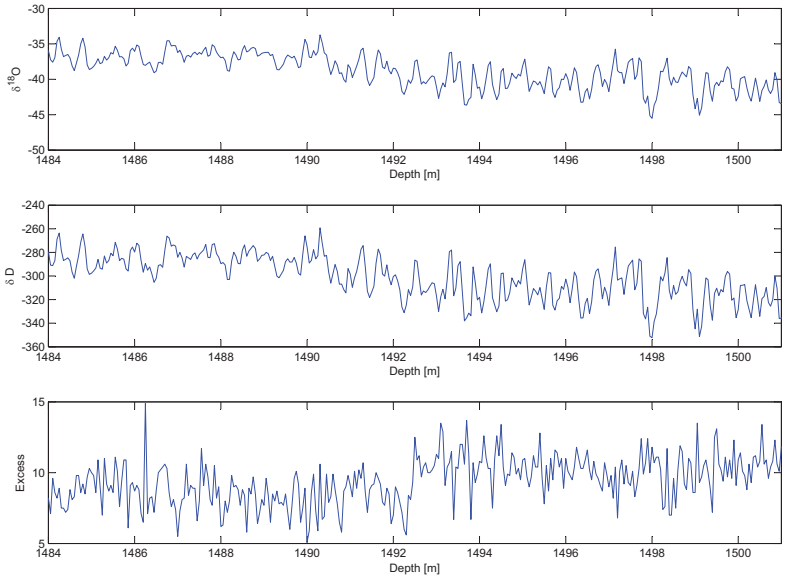

Figure 2.2: Isotopic record from the NGRIP ice core in a depth of 1484 to 1502 m. Covering the Younger Dryas, over a time span of 300 year. Note the abrupt decrease in the deuterium excess around 1492 m in the lower panel. Data from Popp [2008]

2.1.1 Temperature Proxy from Water Isotopes

From isotopic measurements of δ^{18}O in rain water collected in Copenhagen, Dansgaard [1953] noticed an increase in the δ-value during the frontal passage of a warm front. This led him to link the cloud temperature with δ^{18}O . The idea was further supported by six measurements of melted ice collected from a Greenlandic iceberg [Dansgaard, 1953], which showed a lower δ^{18}O than during the warm front passage. This work lead to an investigation of the relationship between the mean annual temperature and the δ^{18}O in permanent snow covered areas. The snow and ice of Greenland and Antarctica was of interest and samples were collected. Most of the sites were in remote locations without meteorological records. Hence the annual mean temperature was found by drilling firn cores to a depth of 15 to 40 m and measuring the temperature at this depth, thereby eliminating the annual oscillations of the temperature signal[2]. In Figure 2.3 a compilation of δ^{18}O vs. mean annual temperature (T_a) for different sites in both the Arctic and the Antarctic is shown. At sites of similar locations the relationship between δ^{18}O and temperature is linear. The results from the inland Greenland sites were published by Dansgaard et al. [1969b], which gave the linear approximation to the data as

$$\delta^{18}\mathrm{O} = (0.64 \pm 0.01)T_a - (15.0 \pm 0.1)[‰] \ . \tag{2.9}$$

The temperature dependency of the isotopic fractionation is governed by the equations described in the previous paragraph. As the air cools the heavy isotopes are removed and the δ-value is lowered. Typical values for present day Greenland are shown in Figure 2.1. Note how the source area is assumed to be the same but the temperature gradient is changing from summer to winter, which gives lower values of δ at the site of precipitation in winter. The slope of the linear relationship $a = \frac{\mathrm{d}\delta}{\mathrm{d}T_a}$ is effected by multiple factors [Boyle, 1997; Werner et al., 2001; Huber et al., 2006]; 1. Seasonally distribution of precipitation: If for example more of the snow falls in the winter, the temperature measured in the isotopes would be biased to this season because it records the temperature during precipitation events. 2. Changes of isotopic composition of the ocean: During glacial conditions with more water bound in glaciers and ice sheets, the R_{ocean} would be greater. 3. Change of source region: This will influence the distance and thereby the fractionation. All of these effects could have changed over various time scales. Thus the relationship shown in Equation (2.9) can only be used during present climate conditions and not as a universal relationship during all climate periods. Borehole temperatures from Johnsen et al. [1995] have been used to estimate a during glacial condition and thereby calibrating the isotope paleothermometer.

[2] See Chapter 5 for temperature relations in the firn collum.

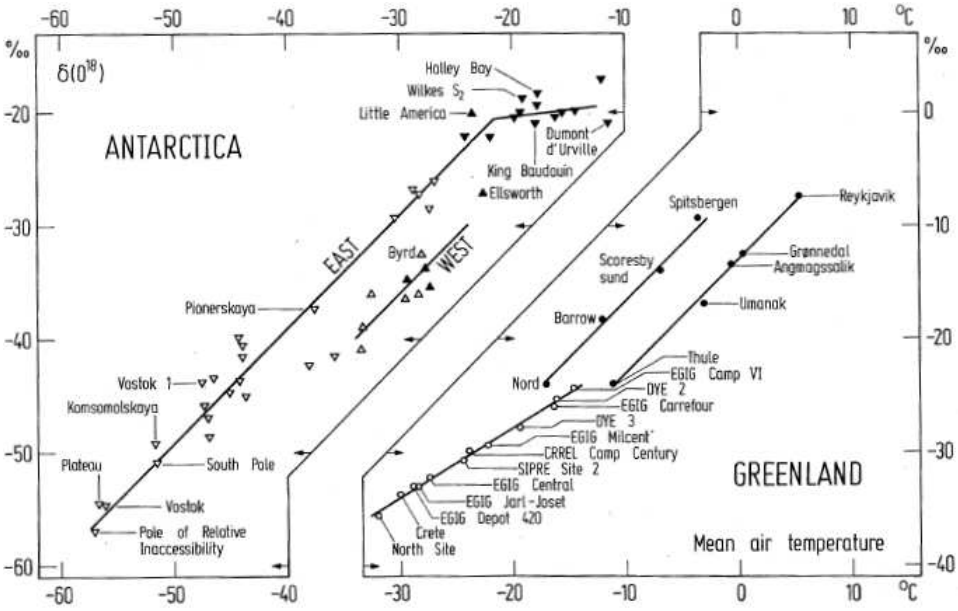

Figure 2.3: The δ^{18}O is depicted against the ten meter temperature giving an estimate of the annual mean temperature. Striking is the correlation between the two when comparing sites of similar geographical location. Addopted from Dansgaard et al. [1973].

When calculating the isotopic fractionation from the kinetic Rayleigh condensation/sublimation model a change in source or site temperature gives rise to either an increase or decrease in the δ-value. It has been shown, for example, by Masson-Delmotte et al. [2005] that δ^{18}O is more connected to the site temperature than source temperature. Whereas deuterium excess is coupled to the moisture source temperature. Having established δ^{18}O as a temperature proxy at sites on the ice sheet, the record can in theory now reconstruct past climate at the ice core site. However, a number of effects and uncertainties is affecting this temperature proxy.

Source of precipitation: The isotopic ratio is dependent on the source as seen above. Hence a change in source will give an effect in the δ-value which is not related to the temperature at the site. Charles et al. [1994] showed a 7 ‰ increase in δ^{18}O if the source area shifts from a pure North Atlantic source to and mixture of both Pacific and North Atlantic sources responsible for the precipitation ending up on the Greenlandic ice sheet. This is an extreme situation [Jouzel et al., 1997], but it shows how the source area can have an influence on the δ-value measured in an ice core, which is not related to the temperature at the ice core site.

Isotopic ratio of oceanic water: The δ-value is by definition compared with the oceanic water, i.e an assumption of a constant isotopic ratio of oceanic water. Although one can think of a number of situations changing the oceanic ratio for example during glaciation large amounts of water are allocated to the ice sheets on land. Hence the δ_{ocean}-value increases. Methods have been developed to estimate the δ_{ocean}-value

back in time using deep sea sediment cores. The estimate is that the δ_{ocean}-value changed 1.2-1.8 ‰ during the transition from Glaciation to Inter-Glaciation [Shackleton and Opdyke, 1973; Lauritzen and Lundberg, 1999].

Precipitation temperature: Because the δ-value is only recorded during precipitation events, a temperature reconstruction only reflects a weighted temperature of the precipitation events and not a mean annual temperature [Huber et al., 2006].

Seasonality: A change in the seasonality of precipitation will change the temperature that the δ-value reflects and thereby bias the measurements. If more snow is deposited during winter the annual mean temperature will seem lower than it actually is.

Cloud-surface temperature: Over the polar ice sheets an inversion layer is formed during precipitation in winter [Jouzel et al., 1997]. This gives rise to a warmer cloud temperature than normal compared to the surface temperature, and thereby biasing the correction between surface and cloud temperature. This inversion is also believed to have been stronger during the Glaciation. Hence the present correction factors can not be used to estimate the temperature relationship to past climate situations [Jouzel et al., 1997]. GCM's can shed some light to this problem.

Deposition noise: Snow drift is accounting for stratigraphic noise in the ice core record [Fisher et al., 1985], by either adding or removing snow from the drill site. In extreme cases one can imagine a whole precipitation event to be removed from the record, or the formation of a sastrugi can add precipitation to the ice core. Thereby the temperature is weighted by wind driven events.

Snow processes and ice flow: Both the diffusion of the isotopic signal and the flow of the ice can alter the isotopic signal. For example if ice from higher altitudes flows into the ice core the recorded temperature from the isotopes will seem colder than actually observed at the drill site. Flow models of the ice coring sites can estimate these effects. Also the diffusion of the isotopes alters the isotopic signal, but the diffusion has been modelled in a couple of different ways ending up with almost the same result [Johnsen, 1977; Whillans and Grootes, 1985; Johnsen et al., 2000], and is believed to be understood and thereby to be corrected for.

Ice sheet evolution: Changes in the elevation of the drill site will bias the measurements and either result in an increase or decrease in the measured signal.

The above uncertainties are recognized and can be corrected for in the record. Other methods have been developed to estimate past temperature from ice cores. In the following section some of these methods are presented.

2.2 Other Methods

Other methods have been applied in ice core research to estimate the past temperature independently or to act as calibration and validation of the isotope temperature reconstruction.

2.2.1 Borehole Inversion

The surface heat is propagated down into the ice by heat diffusion and advection. Thereby the ice has a memory of past surface temperatures. Johnsen et al. [1995] modelled the measured borehole temperature profile to constrain the temperature estimate from δ^{18}O deriving a combined isotope borehole temperature reconstruction. The borehole temperature profiles have also been used to estimate paleoclimate independent of the isotopic signal. By combining both a heat transport and ice flow as a forward model Dahl-Jensen et al. [1998] calculated the solution to the inverse problem of predicted paleotemperatures from temperature measurements from the GRIP and DYE-3 boreholes using Monte Carlo methods. This gives an independent method of resolving past surface temperatures at a drill site. Borehole inversion is not able to resolve high frequency climate events in the ice core record [Jouzel et al., 1997]. The temperatures modelled by Dahl-Jensen et al. [1998] have a growing uncertainty further back in time. The estimate for LGM is a surface temperature 23 ± 2 K lower than present, but the warming during Bølling/Allerød[3] is not resolved in the inversion.

2.2.2 Melt Layer Analysis

The occurrence of melt layers can be used as an empirical calibration of the isotopic temperature. The high altitude ice cores in Greenland are compared with sites at lower altitudes and higher temperature. Thereby estimates can be made on how much higher the surface temperature is to a given time by the frequency of the melt events. This estimate is only valid for summer temperature, where the melt occurs [Jouzel et al., 1997].

2.2.3 Accumulation Change

The accumulation patterns over the ice sheet are also temperature dependent. By knowing the past accumulation one can empirically estimate the

[3]Bølling/Allerød is starting 14691 ± 1.5 years b2k and ending 11704 ± 1.5 years b2k, seen in the deuterium record from GRIP and NGRIP ice core [Steffensen et al., 2008].

temperature in the same manner as in the melt layer analysis.

2.2.4 Gas Isotopes

The fascination of the gas isotopes $\frac{^{15}N}{^{14}N}$ and $\frac{^{40}Ar}{^{36}Ar}$ found in the atmospheric air trapped in the ice cores have been used to estimate paleoclimate and also to calibrate the water isotopes temperature reconstruction [Jouzel, 1999].

2.3 Outline of a New Palaeothermometer

To strengthen the paleotemperatures derived from ice cores, a new method is needed to estimate the surface temperature back in time at the drill site and verify the isotope temperature reconstruction. A large data set from mass spectrometer measurements of water isotopes is at hand from ice cores previously used to make temperature reconstruction from primarily δ^{18}O. It would be a shame to neglect these data and the aim of this thesis is to test the method outlined by Johnsen et al. [2006][4]. In 2006 data was not available to test the method and establish a new ice core paloethermometer relying on differential diffusion was not possible.
When snow is deposited in the dry snow zone the seasonal isotopic signal is diffused in the firn column. This diffusion process is temperature dependent. If the diffusion process can be fully understood one can hope to estimate the firn temperature from the difference in the diffusion of the two water isotopes. To understand the signals retrieved from ice cores a broad knowledge of glaciology, including firn densification, ice flow, temperature propagation in firn and ice and isotopic diffusion is needed. The estimation of the diffusion parameters is also an essential part of the temperature reconstruction. All of these subtopics will be discussed in the following chapters and pieced together to test the temperature reconstruction based on diffusion processes in Greenlandic ice cores.

[4]The idea of estimating temperatures from the difference in the diffusion of δ^{18}O and δD was presented by Johnsen et al. [2006] at the European Geosciences Union General Assembly in 2006, but no further publication has been published on the subject.

3

Densification of Firn

In the dry snow zone the snow is compressed into ice in the firn column. Depending on temperature and accumulation rate the firn is covering a depth of about 70 m to a couple of hundred meters.
During the densification three stages can be identified [Herron and Langway, 1980; Arnaud et al., 2000]. The mechanisms behind the densification are not understood in detail, but the broad picture is believed to be understood. Densification in the first stage is considered to be in the structural regime settling and packing of the grains. The first stage covers snow densities down to a critical density $\rho_c = 550\ \frac{\text{kg}}{\text{m}^3}$. The critical density was first identified by Benson [1969], who was looking at density data from polar regions. The temperature gradient is the driving factor for the packing and sintering in this stage [Arnaud et al., 2000]. The second stage is down to the pore close-off depth where air is inclosed in cylindrical pores. At this stage and below this stage the firn can be considered isothermal because the seasonal temperature signal is absent. During the third and final stage the trapped air is further compressed into spherical bubbles until the density reaches the density of glacial ice $\rho_{ice} = 917\ \frac{\text{kg}}{\text{m}^3}$.
In the following two methods of modelling the densification of firn will be presented. The first is a physical model trying to understand processes of densification by applying models terminology from powder metallurgy, which is comparable with firn densification, but just on different time scales. The second approach, is to look at observations of firn densification from polar regions and make an empirical model, based on simple physical assumptions, which fits these observations.

3.1 Densification by the Arnaud-model -A Physical approach

To understand the physics behind firn densification Arnaud et al. [2000][1] included two processes to explain the stages: Grain boundary sliding derived by Alley [1987] and the geometrical approach of densification by power law creep used in powder metallurgy by Arzt [1983].
Looking at a microscopic scale the geometric approach describes pressure sintering of each spherical grain and the increase in contact area between grains, which can be adapted for the top part of the firn where the grains are compressed together do to grain boundary sliding. The increased contact area is described in the densification by [Alley, 1987],

$$\frac{\mathrm{d}\rho_{rel}}{\mathrm{d}t} = \frac{2}{15}\frac{\lambda r_g}{\nu r_b^2}\frac{P}{\rho_{rel}^2}\left(1-\frac{5}{3}\rho_{rel}\right) \text{ for } \rho_{rel} < 0.6 \ , \tag{3.1}$$

where ρ_{rel} is the density relative to ice, P is the pressure of the load from the above snow and atmosphere, λ is the linear-viscous grain bond thickness, ν is the viscosity of grain boundaries, r_g is grain radii and r_b is bond radii. The ratio between the grain radii and the bond radii can be assumed to be $r_b = 0.65 r_g$ [Alley, 1987].
In the second stage the grain sliding becomes negligible and the densification is controlled by power law creep given by Glen's flow law and following Arzt [1982] the geometrical approach gives the relation

$$\frac{\mathrm{d}\rho_{rel}}{\mathrm{d}t} = 5.3 A_{cr}\left(\rho_{rel}^2\rho_{rel_0}\right)^{\frac{1}{3}}\left(\rho_{rel}-\rho_{rel_0}\right)^{\frac{1}{2}}\left(\frac{P^*}{3}\right)^n \text{ for } 0.6 < \rho_{rel} < 0.9 \ , \tag{3.2}$$

where ρ_{rel_0} is the density at which the area of each grain contact is assumed to be zero, given empirically by $\rho_{rel_0} = 0.0026T + 0.03$, $P^* = \frac{4\pi P}{aZ(\rho_{rel})\rho_{rel}}$, A_{cr} is the creep constant listed in Paterson [2002, Table 5.2] for the stress exponent $n = 3$, a is the average contact area of the grains in units of r_g^2 which was approximated, in a case study of pressure sintering of polar firn by Arzt [1983],

$$a = \pi(\rho_{rel} - \rho_{rel_0})r_g^2 \ , \tag{3.3}$$

and $Z(\rho_{rel})$ is the average number of bonds per grain,

$$Z(\rho_{rel}) = Z_0 + C\left[\left(\frac{\rho_{rel}}{\rho_{rel_0}}\right)^{1/3} - 1\right] \ , \tag{3.4}$$

where $Z_0 = 7.3$ is the initial number of bounds and $C = 15.5$ is the slope of the radial distribution function for random packing of particles [Arzt, 1983].

[1] The model is an improvement of the Pimienta-model presented in English by Barnola et al. [1991]. The model of Arnaud et al. [2000] is denoted the Arnaud-model in the following.

At the pore close-off the air is assumed to be trapped in cylindrical pores in the firn. To compress the firn further the air pores must be compressed into the smallest possible spherical bubbles. This third and final stage can further be subdivided into two stages. 1. The deformation of the cylindrical pores to spherical bubbles which is from $0.9 < \rho_{rel} < 0.95$. given by

$$\frac{\mathrm{d}\rho_{rel}}{\mathrm{d}t} = \frac{3A_{cr}}{2}\left(\frac{\rho_{rel}(1-\rho_{rel})}{(1-(1-\rho_{rel})^{\frac{1}{n}})^n}\right)\left(\frac{3P_{eff}}{2n}\right)^n \tag{3.5}$$

[Arzt, 1983; Arnaud et al., 2000]. 2. The compression of the spherical bubbles from $0.95 < \rho_{rel} < 1$, where n is equal to 1 simplifies Equation (3.5) to

$$\frac{\mathrm{d}\rho_{rel}}{\mathrm{d}t} = \frac{9}{4}A_{cr}(1-\rho_{rel})P_{eff} \ . \tag{3.6}$$

P_{eff} is the effective pressure in the enclosed air bubbles, meaning the pressure of the load minus the pressure in the pores [Arnaud et al., 2000]. The densification process described by the model is depicted in Figure 3.1, based on estimated parameters from the NGRIP site.

3.2 Densification by the Herron-Langway-model -A Semi-empirical approach

Herron and Langway [1980] made a semi-empirical model of firn densification based on observations from both Greenland and Antarctica and will in the following be referred to as the HL-model. The aim of the model is to describe the first two stages, defined in the chapter introduction, using only the 10 meter temperature and the accumulation at a given site, which compared to the Arnaud-model is a simple parametrization. The restriction of covering only the first two stages is due to a lack of data at the time the model was presented. Later observations have shown that the equations governing the second stage also can be used to explain the densification in the final stage. Assuming the stress due to the overlaying snow is linearly related to the proportional change in air space in the firn, given by

$$\frac{\mathrm{d}\rho}{\rho_{ice}-\rho} = C\rho\mathrm{d}h \ , \tag{3.7}$$

where ρ is the density of firn, C is a constant and h is the depth. It is assumed that the change in depth of a layer in time is constant

$$\frac{\mathrm{d}h}{\mathrm{d}t} = \frac{A}{\rho} \ , \tag{3.8}$$

where A is the accumulation in water equivalent. Combining Equations (3.7) and (3.8) for the two stages by allowing two different constants in (3.7), the

temperature and accumulation dependency can be separated as

$$\frac{\mathrm{d}\rho}{\mathrm{d}t} = k_0 A^a \left(\rho_{ice} - \rho\right) \text{ for } \rho < \rho_c \ , \tag{3.9}$$

and

$$\frac{\mathrm{d}\rho}{\mathrm{d}t} = k_1 A^b \left(\rho_{ice} - \rho\right) \text{ for } \rho > \rho_c \ . \tag{3.10}$$

The constants a and b can be determined by comparing sites with different accumulation and are found to be [Herron and Langway, 1980],

$$a = 1.1 \pm 0.2 \text{ and } b = 0.5 \pm 0.2 \ . \tag{3.11}$$

k_0 and k_1 are determined by Arrhenius plots and are dependent on temperature

$$k_0 = 11 \exp\left(-\frac{10160}{RT}\right) \text{ and } k_1 = 575 \exp\left(-\frac{21400}{RT}\right) \ , \tag{3.12}$$

where R is the gas constant and T is the annual mean temperature in kelvin [Herron and Langway, 1980]. For Greenlandic sites later studies have shown a correction factor has to be multiplied to k_0 and k_1 of 0.85 and 1.15 respectively, to fit data [Johnsen, 2008].

3.3 Comparison of the Two Models

In Figure 3.1 the two models are plotted for present day conditions at the NGRIP drill site. The figure can be used to compare the calculated densities

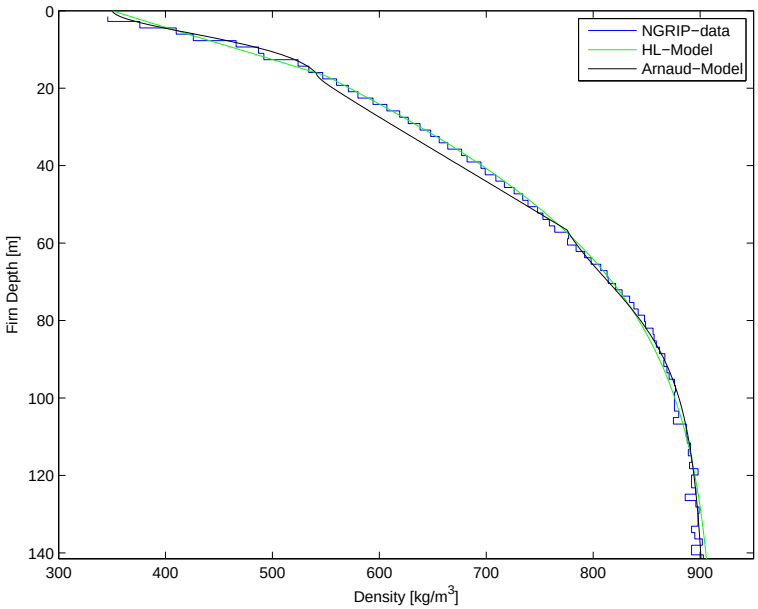

Figure 3.1: The measured density at NGRIP and a parameterizations of the two models have also been plotted. For the Arnaud model have the final stage been calculated using only Equation. (3.6) in consensus with Arnaud et al. [2000] who proposed to apply one of the two equations given depending on which one is fastest at the modelled site. The values not mentioned in the texts are chosen in accordance to Alley [1987]. NGRIP data was provided by Johnsen [2008].

with those observed in the dry snow zone of the Greenlandic ice sheet. The Arnaud-model fits data rather well in both stage 1 and 3, but it is clearly underestimating the density in the second stage. When compared to the observed densification from NGRIP the linear shape of the second stage predicted by the Arnaud-model is not able to assemble the curvature of observed densification at this stage. The misfit of the model may be ascribed to the approximated values of the average contact area of the grains and the number of bonds per grain, which seem not to have been estimated correctly. Contrarily the simple semi-empiric HL-model is able to fit the observed densification with great precision throughout the firn column and must be acknowledged as the best of the two. Further improvement of the HL-model could be to apply temperature fluctuations in the firn in Equation (3.12) as suggested by Zwally and Jun [2002]. For simplicity only the annual mean temperature will be used in this thesis when calculating the densification. Implementations of the Arnaud-model is of interest for further work, because the Arnaud-model provides a physical understanding of the processes involved in densification of firn, but loses in the complexity of the many parameters needed.

4 Models of Ice Flow

Ice flow is an important parameter in correcting isotopic data measured in ice cores. Especially in the proximity of the ice core drill sites, much effort has gone into modelling the ice flow of the ice sheets. In order to constrain the accumulation record the accumulation has been constrained by the δ^{18}O signal in models, e.g by Johnsen et al. [1995] and Buchardt and Dahl-Jensen [2007]. In this chapter a simple flow model for the NGRIP ice core is developed and compared to observed data using Monte Carlo methods to determine past accumulation and strain rates. These are both needed to estimate past temperature from isotope diffusion measured in ice cores. The model is independent of the δ^{18}O as an input parameter for the Monte Carlo simulation to determine the accumulation and the only data input to the model is radar echo layers dated by the GICC05 annual layer counting. Therefore the model is not biased by the isotopes, but the uncoupling of the model from the isotopes makes the model more computer demanding. To limit the computational demand the time resolution of the proposed model has been minimized.

4.1 Flow in Firn

Assuming steady state the flow in the firn column is derived from the continuity equation in a cartesian coordinate system. The continuity equation of a cube with the side lengths $\delta x, \delta y, \delta z$, the density ρ and velocity components u, v, w following a layer down into the firn matrix is given by [Paterson, 2002, p. 255]

$$\frac{\partial(\rho u)}{\partial x} + \frac{\partial(\rho v)}{\partial y} + \frac{\partial(\rho w)}{\partial z} = 0 \ , \tag{4.1}$$

restricting the flow to only two dimensions. The change in vertical velocity can be isolated by assuming horizontal isodensity in the layers

$$\begin{aligned} \frac{\partial w}{\partial z} &= -\frac{w}{\rho}\frac{\partial \rho}{\partial z} - \frac{\partial u}{\partial x} \\ &= -\frac{1}{\rho}\frac{\partial \rho}{\partial t} - \frac{\partial u}{\partial x} \end{aligned} \tag{4.2}$$

By looking at the vertical deformation of a firn layer having thickness λ the vertical strain rate is defined as [Hooke, 2005, p. 265]

$$\dot{\varepsilon}_z = \frac{1}{\lambda}\frac{\mathrm{d}\lambda}{\mathrm{d}t} \ , \tag{4.3}$$

Under stable accumulation conditions the layer of annual accumulation must have the vertical velocity

$$w = \frac{\lambda}{T} \ , \tag{4.4}$$

where T is a time span covered by the layer. Combining Equation (4.2) and (4.3) the vertical strain rate in the firn column can be written as

$$\dot{\varepsilon}_z = -\frac{1}{\rho}\frac{\partial \rho}{\partial t} - \frac{\partial u}{\partial x} \ . \tag{4.5}$$

4.2 Flow in Ice

In the previous section a two dimensional flow for the firn is described. The 2D assumption workes because it approximates the conditions observed in the center part of the ice sheet where the thickness of the firn layer is thin relative to the ice thickness. However to model the flow deeper in the ice perpendicular and upstream flow must also be accounted for. To do this a change of coordinate systems is needed.

4.2.1 Coordinate System

In the following a flow oriented coordinate system will be applied. The basic idea is to apply a coordinate system which follows a flow line out from the ice divide. Figure 4.1 shows the new coordinate system. The origin of the coordinate system is below the base of the ice divide. With the z-axis pointing upwards, the x-axis follows the flow line and the y-axis is perpendicular to the flow line. A velocity vector is defined as $\mathbf{v}(x, y, z) = (u, v, w)$ and R is the curvature of the surface elevation contour, r is the curvature of the flow line, S is the surface elevation, B is the basal elevation and the ice thickness is $H = S - B$, as seen in Figure 4.1b.

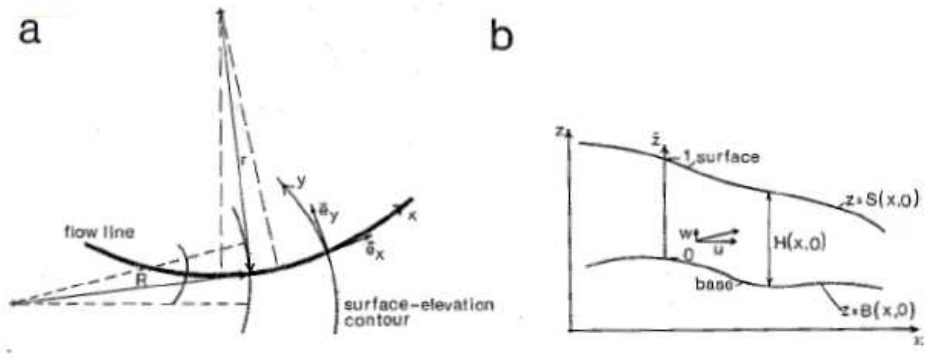

Figure 4.1: Schematic drawing of the defined flow coordinate system. a. is showing the flow line seen from above along with definitions of the curvature parameters. b. The ice is seen along the flow line. Adopted from Reeh [1988].

4.2.2 Derivation of Normal Strain Rates

The Continuity equation, Equation (4.1), can be expressed in normal strain rates as,

$$\dot{\varepsilon}_x + \dot{\varepsilon}_y + \dot{\varepsilon}_z = 0 \ , \tag{4.6}$$

In the flow coordinate system the terms are then given by [Jaeger, 1969; Reeh, 1988; Steen-Larsen, 2007]

$$\dot{\varepsilon}_x = \frac{\partial u}{\partial x} + \frac{v}{r} \tag{4.7}$$

$$\dot{\varepsilon}_y = \frac{\partial v}{\partial y} + \frac{u}{R} \tag{4.8}$$

$$\dot{\varepsilon}_z = \frac{\partial w}{\partial z} \ . \tag{4.9}$$

From the definition of the flow coordinate system $v = 0$ and by assuming the flow lines do not vary with depth the continuity equation is reduced to

$$\frac{\partial u}{\partial x} + \frac{u}{R} + \frac{\partial w}{\partial z} = 0 \ . \tag{4.10}$$

The ice flux can be found by integrating the horizontal velocity from the base of the surface $q = \int_B^S u \mathrm{d}z$. Combining Equation (4.10) and the flux definition gives, according to the boundary conditions, a first order inhomogeneous differential equation in terms of q

$$\frac{\mathrm{d}q}{\mathrm{d}x} + \frac{q}{R} = a_s + a_b - \frac{\partial S}{\partial t} \ , \tag{4.11}$$

where a_s is the surface mass balance in meter of ice per year and a_b is the basal mass balance in meter of ice per year. Both are defined positive for accumulation and negative for ablation. Solving Equation (4.11) gives the flux as a function of space and time

$$q(x,t) = \exp\left(-\int_{x_0}^{x} \frac{1}{R(x')}\mathrm{d}x'\right)\left[\int_{x_0}^{x} \exp\left(\int_{x_0}^{x'} \frac{1}{R(x'')}\mathrm{d}x''\right)\right.$$

$$\times \quad \left(a_s + a_b - \frac{\partial S}{\partial t}\right) \mathrm{d}x' + q(x_0, t)\Bigg] \quad , \tag{4.12}$$

where x_0 is the starting point's distance to the ice divide. Defining a shape function φ of the horizontal velocity and if φ only slowly varies with x then the horizontal velocity may be estimated from the mean horizontal velocity and the shape function.

$$u = u_m(x)\varphi(\tilde{z}) \quad , \tag{4.13}$$

where the mean horizontal velocity is given by

$$u_m(x) = \frac{q(x,t)}{H(x)} \quad , \tag{4.14}$$

and the normalized height by

$$\tilde{z} = \frac{z - B(x)}{H(x)} \quad . \tag{4.15}$$

The shape function $\varphi(\tilde{z})$ has the constrain $\int_0^1 \varphi(\tilde{z})\mathrm{d}\tilde{z} = 1$. An expression for the strain rate is derived from Equation (4.7)-(4.9) and (4.13).

$$\begin{aligned} \dot{\varepsilon}_x &= \frac{\partial u}{\partial x} \\ &= \frac{\partial u_m}{\partial x}\varphi(\tilde{z}) + u_m(x)\frac{\partial \varphi}{\partial \tilde{z}}\frac{\mathrm{d}\tilde{z}}{\mathrm{d}x} \\ &= \frac{\partial u_m}{\partial x}\varphi(\tilde{z}) - \frac{u_m(x)}{H}\frac{\partial \varphi}{\partial \tilde{z}}\left(\frac{\partial B}{\partial x} + \tilde{z}\frac{\partial H}{\partial x}\right) \quad , \end{aligned} \tag{4.16}$$

and

$$\dot{\varepsilon}_y = \frac{u_m(x)}{R(x)}\varphi(\tilde{z}) \quad . \tag{4.17}$$

From Equation (4.6) the vertical strain rate is

$$\begin{aligned} \dot{\varepsilon}_z &= -\dot{\varepsilon}_x - \dot{\varepsilon}_y \\ &= -\frac{\partial u_m}{\partial x}\varphi(\tilde{z}) + \frac{u_m(x)}{H}\frac{\partial \varphi}{\partial \tilde{z}}\left(\frac{\partial B}{\partial x} + \tilde{z}\frac{\partial H}{\partial x}\right) - \frac{u_m(x)}{R(x)}\varphi(\tilde{z}) \quad . \end{aligned} \tag{4.18}$$

4.3 The Dansgaard-Johnsen Flow Model

Equation (4.18) describes the vertical strain rate, but in order to calculate the strain rate a model for horizontal velocity is needed. Using a simple velocity profile down through the ice matrix Dansgaard and Johnsen [1969] developed a model which simplifies the Glen velocity profile by the shape illustrated in Figure 4.2. Hence the model is also known as the kink-model. The Dansgaard-Johnsen Flow Model will be abbreviated the DJ-model in the following. In the following a modified DJ-model is applied with the following assumptions.

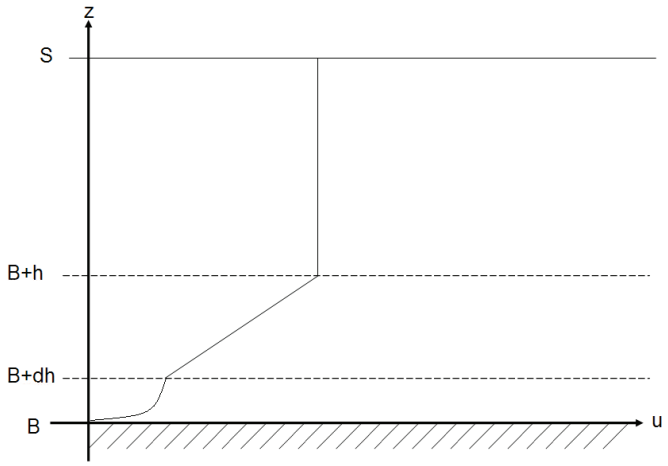

Figure 4.2: The horizontal velocity profile. As simplified in the DJ-model. The sketched velocity form B to $B+dh$ is only one solution of how the velocity in the silty ice might look like. This is dependent one the unknown function $f(\theta, \tilde{z},)$.

- The flow is defined in the flow coordinate system described in Section 4.2.1.
- The horizontal velocity is defined following Figure 4.2 and can be described from the surface velocity u_s

  $B \leq z \leq B + dh$ **:** A mixed layer of silty ice, often found in the bottom of an ice core[1]. The layer covers the last 6 m of the GRIP ice core Dansgaard et al. [1993] and is formed as the ice moves over the bed of the ice sheet. Here the velocity function $u(z)$ is unknown but constrained by the surface velocity

  $$\int_B^{dh} u(z)dz = \theta u_s f_b \ , \tag{4.19}$$

  with the boundary conditions

  $$u(B) = 0 \ \text{ and } \ u(B + dh) = u_s f_b \ . \tag{4.20}$$

  $B + dh < z \leq B + h$ **:** In this middle part the velocity is linearly related to z. Based on the boundary condition of this part the linearity can be found to fulfil

  $$u(z) = \left(1 - \frac{(B + h - z)(1 - f_b)}{h - dh}\right) u_s \ . \tag{4.21}$$

  $B + h < z \leq S$ **:** In the top part the velocity is assumed to be constant and given by

  $$u(z) = u_s \ . \tag{4.22}$$

[1]Because of the basal melt at NGRIP no silty layer is observed [NGRIP Members, 2004]. However, the terminology is kept in the following to refer to the basal ice where the horizontal velocity is allowed to deviate from the kink profile.

- On local scale the parameters a_s, a_b, $\frac{\partial S}{\partial t}$ and R are independent of the horizontal position.
- The flux at the start of the flow line is negligible: $q(0,t) = 0$.

The above assumptions are not far from actual conditions near the ice divide in the central parts of the Greenlandic ice sheet.

4.3.1 Definition of the Shape Function

The shape function can be defined based on the DJ-model by introducing an additional normalization constant k. The shape function is given as

$$\varphi(\tilde{z}) = \begin{cases} f(\theta,\tilde{z})k & \text{for} \quad 0 \leq \tilde{z} \leq \frac{dh}{H(x,y)} \\ \left(1 - \frac{(h-\tilde{z}H)(1-f_b)}{h-dh}\right)k & \text{for} \quad \frac{dh}{H(x,y)} < \tilde{z} \leq \frac{h}{H(x,y)} \\ k & \text{for} \quad \frac{h}{H(x,y)} < \tilde{z} \leq 1 \end{cases} . \tag{4.23}$$

By the definition of the shape function, k is found by normalizing the shape function $\int_0^1 \varphi(\tilde{z})\mathrm{d}\tilde{z} = 1$. The integration reveals

$$k = \frac{1}{\int_0^{\frac{dh}{H}} f(\theta,\tilde{z})\mathrm{d}\tilde{z}} - \frac{(dh-h)(f_b+1)}{2H} + H - h \ . \tag{4.24}$$

The integration of the silty layer is assumed to be $\theta f_b k$, which simplifies k even further

$$k = \frac{2H}{2\theta f_b H + 2H - dh(f_b+1) + h(f_b-1)} \ . \tag{4.25}$$

4.4 Modelling the Ice Flow

Having formalized the flow model through the continuity equation and the set of simple assumptions, the model has to be compared with actual data to model the flow close to the ice divide in central parts of Greenland. Modelling a physical system can be divided into three different phases [Tarantola, 2004]:

1. Parametrization of the system : Finding the minimum number of parameters needed for a full description of the system.
2. Forward modelling : A system of physical laws is setup to model the system in question based on the parametrization. Running the forward model predicts a possible set of data which can be compared to the observable data.
3. Inverse modelling : Observations of the system are used to produce the set of model parameters, which is able to fit data in a desired way.

In the following sections the three phases will be described one by one in preparation for inverse modelling the flow in the proximity of the NGRIP ice core drill site. The core has been drilled on the ice divide running as a ridge at the top of the Greenland ice sheet and ages of internal layers in the core are available from the GICC05 time scale. This data set will be used for the inverse problem solution to estimate the parameters which gives the observed chronology of the core.

4.5 Parametrization of the Flow Equation

In order to compile a reasonable flow model the equations have to be parameterized into the key components used in the model. It is these components that will be estimated later by the solution to the inverse problem. Some of the parameters involved in the model can be estimated directly from other measurements. In the following the individual parameters from the above derived Dansgaard-Johnsen flow model will be discussed in further detail.

Surface and Basal mass Balance

The incoming precipitation is accumulated at the top of the ice sheet at the rate a_s given in meter ice equivalent per year. The location in the dry snow zone implies negligible surface melt. Thereby the accumulation is the only source contributing to the surface mass balance. At the base the amount of ice removed by basal melt is given by a_b and assumed to be constant in time. An extensive study by Dahl-Jensen et al. [2003] found the basal melt rate to vary between 0.72 and 0.80 $\frac{\text{cm}}{\text{year}}$ in a 100 kyr period at the NGRIP drill site. Thereby the assumption of constant melt rate is misleading, but assumed to simplify the parametrization.

Kink and Silty Height

To parameterize the height of the kink, h and the thickness of the silty layer, dh, it is assumed that both are time independent fraction of the total ice height

$$h = \alpha H \tag{4.26}$$

and

$$dh = \beta H \tag{4.27}$$

respectively.

The Sliding Fractionation

The sliding fractionation is assumed to be linear proportional to the basal mass balance

$$f_b = \gamma a_b + \gamma_0 \ , \tag{4.28}$$

from the assumption that water at the base will enhance the basal sliding, which has been observed for glaciers [Hooke, 2005, p. 162]. If melt is present γ_0 is assumed to be zero giving only one parameter to be estimated from the solution to the inverse problem. This fractionation of the basal melt is assumed to be invariant in time.

Silty Layer Shape Constant

To simplify the calculation of the silty layer the shape constant θ is assumed to be invariant in both space and time. To a first approximation the constant is assumed to be affiliated with a linear function, giving

$$\theta = \frac{1}{2} \ . \tag{4.29}$$

Which limits the number of parameters needed in the inversion even further.

Present Topography

The present topography of Greenland is well known and a 5 km resolution Digital Elevation Model (DEM) of Greenland is available from the National Snow and Ice Data Center DAAC, University of Colorado, Boulder, Colorado, [Bamber et al., 2001; Layberry and Bamber, 2001]. Figure 4.3 shows the basal and surface DEM compiled from radar measurements from airplanes. Having the data, a profile through Greenland following the ice divide can be calculated and Figure 4.4 shows such a map. In the figure the gradient of the basal depth, surface and ice height is calculated. The line is chosen in such a way that it intersects the deep drilling projects, almost following the ice divide from the Southern dome to Thule in the North.

Neglecting isostatic movement on the time scale of the model the basal gradient $\frac{\partial B}{\partial x}$ is assumed to be constant in time. The same assumptions are made for the ice $\frac{\partial H}{\partial x}$, the surface gradient $\frac{\partial S}{\partial x}$ and the surface curvature R. All of these can be found from the DEM and are not a part of the solution to the inverse problem. However, the ice height H is allowed to vary in time having an influence on $\frac{\partial S}{\partial t}$.

The Flux q

By the assumptions in Section 4.3 that R, a_s, a_b and $\frac{\partial S}{\partial t}$ all are constant in space on a local scale, and $q(0,t) = 0$, the flux in Equation (4.12) simplifies to

$$q(x,t) \quad = \quad \exp\left(-\int_0^x \frac{1}{R}\mathrm{d}x'\right)\left[\int_0^x \exp\left(\int_0^{x'} \frac{1}{R}\mathrm{d}x''\right)\left(a_s + a_b - \frac{\partial S}{\partial t}\right)\mathrm{d}x'\right]$$

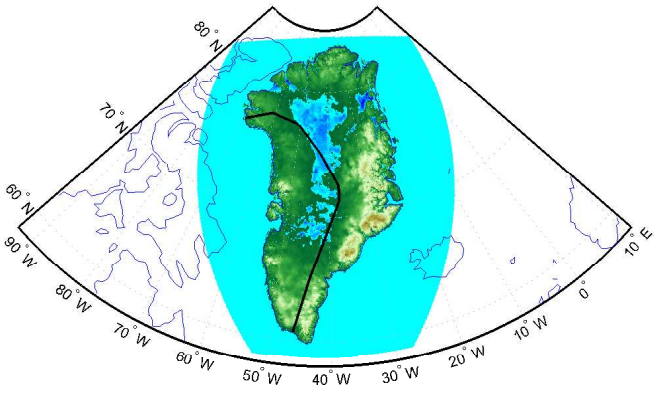

(a) Basal topography

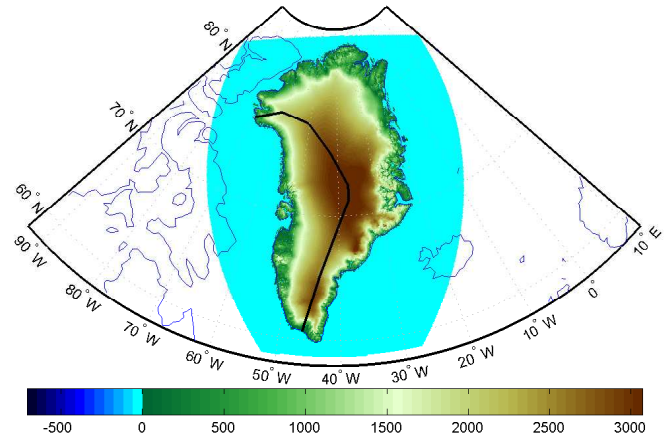

(b) Surface topography

Figure 4.3: The Topography of Greenland: a. The basal topography. Notice how the central parts of Greenland actually is below sealevel accounting for a greater ice thickness than the actual elevation of the ice sheet. b. The surface topography of the ice sheet. The data plotted in this figure will be used as topography needed in the flow model and the black line approximately follows the ice divide form the South dome to Thule using the ice core drill sites as way points. A vertical profile of the line is given in Figure 4.4.

$$
\begin{aligned}
&= \exp\left(-\frac{x}{R}\right)\left(a_s(t) + a_b(t) - \frac{\partial S}{\partial t}\right) R \exp\left(\frac{x}{R}\right) \\
&= R\left(a_s + a_b - \frac{\partial S}{\partial t}\right) \quad . \qquad (4.30)
\end{aligned}
$$

The Vertical Strain Rate

By the spatial independence of Equation (4.30) on a local scale, Equation (4.18) simplifies to

$$
\dot{\varepsilon}_z = \frac{q\varphi(\tilde{z})}{H^2}\frac{\partial H}{\partial x} + \frac{q}{H^2}\frac{\partial \varphi(\tilde{z})}{\partial \tilde{z}}\left(\frac{\partial B}{\partial x} + \tilde{z}\frac{\partial H}{\partial x}\right) - \frac{q\varphi(\tilde{z})}{RH} \quad . \qquad (4.31)
$$

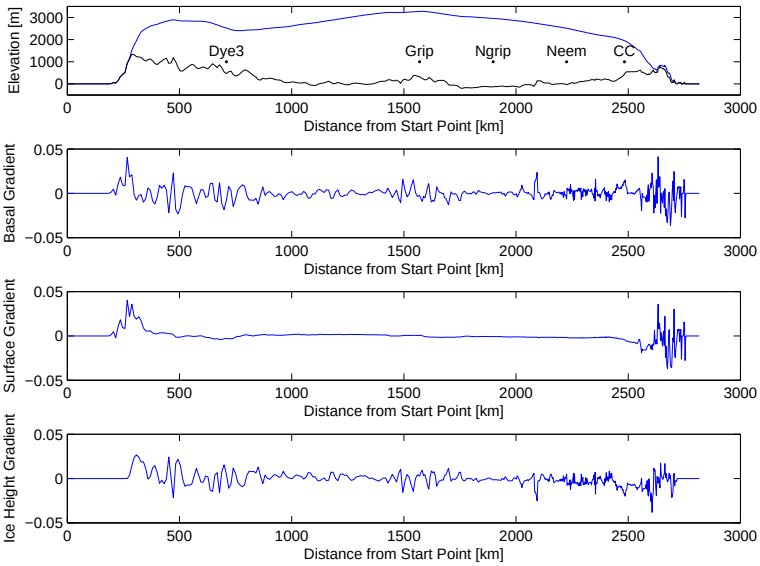

Figure 4.4: The vertical profile of the black line in Figure 4.4 is shown in the upper panel and the three panels below are the basal, surface and ice height gradients calculated from the profiles. The five deep drillings on the Greenlandic ice sheet are also pinpointed in the upper panel.

The Vertical Velocity

Substituting the normalized height $\tilde{z}$ for the real height, gives the normalized vertical strain rate

$$\frac{\mathrm{d}w}{\mathrm{d}z} = \frac{\mathrm{d}w}{\mathrm{d}\tilde{z}}\frac{\mathrm{d}\tilde{z}}{\mathrm{d}z} = \frac{1}{H}\frac{\mathrm{d}w}{\mathrm{d}\tilde{z}} = \dot{\varepsilon}_{\tilde{z}} \ . \tag{4.32}$$

The vertical velocity can be found by integration for a given height $\tilde{z}$,

$$w(\tilde{z}) = H\int_0^{\tilde{z}} \dot{\varepsilon}_{\tilde{z}}(\tilde{z}')\mathrm{d}\tilde{z}' + w_0 \ , \tag{4.33}$$

where w_0 is the basal vertical velocity. Knowing the vertical velocity at a given point in the silty ice is of no interest, since the spoiled stratigraphy in this layer makes the silty layer irrelevant for physical ice core studies. To calculate the velocity above the silty lay integral, $\int_0^{dh/H}\dot{\varepsilon}_z\mathrm{d}\tilde{z}$, has to be solved and is denoted $w_{\frac{dh}{H}}$

$$\begin{aligned} w_{\frac{dh}{H}} &= \left(\frac{q}{H^2}\frac{\partial H}{\partial x} - \frac{q}{RH}\right)\int_0^{\frac{dh}{H}}\varphi(\tilde{z})\mathrm{d}\tilde{z} \\ &+ \frac{q}{H^2}\frac{\partial B}{\partial x}\int_0^{\frac{dh}{H}}\frac{\partial\varphi(\tilde{z})}{\partial\tilde{z}}\mathrm{d}\tilde{z} + \frac{q}{H^2}\frac{\partial H}{\partial x}\int_0^{\frac{dh}{H}}\frac{\partial\varphi(\tilde{z})}{\partial\tilde{z}}\tilde{z}\mathrm{d}\tilde{z} \\ &= \left(\frac{q}{H^2}\frac{\partial H}{\partial x} - \frac{q}{RH}\right)\theta f_b k \\ &+ \frac{q}{H^2}\frac{\partial B}{\partial x}f_b k + \frac{q}{H^2}\frac{\partial H}{\partial x}f_b k\left(\frac{dh}{H} - \theta\right) \ . \end{aligned} \tag{4.34}$$

The velocity above the silty layer is then divided into two.
From $\frac{dh}{H} \leq \tilde{z} \leq \frac{h}{H}$:

$$\begin{aligned} w(\tilde{z}) &= H\left[w_{\frac{dh}{H}} + \left(\frac{q}{H^2}\frac{\partial H}{\partial x} - \frac{q}{RH}\right)\int_{\frac{dh}{H}}^{\tilde{z}} \varphi(\tilde{z})\mathrm{d}\tilde{z}\right. \\ &+ \left.\frac{q}{H^2}\frac{\partial B}{\partial x}\int_{\frac{dh}{H}}^{\tilde{z}} \frac{\partial\varphi(\tilde{z})}{\partial\tilde{z}}\mathrm{d}\tilde{z} + \frac{q}{H^2}\frac{\partial H}{\partial x}\int_{\frac{dh}{H}}^{\tilde{z}} \frac{\partial\varphi(\tilde{z})}{\partial\tilde{z}}\tilde{z}\mathrm{d}\tilde{z}\right] + w_0 \\ &= H\left[w_{\frac{dh}{H}} + \left(\frac{q}{H^2}\frac{\partial H}{\partial x} - \frac{q}{RH}\right)\right. \\ &\times \left(\frac{k((f_b-1)\tilde{z}^2H^2 + 2(dh - f_bh)\tilde{z}H - dh^2(f_b+1) + 2dhf_bh)}{2(dh-h)H}\right) \\ &+ \left.\frac{q}{H^2}\frac{\partial B}{\partial x}\left(\frac{(f_b-1)(\tilde{z}H - dh)k}{dh-h}\right) + \frac{q}{H^2}\frac{\partial H}{\partial x}\left(\frac{(f_b-1)(\tilde{z}^2H^2 - dh^2)}{2(dh-h)H}\right)\right] + w_0 \ . \end{aligned} \tag{4.35}$$

From $\frac{h}{H} < \tilde{z} \leq 1$:

$$\begin{aligned} w(\tilde{z}) &= H\left[w_{\frac{h}{H}} + \left(\frac{q}{H^2}\frac{\partial H}{\partial x} - \frac{q}{RH}\right)\int_{\frac{h}{H}}^{\tilde{z}} \varphi(\tilde{z})\mathrm{d}\tilde{z}\right. \\ &+ \left.\frac{q}{H^2}\frac{\partial B}{\partial x}\int_{\frac{h}{H}}^{\tilde{z}} \frac{\partial\varphi(\tilde{z})}{\partial\tilde{z}}\mathrm{d}\tilde{z} + \frac{q}{H^2}\frac{\partial H}{\partial x}\int_{\frac{h}{H}}^{\tilde{z}} \frac{\partial\varphi(\tilde{z})}{\partial\tilde{z}}\tilde{z}\mathrm{d}\tilde{z}\right] + w_0 \\ &= H\left[w_{\frac{h}{H}} + \left(\frac{q}{H^2}\frac{\partial H}{\partial x} - \frac{q}{RH}\right)\left(\tilde{z} - \frac{h}{H}\right)k\right] + w_0, \end{aligned} \tag{4.36}$$

where $w_{\frac{h}{H}} = \int_0^{\frac{h}{H}} \dot{\varepsilon}_z \mathrm{d}\tilde{z}$ and $w_0 = a_b$ from the boundary conditions. Hence the vertical velocity field from the surface to the top of the silty layer is unambiguous determined.

4.6 Forward Modelling of Particle Paths

After having parameterized the flow model a forward modelling of particle paths down through the ice matrix in a given time span is the next step in the ice flow modelling. In Table 4.1 is a list of all the parameters needed for running the forward model and their spatial and time variabilities. Using the model a particle is set off at the surface in present day conditions and by assuming no change in the accumulation history or the ice height at the site, the particle is numerically integrated 30000 years down into the ice matrix. Figure 4.5 shows a calculated horizontal movement of such an ice particle. In the 30000 years it only moves about 33 km in the horizontal direction.

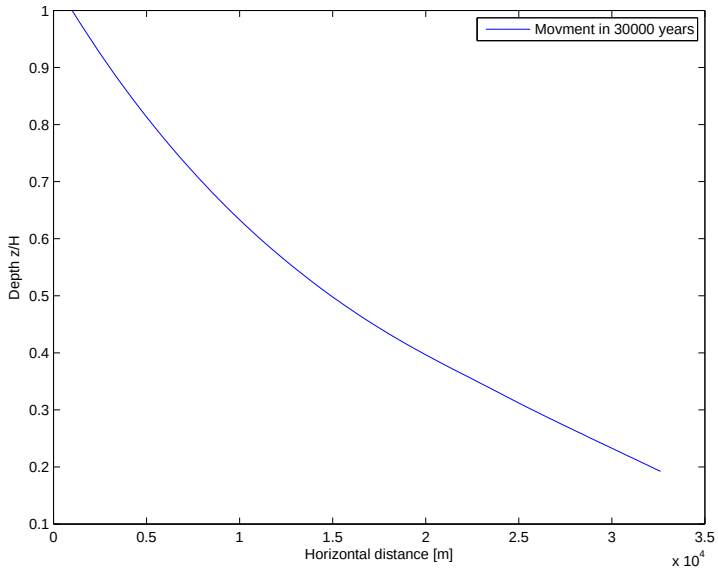

Figure 4.5: From present day accumulation and surface elevation the horizontal movement is calculated for an ice parcel in 30000 years. The vertical displacement is only about 33 km. The present day parameterizations can be assumed to be a maximum of the displacement. Hence the accumulation is lower in the Last Glaciation.

Comparing these findings with the resolution of the DEM, which is 5×5 km, not much information is lost by assuming that the spatial parameters are constant when only modelling on the time span covering the Holocene, transition and down to the LGM. The flat base in proximity of the drill site further supports this assumption, see Figure 4.4. It simplifies the amount of computation needed to run the forward model, by making the model quasi 1-dimensional.

Table 4.1: Summary of the parameters needed for the forward model and its dependency of both space and time. The first six are subjects for the inversion, whereas θ is assumed known, $\frac{\partial S}{\partial t}$ is a function of the evolution of H, and the last three are known from the DEM.

	Variable in Time	Constant in Time	Variable in Space	Constant in Space
a_s	$\surd$	$\div$	$\surd$	$\div$
a_b	$\div$	$\surd$	$\surd$	$\div$
H	$\surd$	$\div$	$\surd$	$\div$
α	$\div$	$\surd$	$\div$	$\surd$
β	$\div$	$\surd$	$\div$	$\surd$
γ	$\div$	$\surd$	$\div$	$\surd$
γ_0	$\div$	$\surd$	$\div$	$\surd$
θ	$\div$	$\surd$	$\div$	$\surd$
$\frac{\partial S}{\partial t}$	$\surd$	$\div$	$\surd$	$\div$
R	$\div$	$\surd$	$\div$	$\surd$
$\frac{\partial B}{\partial x}$	$\div$	$\surd$	$\surd$	$\div$
$\frac{\partial H}{\partial x}$	$\div$	$\surd$	$\surd$	$\div$

A numerical routine for tracking a layer's movement from the surface into the ice in a given time span is made as a forward model. The movement of a layer is governed by the vertical and horizontal velocity field parameterized in Equation (4.34) - (4.36) and (4.13). The numerical integration is done

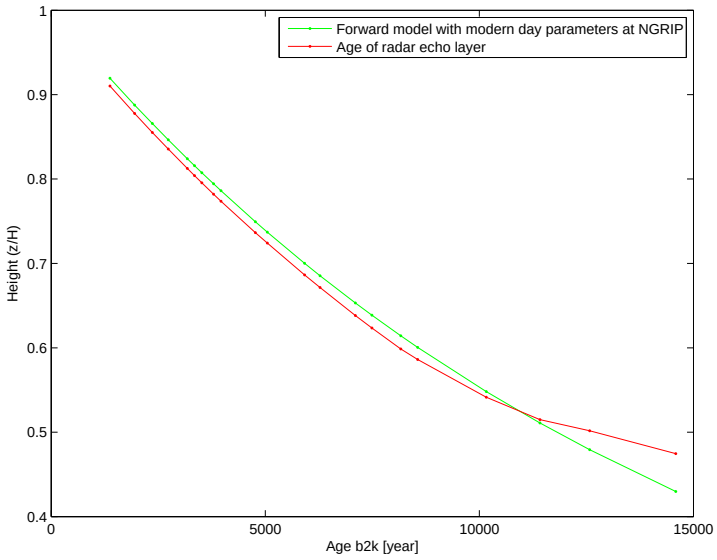

Figure 4.6: Model run with modern day climate compared with the observed age vs. depth at NGRIP. The distance between the two curves are almost constant in the Holocene period but starts to deviate at the 8.2 kyr event, indicating large scale climate shift.

using a Adams-Bashforth-Moulton PECE solver[2] to calculate the present depth of a layer having a certain age.

In order to verify the forward algorithm a number of tests have been performed to see the response to various scenarios. A small selection is presented in Appendix A.1 showing how the forward model behaves in a desired way. After having established a functional forward model, the next step is to run the model and compare it to actual data from the Greenland ice sheet. A complete list of depth vs. age for the different deep drillings in Greenland is compiled by GICC05 and the data is available at GICC05 [2005]. Also a small data set listing Age vs. Depth is available from radar echo layer tracking from airborne measurements along the ice divide from NGRIP to the new drill site at NEEM. The dating of the NGRIP core is used to date this data set. A set of 21 layers are listed in Appendix A.3 and in Figure 4.6 the data for NGRIP is compared with a numerical model run with present day climate parameters. The two curves follow each other down to about 10 kyr b2k, where the similarity stops, matching the time of the transition from the present warm period into the Last Glacial. This comparison emphasizes the need for inverse modelling of the flow parameters. The limited data set from the radar echo layers will be used as observed data for the inverse problem solution to limit computations.

[2]Is implemented in Matlab as the function ode113.

4.7 Formulation of the Inverse Problem

The forward model $\mathbf{g}$ predicts a set of observable quantities $\mathbf{d}_{cal}$ based on the model parameters $\mathbf{m}$ from the general inverse problem formulation,

$$\mathbf{d}_{cal} = \mathbf{g}(\mathbf{m}), \tag{4.37}$$

which can be seen as a mapping of the model space into the data space. Having the forward model this is straightforward if the model parameters are known, but in reality data $\mathbf{d}_{obs}$ is observed and the model parameters have to be estimated. Solving the system to find the best set of model parameters, which predicts the data, is the inverse problem. A Bayesian approach combines the a priori information of a model vector given by the probability density $\rho_M(\mathbf{m})$ with the information obtained by the measurement of the physical system to estimate the probability density of data $\rho_D(\mathbf{d})$ to solve the inverse problem. The solution to the inverse problem is then given by the a posterior probability density $\sigma_M(\mathbf{m})$

$$\sigma_M(\mathbf{m}) = k\rho_M(\mathbf{m})L(\mathbf{m}) \ , \tag{4.38}$$

where k is a normalization constant and L is the likelihood of the model given data

$$L(\mathbf{m}) = \rho_D(\mathbf{g}(\mathbf{m})). \tag{4.39}$$

The likelihood function can be seen as a measure of how well the model fits data. The general solution to the inverse problem provides a probability distribution over the model space. Not knowing the maxima of this probability distribution the model space has to be sampled to estimate the most likely solution to the inverse problem. A pseudo random walk in the model space to sample the model space is referred to as the Monte Carlo Method (MCM). The MCM can successfully be used when analysis is needed of complex a priori information and noisy data. [Mosegaard and Tarantola, 1995; Tarantola, 2004]

4.7.1 A Priori Information

If the only tangible information about a parameter is that the parameter is limited by two boundaries m^{α}_{min} and m^{α}_{max} the a priori probability density can be formulated as

$$\rho_M(\mathbf{m}) = \prod_{\alpha \in \mathbf{I}_M} \rho_\alpha \left(m^\alpha\right) \ , \tag{4.40}$$

where

$$\rho_\alpha(m^\alpha) = \begin{cases} \mu_\alpha(m^\alpha) \ for \ m^\alpha_{\min} \leq m^\alpha \leq m^\alpha_{\max} \\ 0 \ \text{otherwise} \end{cases} \ . \tag{4.41}$$

Here $\mu_\alpha(m^\alpha)$ is the constant homogeneous probability density for parameter m^α [Tarantola, 2004]. The presented a priori probability distribution is also known as a flat a priori probability distribution.

4.7.2 Occam's Inversion

The Occam's inversion is an additional constrain on the model parameter, which can be combined with the Bayesian inversion as an a priori information about the system. The inversion searches for the smoothest solution of the varying parameters, for example, in time. Occam's inversion builds on the idea of applying Occam's razor, which is an academic principle stating that *"Hypotheses should be neither unnecessarily complicated nor unnecessarily numerous"* [Constable et al., 1987]. Hence the Occam's inversion is trying to find smooth models in such a way that one is not misled by complicated structures in the models which are not needed for fitting data.
Following Gouveia and Scales [1997] and Steen-Larsen et al. [2008] the solutions to the inverse problem have to fulfill the criteria

$$\min|\mathbf{Rm}| \tag{4.42}$$

and

$$(\mathbf{d}_{cal} - \mathbf{d}_{obs})^T \mathbf{C}_D^{-1} (\mathbf{d}_{cal} - \mathbf{d}_{obs}) \leq T. \tag{4.43}$$

Here $\mathbf{R}$ is the roughening operator estimating the discrete second derivative of the model parameter profile, $\mathbf{C}_D$ is the data covariance matrix and T is the tolerance for N data points of the model given by

$$T = \sqrt{N}\left(1 - \frac{1}{4N} + \frac{1}{32N^2} + \mathcal{O}(N^3)\right) \quad , \tag{4.44}$$

where $\mathcal{O}(N^3)$ is higher order terms, which is neglected. The left side of Equation (4.43) can be defined as the misfit χ^2 between models and actual data point by

$$\chi^2 = \sum_{j=1}^{N_{obs}} \frac{\left(d_{obs_j} - d_j\right)^2}{\sigma_j^2} \quad , \tag{4.45}$$

where σ_j is the standard deviation of the jth parameter. The roughening operator from Equation (4.42) can be derived as a finite-difference representation,

$$c_j = \frac{\mathrm{d}^2 m}{\mathrm{d}t^2} = \frac{\frac{m_{j+1}-m_j}{t_{j+1}-t_j} - \frac{m_j - m_{j-1}}{t_j - t_{j-1}}}{\frac{1}{2}(t_{j+1} - t_{j-1})} \quad . \tag{4.46}$$

Ignoring the boundaries the probability distribution is defined as

$$\rho_M(\mathbf{m}) = \exp\left(-\eta^2 \sum_{j=2}^{N_m - 1} \frac{(c_j - c_j^{(0)})^2}{2\sigma_c^2}\right) \quad , \tag{4.47}$$

where $c_j^{(0)}$ is the a priori smoothness, which is normally set to zero, and σ_c is the characteristic curvature in the parameter $\mathbf{m}$, given by

$$\sigma_c = \frac{b_c}{T_c^2}, \tag{4.48}$$

where b_c is the characteristic change in a parameter during a characteristic time scale T_c [Waddington et al., 2007; Steen-Larsen et al., 2008]. Adjusting the Lagrange multiplier η to minimize the misfit with the allowed tolerance

$$\chi^2 - T = 0 \ , \tag{4.49}$$

the smoothest a priori information of the system is then used in the form of Equation (4.47).

4.7.3 Probability Density of Data and Likelihood Function

Having an n-dimensional data set $\mathbf{d}$ and a set of observed data $\mathbf{d}_{obs}$, the probability density of the data is given by

$$\rho_D(\mathbf{d}) = \frac{1}{\sqrt{(2\pi)^n \det \mathbf{C}_D}} \exp\left(-\frac{1}{2}(\mathbf{d}-\mathbf{d}_{obs})^T \mathbf{C}_D^{-1}(\mathbf{d}-\mathbf{d}_{obs})\right). \tag{4.50}$$

It is assumed that the errors on the observed data are of Gaussian nature and described by $\mathbf{C}_D$ [Tarantola, 2004]. The prefix ^{T} denotes the transposed matrix.

4.7.4 Metropolis Algorithm for Monte Carlo Simulations

To guide the pseudo random walk in the MCM the Metropolis Algorithm can be applied in the form formulated by Mosegaard and Tarantola [1995]. A new point i in the random walk can be rejected or accepted by the algorithm by comparing the point i with the previous point j according to the following rule:

- If the a posteriori probability density at point i is higher or equal to the one at point j, then i is accepted as a point in the walk with no restrictions.
- If the a posteriori probability density at point i is less than the one at point j, then the random walk accepts the point i with the probability

$$\frac{\sigma_M(\mathbf{m}_i)}{\sigma_M(\mathbf{m}_j)} \ . \tag{4.51}$$

The MCM then follows the steps.

1. Make a start guess of the model parameters $\mathbf{m}_{old}$.
2. Calculate the likelihood of $\mathbf{m}_{old}$.
3. Make a perturbation $\mathbf{m}_{test}$ of $\mathbf{m}_{old}$ by

$$\mathbf{m}_{test} = \mathbf{m}_{old} + S(2r-1) \ , \tag{4.52}$$

where S is the step size used in the random walk and r is a random number homogenous distributed from zero to one. The perturbation is tested in accordance to $\rho_M(\mathbf{m})$.

4. Calculate the likelihood of $\mathbf{m}_{test}$.

5. Accept or reject the test point in accordance to the Metropolis rule.

6. If the point is accepted it is sampled and the process is repeated from step 3 with $\mathbf{m}_{test} = \mathbf{m}_{old}$.
   If the point is rejected $\mathbf{m}_{old}$ is kept and the process is repeated from point 3.

To sample the model space properly the process is run for a great number of iterations. The step size is chosen in such a way that the acceptance rate of the proposed model is between 0.35 and 0.60. This ensures that the sampling is not only confined to a local maximum in the a posteriori probability density, but samples the model space of interest in the most optimal way.

4.7.5 Burn-in and Model Sampling

Due to the large number of iterations needed to sample a multi-dimensional model space, routines of sampling the accepted models are needed to limit the output data. First of all, depending on the initial guess of model parameters, the algorithm needs time to *"burn-in"*, i.e. bring the likelihood of the model down to a reasonable level, see Figure 4.7. The number of iterations before the stable level is defined as the burn-in and indicated with the reddish color in Figure 4.7. Models sampled before the burn-in are unreliable,

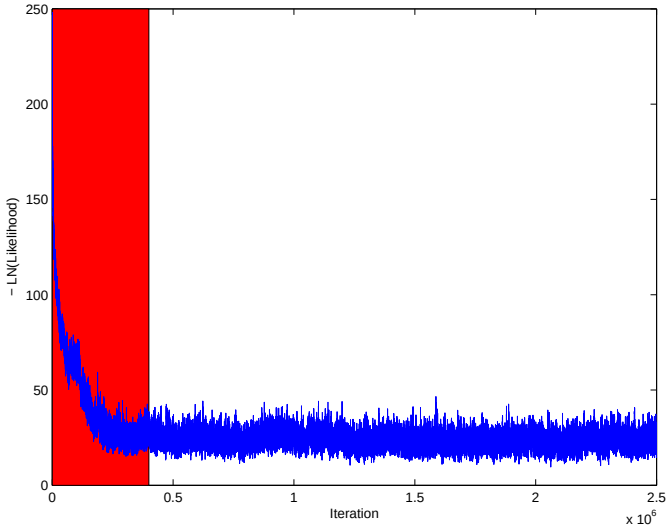

Figure 4.7: The Burn-in of of the MC method can be shown by depicting the number of iterations vs. minus the logarithm to the likelihood. The likelihood is decreasing to a stable level in a number of iterations. This number burn-in time is here about $4 \cdot 10^5$ iterations.

as representative models for the system, and only models after the burn-in are used to estimate the model parameters by calculating the distribution of each parameter.

A further reduction in the number of sampled models is done by only sampling uncorrelated models. The number of models in between uncorrelated models (M_{un}) can be estimated from looking at the one lag autocorrelation (a) of the likelihood function after the the burn-in of the models

$$M_{un} = -\frac{\Delta M}{\log a}, \tag{4.53}$$

where ΔM is the model spacing of sampled models in the likelihood function [Mosegaard and Tarantola, 1995].

4.7.6 Model Parameter Estimation After Sampling

After having sampled a large number of uncorrelated models the most likely set of parameters is chosen by calculating the appearance of a certain parameter value, see Figure 4.8a. The mean and standard deviation are found by simple statistics. Not all of the parameters are likely to exhibit a well behaved gaussian nature with a well defined mean as in Figure 4.8a. Some of the distributions show multiple maxima for a parameter, as seen in Figure 4.8b. Estimating the behavior of the parameter depicted in Figure 4.8b with only one gaussian would not fully explain the maxima found for the parameter. Fitting multiple gaussians to the distribution is then done using Expectation Maximization (EM) clustering [Steen-Larsen et al., 2008]. This method fits multiple gaussians to the histograms in the N-dimensional model space and the most likely mean and standard deviation of a parameter is estimated [Moon, 1996]. To estimate the number of gaussians needed, scatter-cloud plots of parameter pairs are plotted, as seen in Figure 4.9. The figure shows how the presented pair has at least five separate maxima.

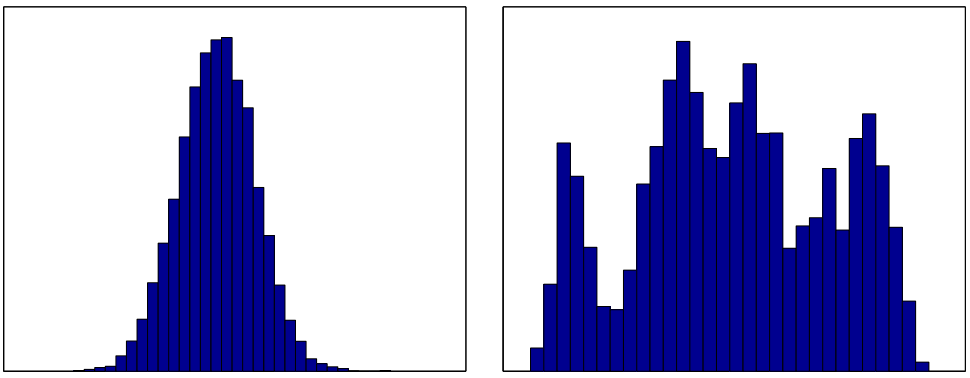

(a) (b)

Figure 4.8: Histogram of parameter solutions. a. A well behaved histogram of a model parameter with gaussian distribution. b. A less well behaved histogram, which look more like a superposition of Gaussians.

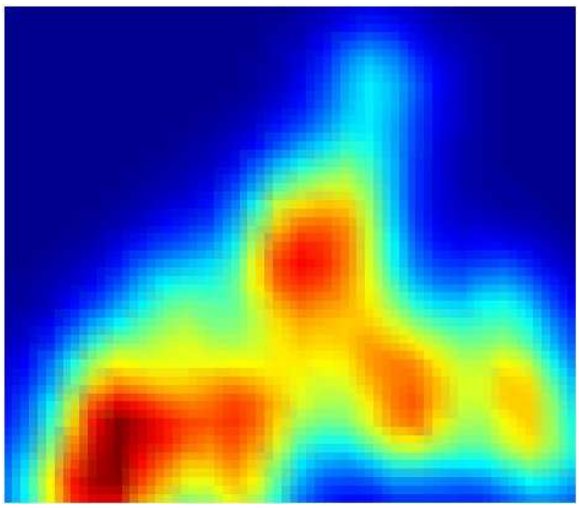

Figure 4.9: Scatter-cloud of two parameters. The more reddish the color the higher is the appearance of this parameter value set. It can be argued that five interconnecting clusters are present for the two parameters plotted.

4.8 NGRIP A Priori Information

To minimize the bias of model parameters a flat a priori probability distribution is used for solving the inverse problem of estimating the NGRIP flow parameters. The limits are based on present day observed values and other model calculations done for the flow in the area [Johnsen, 2008]. The values are then taken as a mean value of the parameter with the limits equally spaced about the mean. Below the parameters are described, along with chosen boundaries for the NGRIP ice core.

H : The surface height, in time steps of 1000 years. A flat a priori between $H_{present} - 500$ and $H_{present} + 500$ m. The surface height is forced with the present value at the time step equivalent to present day.

a_s **:** The surface mass balance. A flat a priori between 0.00 and 0.50 $\frac{\mathrm{m_{ice}}}{\mathrm{year}}$. The surface mass balance is forced with the present value at the time step equivalent to present day.

a_b **:** The basal mass balance, which is constant in time. A flat a priori between -0.20 and 0.00 $\frac{m_{ice}}{year}$.

α **:** The kink height fraction of the ice thickness, which is constant in time. A flat a priori between 0 and 1.

β **:** The silty ice height fraction of the ice thickness, which is constant in time. A flat a priori between 0.00 and 0.01.

γ **:** The fraction of the basal sliding with respect to a_b, which is constant in time. A flat a priori between -150 and 0.

γ_0 **:** The offset of the basal sliding is neglected.

In addition to the flat a priori distribution a smoothing of the time dependent parameter is added in agreement with Occam's inversion scheme. A naive hope was that this addition would not be needed but model runs without Occam's inversion scheme showed an oscillation between the two time dependent parameters (a_s and H) cancelling out the change in each other, see Appendix A.2. Thus, the only way to control the correlation between the two model parameters is to use Occam's inversion constrain as a priori information. Lagrange multipliers for both parameters are unknown and can only be found by running the model past the burn-in with different values for each.

4.8.1 Estimation of Lagrange Multipliers

For a characteristic time of change of 1000 years the characteristic accumulation $b_{c_{a_s}} = 0.05\ \frac{\mathrm{m_{ice}}}{\mathrm{year}}$ and the characteristic change in height $b_{c_H} = 15$ m is chosen. The values are chosen in order to control the fluctuations in the two parameters. The Lagrange multipliers help to moderate the characteristic accumulation and height according to features actually seen in data. In order to determine the Lagrange multipliers for the two parameters random values are chosen and the Monte Carlo model is run past the burn-in time of the model. The average misfit after the burn-in is calculated for each model run. Figures 4.10a and b show the calculated misfit after the burn-in of 39 model runs with randomly chosen values of η_{a_s} and η_H. The Lagrange multipliers which fulfils the condition

$$\chi^2 - T = 0\ , \tag{4.54}$$

have been found by fitting a second order polynomial, as seen in Figure 4.10. The polynomial roots, in the range of the plots0, give the estimated value $(\eta_{a_s}, \eta_H) = (8.04, 6.84)$, which is chosen for further modelling of the NGRIP ice core.

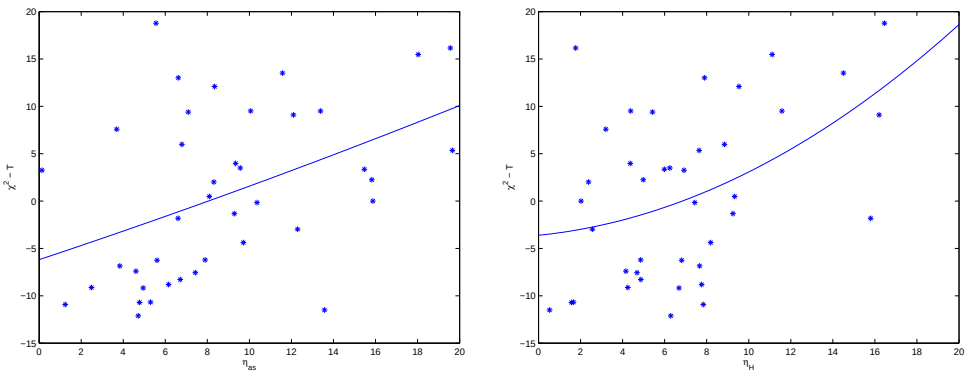

(a) η_{a_s} (b) η_H

Figure 4.10: The estimation of the Lagrange Multipliers is based on comparisons of 39 model runs past the burn-in. To find the zero-crossing is a second order polynomial fitted to the misfit point of the models.

4.9 Results of the Monte Carlo Simulations

The Monte Carlo simulation of the NGRIP flow parameter is done to estimate an age-depth relationship from the list of radar echo layers in Appendix A.3. The unknown parameters which are time dependent (a_s and H) have a equal spacing of 1000 years to limit the computational power needed to solve the problem and cover a time period from 0-18 kyr before present, however for $a_s(t = 0)$ and $H(t = 0)$ the present day value is used. Given a total of 40 parameters to be estimated, the model runs for $2.5 \cdot 10^6$ iterations. To optimize the acceptance rate of the Metropolis Algorithm and assuring a well sampled model space the step size is adjusted if the acceptance rate, becomes too high or too low, gives a final acceptance rate of 47.4 %, which is within the 30-50 % range proposed by Tarantola [2004] to ensure a well sampled model space. The burn-in time is about $4 \cdot 10^5$ iterations. Analyzing the tail of the likelihood function using Equation (4.53) the spacing between uncorrelated models is found to be 88 iterations, which gives 11786 uncorrelated models to base the statistics on.
To investigate the correlation of parameters in the model solutions Figure 4.11 shows the correlation map of the 40 model parameters in the 11786 models. Both a_s and H show significant correlation with themselves between time steps. This behavior must be ascribed to the constrain in Occam's inversion and must be accepted. This behavior is also consistent with the expected behavior of the accumulation change over the ice sheet. The surface height shows a noticeable shift in the correlation map at about 8 kyr. At this time it shifts from a strong correlation to a strong anti-correlation, which can be linked to elevation decrease in the transition into the Last

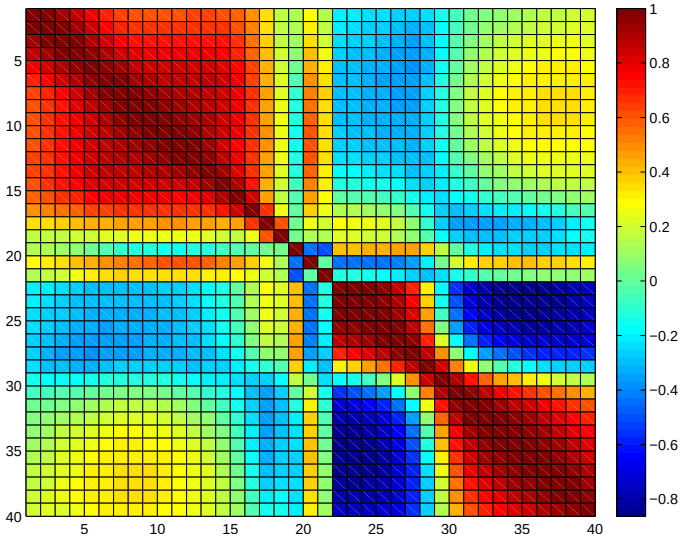

Figure 4.11: Correlation map of the parameter represented by the sampled uncorrelated models. The numbers in the figures refers to the parameter: 1-18 is a_s, 19 is a_b, 20 is α, 21 is γ, 22-39 is H and 40 is β.

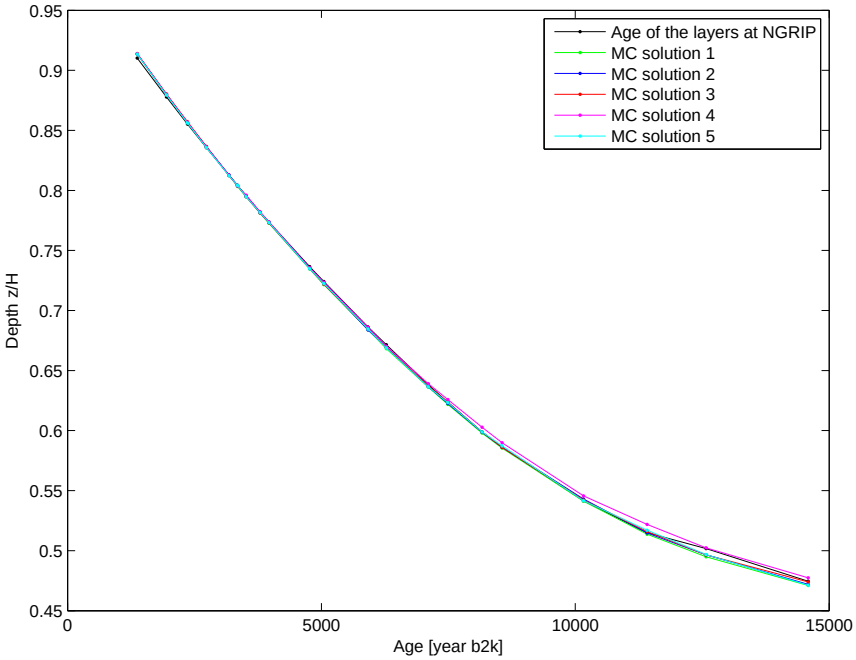

Figure 4.12: The five weighted solution found by the EM routine, compared with the data. Notice the similarities down to about 10 kyr b2k. Solution number five is weighted highest and is chosen as the final solution of the MC simulation, but as seen is the Occam's inversion also limiting the curvature of the found solutions.

Glaciation, seen in almost all of the models. The only other parameter showing an increased correlation is that between α and the surface accumulation at the middle of the time span. This behavior is not understood, but must be influenced by the physical coupling of an increase in accumulation linked to an increase of surface elevation on short time scales.

When examining the scatter-cloud representations of the model parameters, the solutions seem to be located in five different peaks, see Figure 4.9. An EM routine is run to calculate the five solutions to the problem. The the solutions are weighted according to how pronounced they appear in the 40-dimensional model space. The five solutions are compared with the data points in Figure 4.12. Solution five scores the highest. However a common feature of the models is that they fit data rather well until about 10 kyr b2k. This behavior can be partly ascribed to the time resolution of the model which is not able to cope with the rapid climate shifts in the transition, but also be induced by the smoothness from the Occam *a priori*. With the limited data points from the radar echo layers in mind, solution five may be a good candidate to give a general picture of the behavior in the Holocene.
The estimated values of the parameters are shown in Figure 4.13 for a_s and H along with the standard deviation (STD) of the gaussian and the time independent parameters are listed in Table 4.2. The basal melt estimated in this solution is lower than the 6.1 $\frac{\text{mm}}{\text{year}}$ found by Buchardt and Dahl-Jensen [2007], but may be caused by the shallow depth of the data used in the

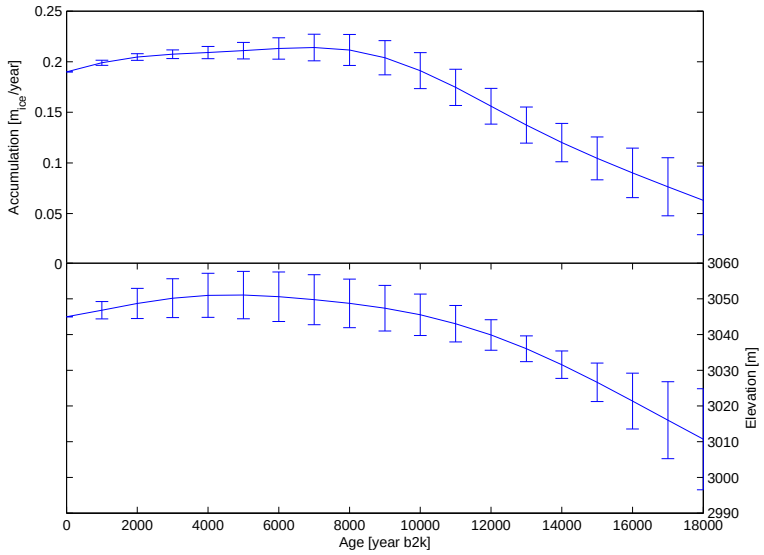

Figure 4.13: Elevation and accumulation history of NGRIP from solution five and the standard deviation of the gaussian indicated in the plot as the error bars.

inversion. The lowering of the elevation of the ice sheet down into the Last Glacial is also seen in the 3-dimensional model of the Greenland ice sheet by Greve [1997], but is less than expected. Also the predicted surface elevation of the early Holocene is less than seen by other models, especially far less than the 200 m found by Vinther et al. [2008a].

Parameter	a_b $\left[\frac{m_{ice}}{year}\right]$	α	β	γ	γ_0
Value	-0.0045	0.52	0.0050	-18.0	0
STD	0.0023	0.15	0.0029	14.0	0

Table 4.2: The flow parameters found for NGRIP by the MC simulation and the standard deviation of the gaussian.

The accumulation and strain rate are needed in the coming chapters to estimate the diffusion processes at the drill site. Hence the found parametrization is in the next section compared with the ss09sea time scale, which has been used to describing the flow parameters at NGRIP.

4.10 Comparison with the ss09sea

As mentioned in the introduction of this chapter other model studies of the ice flow are relying on the δ^{18}O record to estimate the past accumulation record. For the NGRIP drill site the ss09sea time scale is of particular interest [Johnsen et al., 2001]. The ss09sea time scale was developed for the GRIP drill site and adopted as a time scale for NGRIP before the GICC05 layer counting was available. ss09sea incorporates changes in $\delta^{18}O_{ocean}$ and for the NGRIP solution the strain rate is found by the ss06bm model[3] [Johnsen,

[3]Modification of the ss06 model for GRIP with basal melt.

2008]. In following only the abbreviation ss09sea will refer to this combination of strain model and time scale. The models are based on the DJ flow model for the horizontal velocity field. The accumulation record is estimated from δ^{18}O by

$$a(t) = a_0 \exp(R). \tag{4.55}$$

Here a_0 is the present day accumulation rate and R is the isotope dependent,

$$R = k_2 \left(\delta^{18}O(t) - \delta^{18}O_w\right) + \frac{1}{2}k_1 \left(\delta^{18}O(t)^2 - \delta^{18}O_w\right). \tag{4.56}$$

$\delta^{18}O_w$ and $\delta^{18}O_c$ are typical isotopic values for the warm interglacial and cold glacial periods, $k_1 = \frac{c_1 - c_2}{\delta^{18}O_w - \delta^{18}O_c}$, $k_2 = c_1 - \delta^{18}O_w k_1$, where c_1 and c_2 is the slope of the accumulation vs. isotopes under the two time periods[Johnsen et al., 1995; Buchardt and Dahl-Jensen, 2007]. The model has after the GICC05 became available been adjusted to fit the GICC05 layer counting down to 42 kyr b2k in the NGRIP ice core and the model estimate both accumulation and strain history at the drill site. The accumulation history for NGRIP is depicted in Figure 4.14. When comparing the results of the MC solution to the ss09sea, the overestimation of the accumulation in the MC solution may be ascribed to the limited time resolution of the model. With time resolution in mind the estimated accumulations are comparable in the two models and the MC solution can be used as a guide line

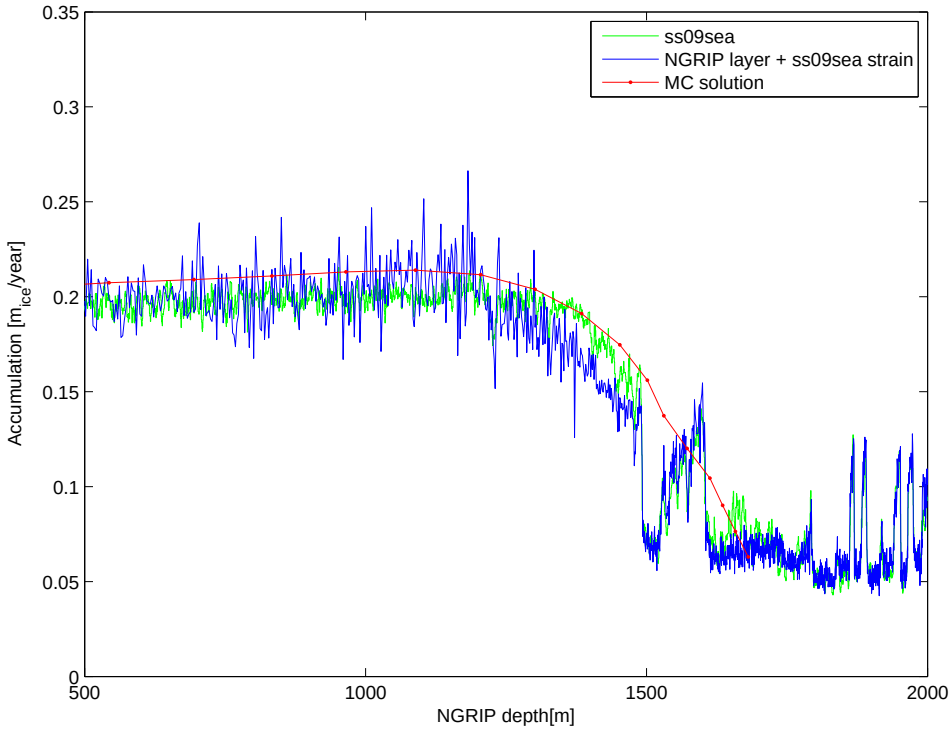

Figure 4.14: Accumulation profile for the NGRIP ice core back to 50 kyr before 1996 modelled both by ss09sea and the MC solution along with the counted layering from the GICC05 strain corrected by the ss09sea. The variability of the accumulation pattern is clearly seen, especially in the glacial for ss09sea, whereas the MC only shows the trend of the Holocene due to the resolution. Data [Johnsen, 2008] and [GICC05, 2005]. Both of the models have difficulties in estimating the accumulation in the early Holocene.

for the accumulation in the Holocene but needs to be calculated in a higher time resolution to account for the rapid oscillations in the transition. For detailed studies where accumulation and other flow parameters are needed the ss09sea is far superior to the MC solution and must be applied to give the most accurate picture of the flow history at the site. However, both of the models are overestimating the accumulation in the early holocene from about the 8.2 kyr event. This overestimation can be caused by a change in the position of the ice divide at this period in time [Johnsen, 2008], which is not parameterized by the models.

The effort gone into the MC flow modelling in this chapter may despite having low time resolution, be justified as a confirmation of coupling the flow model to the isotopic record as a trustworthy approximation. Even though both of the models are having problems with reconstructing the accumulation seen in the early Holocene compared to the GICC05 layer counting.

5

Isotopic Diffusion in Firn and Ice

When recovering the isotopic signal from ice cores the signal is not equivalent to the one which is deposited as snow. As snow is buried the signal is smoothed by diffusion processes. The main diffusion takes place in the firn column, where the interconnected pores allows diffusion by vapor transport. After the pore close-off only little additional diffusion takes place. The aim of this chapter is to describe the diffusion processes affecting the ice core record.

Following the approach described in Johnsen [1977] and Johnsen et al. [2000] the origin of the coordinate system's z-axis follows the layer as it moves down through the firn and ice matrix. Taking the vertical strain rate into account, assuming a uniform strain rate $\dot{\varepsilon}_z$ and a diffusivity for each species i, $D_i(t)$, the diffusion equation becomes

$$\frac{\partial \delta}{\partial t} = D_i(t)\frac{\partial^2 \delta}{\partial z^2} - \dot{\varepsilon}_z(t) z \frac{\partial z}{\partial t} \ , \tag{5.1}$$

where $\delta = \delta(z', t)$ is the smoothed and compressed isotope profile at time t, expressed by the layer thinning function

$$z' = z \exp\left(\int_0^t \dot{\varepsilon}(t'')\mathrm{d}t''\right) \ . \tag{5.2}$$

By defining the diffusion length σ [Johnsen, 1977] as the solution to the differential equation

$$\frac{1}{2}\frac{\mathrm{d}\sigma^2}{\mathrm{d}t} - \dot{\varepsilon}_z(t)\sigma^2 = D_i(t) \ , \tag{5.3}$$

the diffusion Equation (5.1) can be solved by the convolution of $\delta(z, 0)$ with a gaussian clock having the standard deviation σ [Johnsen et al., 2000], which will be used in Chapter 6. Having established the frame of the diffusion process, the diffusion in both firn and ice can be discussed separately. An investigation of the diffusion length will be conducted in the following.

5.1 Diffusion in Firn

In the densification process of firn an exchange of water species is happening through the vapor phase, which smoothes the isotopic ration of δ^{18}O and δD . An important parameter in this process is the diffusivity of each species in the firn D_{fi}. The diffusivity is among others dependent on the toruosity factor τ, which expresses the shape of the interconnected pores in firn and are defined by $D_{eff} = \frac{D_{ai}}{\tau}$, where D_{ai} is the diffusivity of air[1] and D_{eff} is the effective diffusivity inside the pore space [Johnsen et al., 2000]. Furthermore Johnsen et al. [2000] show based on Schwander et al. [1988] and Jean-Baptiste et al. [1998] that the toruosity can be assumed to be a function of the density

$$\frac{1}{\tau} = 1 - b_\tau \left(\frac{\rho}{\rho_{ice}}\right)^2 \text{ for } \rho \leq \rho_{close_{eff.}} \ , \tag{5.4}$$

where $b_\tau = 1.30$ and $\rho_{close_{eff.}}$ is the effective pore close off density

$$\rho_{close_{eff.}} = \frac{\rho_{ice}}{\sqrt{b_\tau}} \ . \tag{5.5}$$

Below $\rho_{close_{eff.}}$ the toruosity factor is $\frac{1}{\tau} = 0$.
Assuming the firn grains are well mixed and in isotopic equilibrium with the vapor, the diffusivity of firn is

$$D_{fi} = \frac{mpD_{ai}}{RT\alpha_i\tau}\left(\frac{1}{\rho} - \frac{1}{\rho_{ice}},\right) \ , \tag{5.6}$$

where m is the molar weight of water, p is saturation pressure over ice, R is the gas constant, T is the temperature and α_i is a fraction constant dependent on the species. The saturation pressure is empirically found to be

$$p = 3.454 \cdot 10^{12} exp\left(\frac{-6133}{T_k}\right) \ , \tag{5.7}$$

[Johnsen et al., 2000].

[1] Values from the literature for the diffusivity of heavy isotopes in air. Calculated in values of the diffusivity of air D_a,

$$D_a = 0.211\left(\frac{T}{273.15}\right)^{1.94}\left(\frac{1}{P}\right)\left[\frac{\text{cm}^2}{\text{s}}\right],$$

where T is the temperature in K and P is the ambient pressure in atm [Johnsen et al., 2000], are;
Merlivat [1978]:

$$D_{a18} = \frac{D_a}{1.0285} \text{ and } D_{aD} = \frac{D_a}{1.0251}$$

Cappa et al. [2003]:

$$D_{a18} = \frac{D_a}{1.0319} \text{ and } D_{aD} = \frac{D_a}{1.0164}$$

The later value will be used in the following

5.1.1 Analytical Solution of the Diffusion Length - Using the HL-Densification Model

Assuming a simple strain rate in firn column

$$\dot{\varepsilon} = -\frac{1}{\rho}\frac{\mathrm{d}\rho}{\mathrm{d}t}, \tag{5.8}$$

which can be derived from Equation (3.9) and (3.10) in the HL densification model. Equation (5.3) is a linear first order differential equation in σ^2, which given the strain rate can be solved analytically [Spiegel and Liu, 1999, Eq. 19.2] and including the diffusivity from Equation (5.6) the diffusion length above the pore close-off is given by

$$\sigma^2 = \left(\frac{\rho_{top}}{\rho}\right)^2 \left(\frac{mpD_{ai}}{RT\alpha_i}\frac{1}{C_{HL}\rho_{ice}\rho_{top}^2}\left(\rho^2 - \rho_{top}^2 - \frac{b_\tau}{2\rho_{ice}^2}\left(\rho^4 - \rho_{top}^4\right)\right)\right) \ , \tag{5.9}$$

where ρ_{top} is the lower integration limit and C_{HL} is constant from the HL-model. The boundary conditions give for $\rho \leq \rho_c$

$$\sigma^2 = \frac{mpD_{ai}}{RT\alpha_i}\frac{1}{k_0 A^a \rho_{ice}\rho^2}\left(\rho^2 - \rho_0^2 - \frac{1.3}{2\rho_{ice}^2}\left(\rho^4 - \rho_0^4\right)\right), \tag{5.10}$$

and for $\rho_c \leq \rho \leq \rho_\tau$

$$\begin{aligned}\sigma^2 &= \frac{mpD_{ai}}{RT\alpha_i}\frac{1}{k_1 A^b \rho_{ice}\rho^2}\left(\rho^2 - \rho_c^2 - \frac{1.3}{2\rho_{ice}^2}\left(\rho^4 - \rho_c^4\right)\right) \\ &+ \frac{mpD_{ai}}{RT\alpha_i}\frac{1}{k_0 A^a \rho_{ice}\rho^2}\left(\rho_c^2 - \rho_0^2 - \frac{1.3}{2\rho_{ice}^2}\left(\rho_c^4 - \rho_0^4\right)\right).\end{aligned} \tag{5.11}$$

This analytical solution is the one previously used by Johnsen et al. [2000] to model diffusion lengths.

5.1.2 Numerical Solution of the Diffusion Length - Using the HL-Densification Model with Full Strain Rate

The assumption of the simple strain rate in Equation (5.8) can be used for the firn as an approximation, because of the limited horizontal displacement due to the shallowness of the firn column. However, accounting for the horizontal velocity the full strain rate is given by Equation (4.5), which gives the additional term $-\frac{\mathrm{d}u}{\mathrm{d}x}$ to the assumed strain in Equation (5.8). Assuming a parametrization as in Section 4.2 this term reduces to

$$\frac{\mathrm{d}u}{\mathrm{d}x} = \frac{q(t)}{H}k \tag{5.12}$$

$$= \frac{2R\left(a_s + a_b - \frac{\partial S}{\partial t}\right)}{2\theta f_b H + 2H - dh(f_b+1) + h(f_b-1)} \ . \tag{5.13}$$

Now Equation (5.3) can be solved numerically using the full strain rate. For simplicity the 30 m elevation change found by the MC flow model is neglected. The only parameter allowed to change in time is the surface accumulation. Figure 5.1a shows a comparison of the analytical and the numerical solution. The addition of the full strain gives a lower diffusion length than found by Johnsen et al. [2000], especially below ρ_c.

5.1.3 Temperature Dependency of the Diffusion length

The temperature profile in the firn is not constant. It changes according to the seasonal variations of the surface temperature. Surface heat is transferred into the firn governed by the general heat transfer equation

$$\rho c \frac{\partial T}{\partial t} = K \nabla^2 T - \rho c \left(u \frac{\partial T}{\partial x} + v \frac{\partial T}{\partial y} \right) + \left(\frac{\mathrm{d}K}{\mathrm{d}z} - \rho c w \right) \frac{\partial T}{\partial z} + f \ . \quad (5.14)$$

Here c is the specific heat capacity, K is the thermal conductivity and f is the internal heat production [Paterson, 2002, p. 224]. Assuming no heat transport in the horizontal plane and that the internal heat production is small, the general heat equation simplifies to

$$\rho c \frac{\partial T}{\partial t} = K \frac{\partial^2 T}{\partial z^2} + \frac{\mathrm{d}K}{\mathrm{d}z} \frac{\partial T}{\partial z} - \rho c w \frac{\partial T}{\partial z} \ . \quad (5.15)$$

The simplified heat equation can be solved numerically given the thermal conductivity of firn from Schwander et al. [1997]

$$K = K_{ice} \left(\frac{\rho}{\rho_{ice}} \right)^{\left[1 - 0.5 \left(\frac{\rho}{\rho_{ice}} \right) \right]} \ , \quad (5.16)$$

and assuming that the seasonality in the surface temperature is given by a sine wave oscillating around the annual mean. Figure 5.1b shows firn temperature profile for each month of the year for the top part of the firn column. The fluctuations in the surface temperature are seen to penetrate the firn to a depth of 10 to 15 meters and then reach the annual mean all year around.

Having established the temperature profile throughout the firn this can be used to estimate the diffusivity of the stable isotopes in a temperature dependant case. The age of a layer is given by

$$age = \frac{1}{A} \int_0^z \rho \mathrm{d}z \ , \quad (5.17)$$

where A is the accumulation in water equivalents assumed to be unchanged in time and z is the depth of the layer. Hence the layers used for numerical

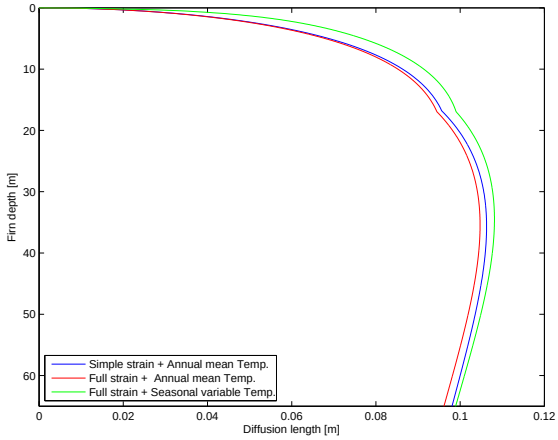

(a)

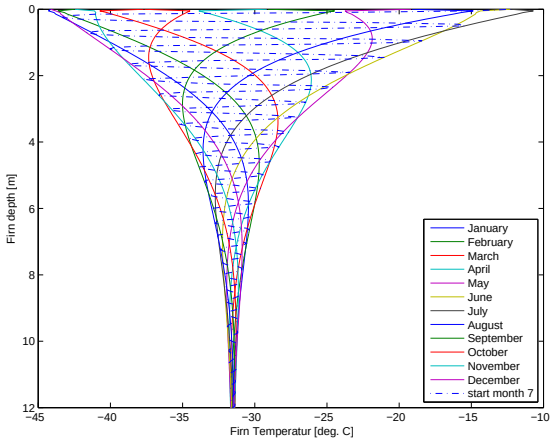

(b)

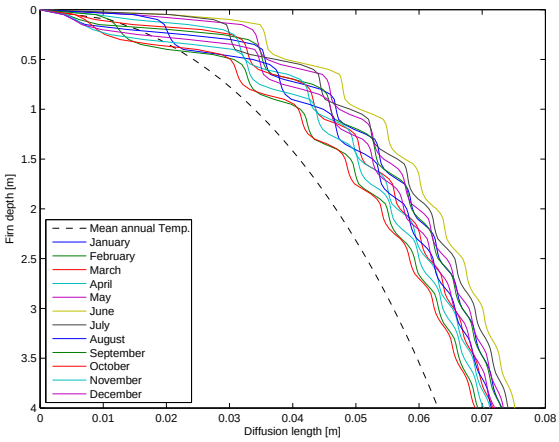

(c)

Figure 5.1: a. Calculated diffusion lengths for δ^{18}O in firn above pore close off. For the three solutions; 1. the analytical simple strain solution. 2. Full strain solution with an annual mean temperature. 3. Full strain solution with a monthly mean temperature. b. Each of the solid lines represents the temperature in one month of the year. The dashed line shows the temperature a layer starting in the summer sees on the way through the firn. c. a close up of the surface firn.

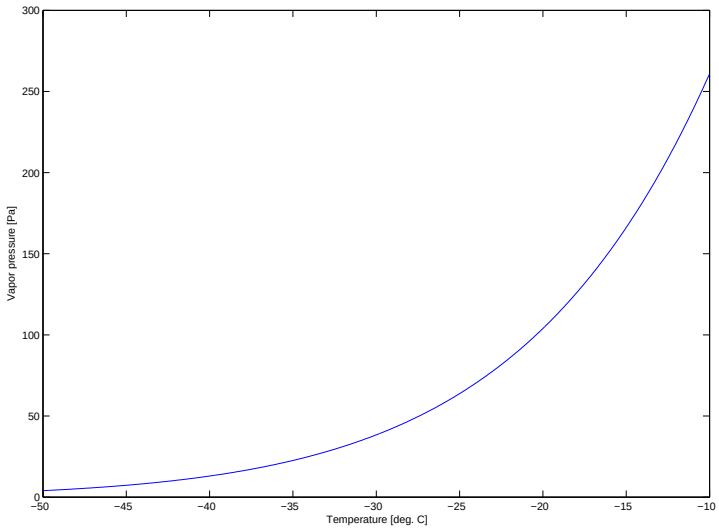

Figure 5.2: Equation (5.7) is depicted in the range experienced by the firn. In this range the vapor pressure is highly non-linear.

evaluation of Equation (5.3) can be assigned a temperature according to the season of the year and the diffusion length can be derived. The dotted line in Figure 5.1b depicts the temperature a layer moving down into the firn experiences. The diffusion length for ^{18}O is depicted in Figure 5.1a, which shows that when only using the mean temperature the diffusion length of δ^{18}O is underestimated.
The difference between the calculated diffusion lengths in Figure 5.1a must be ascribed to the vapor pressure not being linearly related to temperature but given by the exponential function in Equation (5.7) and having nonlinear behavior in the temperature range experienced at the ice core sites, see Figure 5.2.

5.2 Diffusion in Ice

Below $\rho_{close_{eff}}$ the diffusion of the isotopic signal is expected to be caused by single crystal self diffusion with a diffusivity of ice $D_{ice} = 3.96 \cdot 10^4 \exp \frac{-7273}{T}$ $\left[\frac{\mathrm{m}^2}{\mathrm{year}}\right]$ for both of the δ^{18}O and δD of ice [Ramseier, 1967]. This diffusivity is significantly less than the firn diffusivity from Equation (5.6) at equivalent temperatures [Johnsen et al., 2000]. By analyzing MEM[2] power spectra of sections of Holocene ice in the GRIP ice core Johnsen et al. [2000] found a diffusivity of the ice which were higher than the expected from single crystal self diffusion. This indicates that additional diffusion processes are involved in the diffusion of Holocene ice. However, analyzing sections from the Last Glacial an agreement is found between the measured diffusion and

[2]Maximum Entropy Method. The method will be presented in Chapter 6 as Burg's Algorithm of power spectral density estimation.

the single crystal self diffusion for the GRIP ice core. Several explanations for the additional diffusivity of the Holocene ice has been suggested, but the excess diffusivity of Holocene ice has only been observed in the GRIP ice core [Johnsen, 2008] and will not be discussed further.

5.3 Differential Diffusion Length

The differential diffusion length ($\Delta\sigma$) is defined from the diffusion lengths of the the two water isotope as

$$\Delta\sigma^2 \equiv \sigma^2_{^{18}O} - \sigma^2_D \quad . \tag{5.18}$$

Using the above derived equations the differential diffusion length at the base of the firn (at pore close-off) can be calculated as a function of the accumulation and surface temperature. Some results of these calculations can be seen in Figure 5.3. Later these results will be used to determine the temperature history of an ice core section forming the basis of the new ice core Paleothermometer.

In order to estimate the past temperature from Figure 5.3 the measured diffusion length in an ice section (σ_{sec}) has to be corrected for the thinning which has happened after pore close-off. Using the Bernoulli equation

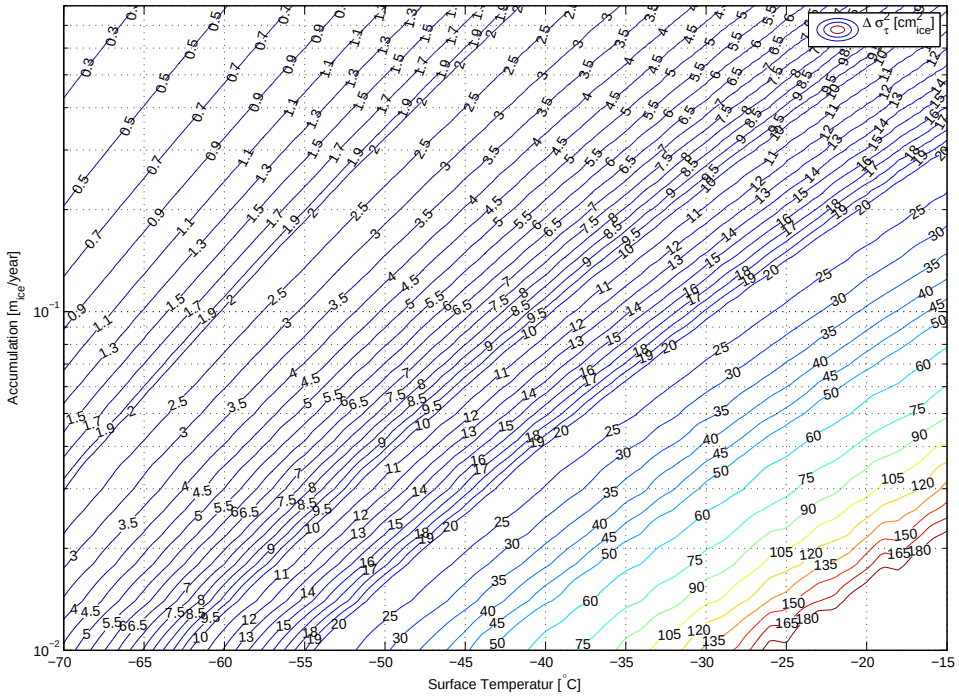

Figure 5.3: Modelled differential diffusion length at the pore close-off depending on accumulation and surface temperature. This result will later be used to estimate the paleotemperatures seen by a limited number of ice core section, by estimating the diffusion length in the section and knowing the accumulation from the GICC05 layer counting.

[Kreyszig, 1999], Equation (5.3) can be solved

$$\sigma^2(t_{sec}) = \exp\left(2\int_{t_\tau}^{t_{sec}} \dot{\varepsilon}(t)\mathrm{d}t\right)\left[2\int_{t_\tau}^{t_{sec}} D_i(t)\exp\left(-2\int_{t_\tau}^{t} \dot{\varepsilon}(\theta)\mathrm{d}\theta\right)\mathrm{d}t + \sigma_\tau^2\right] \quad , \tag{5.19}$$

which gives the expression for the diffusion length at the pore close off

$$\sigma_\tau^2 = \frac{\sigma_{sec}^2}{\exp\left(2\int_{t_\tau}^{t_{sec}} \dot{\varepsilon}(t)\mathrm{d}t\right)} - 2\int_{t_\tau}^{t_{sec}} D_i(t)\exp\left(-2\int_{t_\tau}^{t} \dot{\varepsilon}(\theta)\mathrm{d}\theta\right)\mathrm{d}t \quad . \tag{5.20}$$

The last term in the equation above can be defined as the ice self diffusion σ_{ice}^2. Assuming only self diffusion in ice below the pore close-off the differential diffusion length correction simplifies to

$$\Delta\sigma_\tau^2 = \frac{\Delta\sigma_{sec}^2}{\exp\left(2\int_{t_\tau}^{t_{sam}} \dot{\varepsilon}(t)\mathrm{d}t\right)} \quad . \tag{5.21}$$

Here $\Delta\sigma_\tau^2$ is the diffusion length at the effective pore close-off.

5.4 Modelled Diffusion Length

The diffusion length at a given depth can be modelled from the equations above. A surface temperature reconstruction, which combines δ^{18}O and the measured borehole thermometry from NGRIP [Johnsen, 2008], has been

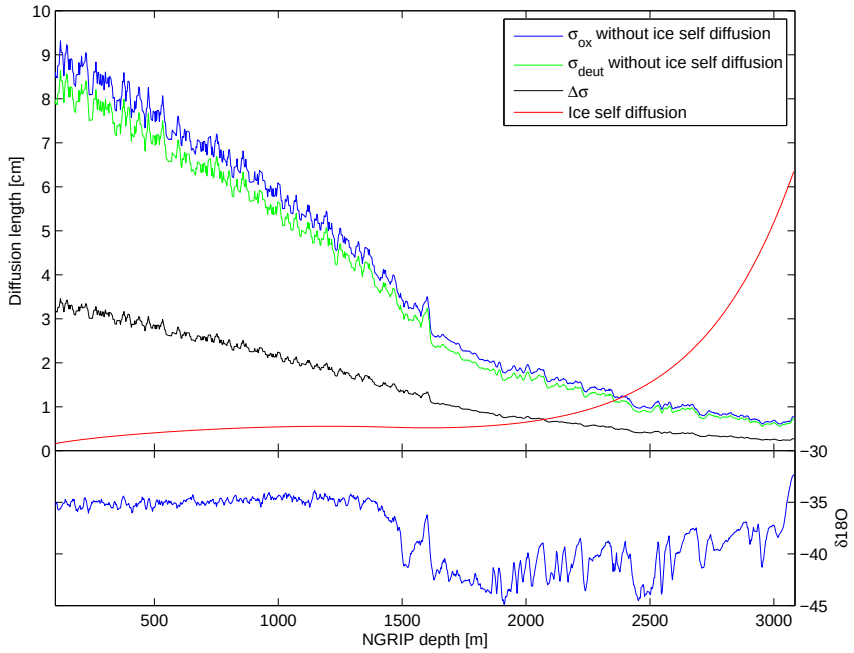

Figure 5.4: Modelled diffusion lengths along the NGRIP ice core. The δ^{18}O record is plotted for reference. Notice how the differential diffusion is not seeing the interstadials in the Last Glacial.

used to derive the firn and ice diffusivity. The calculated diffusions lengths are shown in Figure 5.4.
Figure 5.4 shows that the contribution of the ice self diffusion to the overall diffusion length of the two isotopes is negligible down to about 2100 m. Due to the equal ice self diffusivity of the two isotopes the differential diffusion length is unaffected by the ice self diffusivity. However, the modelled differential diffusion length seems not to record the rapid climatic shifts of the GI events in the Last Glacial.

6

Spectral Analysis of Isotopic Data

This chapter will focus on how to retrieve the isotopic diffusion signal from Greenlandic ice cores. Prior knowledge about the ice core drilling is needed to understand the data used in this chapter.
When an ice core is drilled the core is cut into 55 cm pieces and preserved in a plastic bag. The water isotopes are then measured at different resolutions depending on the purpose of the measurement. A 18 m section of the NGRIP ice core with a sample size[1] of 5 cm is shown in Figure 2.2 for both δ^{18}O and δD .
With measurements of both δ^{18}O and δD, the differential diffusion length along with the diffusion length of the two water isotopes can be estimated from spectral analysis. δ^{18}O have been measured almost for the full length of the deep ice cores in Greenland whereas δD only has been measured across shorter intervals.

6.1 Depositional Spectra of Snow

The spectra of the isotopic signal of precipitation accumulating on the surface is assumed to have a peak corresponding to the yearly periodicity of the signal. In addition to this peak the rest of the spectra is white noised[2]. The surface snow is then mixed by snow drift which adds blue noise to the signal by removing low frequency oscillations [Fisher et al., 1985]. The diffusion then reduces the amplitude of the signal and transform the spectrum to a

[1] The sample resolution is often given as samples per bag, for example, 11pbag is equivalent to a sample size of 5 cm.

[2] The colors of noise are defined as:

White	:	A flat spectra.
Blue	:	An increasing power density with frequency.
Red	:	Decreasing power with increase in frequency, the spectra have a cut-off.

red noised signal [Johnsen, 1977; Fisher et al., 1985], as will be seen in the next section. Studies of synthetic ice core data [Cuffey and Steig, 1998] have shown that after the mixing in the firn column, the annual signal can be retrieved within 20% of the original signal. The authors also pointed out that an optimal ice core drilling site would be a site with high accumulation and low temperatures which, as seen in Figure 5.3, also gives a low differential diffusion length.

6.2 Power Spectral Properties of Diffusion

The Fourier transform of a function $f(t)$ is defined as

$$\mathfrak{F}(\omega) = \frac{1}{\sqrt{2\pi}} \int_{-\infty}^{\infty} f(t) \exp\left(-i2\pi\omega t\right) \mathrm{d}t \ , \tag{6.1}$$

or in the discrete case $f_0, f_1, ..., f_{N-1}$ as

$$\mathfrak{F}(\omega) = \Delta \sum_{n=0}^{N-1} f_n \exp\left(-i2\pi \frac{\omega n}{N}\right) \ , \tag{6.2}$$

[Marple, 1987, p. 42]. It is a transformation of the function f from the time into the frequency domain. ω is the frequency, Δ is the sampling interval and N is number of samples in the section. The total energy of the function $f(t)$ can be found by integrating the squared modulus of the function over the real axis. The energy can be transformed into the frequency domain using *Parseval's Theorem* [Bracewell, 2000, p. 119]. Hence the energy of the system is

$$E = \int_{-\infty}^{\infty} |f(t)|^2 \mathrm{d}t = \int_{-\infty}^{\infty} |\mathfrak{F}(\omega)|^2 \, \mathrm{d}\omega \ . \tag{6.3}$$

The energy spectral density (ESD) is defined as

$$ESD(\omega) = |\mathfrak{F}(\omega)|^2 \ . \tag{6.4}$$

Power is defined as the energy per time unit, thus the power spectral density (PSD) is given by

$$P(\omega) = \frac{|\mathfrak{F}(\omega)|^2}{N\Delta} \ , \tag{6.5}$$

where $N\Delta$ is the periodicity of the function [Marple, 1987, p. 117].

6.2.1 The Fourier Transformed Isotopic Diffusion

As mentioned in Chapter 5 the diffusion is a smoothing of the isotopic signal. One of the simplest ways to smooth a signal is to convolute it with a normalized Gaussian, which is a solution to the diffusion Equation (5.1)

[Johnsen, 1977] giving the measured isotopic signal t after the snow has been deposited

$$\delta(z', t) = \delta(z', 0) * \frac{1}{\sigma\sqrt{2\pi}} \exp\left(-\frac{z^2}{2\sigma^2}\right) \quad , \tag{6.6}$$

where $\delta(z', 0)$ is the original isotopic signal, z and z' follows the definition in Chapter 5. The deconvolution of the signal can be done by transforming the signal into the frequency domain. Using the convolution theorem [Bracewell, 2000, p. 332] the Fourier transformation of the diffused signal can be derived to be

$$\begin{aligned} \mathfrak{F}(k) &= \mathfrak{F}(\delta(z', t)) \\ &= \sqrt{2\pi}\mathfrak{F}\left(\delta(z', 0)\right)\mathfrak{F}\left(\frac{1}{\sigma\sqrt{2\pi}} \exp\left(-\frac{z^2}{2\sigma^2}\right)\right) \\ &= \mathfrak{F}\left(\delta(z', 0)\right) \exp\left(-\frac{1}{2}k^2\sigma^2\right) \quad , \end{aligned} \tag{6.7}$$

where k is the wave number $k = 2\pi\omega$.

6.2.2 Sampling Effects

The ideal way of measuring the isotopic composition in an ice core would be in a continuous way, but as in all physical measurements this is not possible, because the measured signal is discrete. The sampling gives rise to some difficulties when working with the signal in order to retrieve spectral information from the system.
If the sampling is done in an equal spaced interval Δ the Nyquist frequency is defined as [Press et al., 2007, p. 605]

$$f_{nq} = \frac{1}{2\Delta} \quad . \tag{6.8}$$

This is the base of the sampling theorem. The theorem states: If a signal has a bandwidth limited below f_{nq} a continuous function $h(x)$ can be sampled with intervals Δ and fully resolved by as

$$h(x) = \sum_{n=-\infty}^{\infty} h_n \text{sinc}(2f_{nq}(x - n\Delta)) \quad , \tag{6.9}$$

where

$$h_n = h(n\Delta) \text{ and } n \in \mathbb{Z} \tag{6.10}$$

[Press et al., 2007, p. 605]. The sampling theorem is useful, but not all physical systems are bandwidth limited. In this case the PSD of the signal outside $\pm f_{nq}$ gets folded into the range inside the $\pm f_{nq}$ limit. This is often referred to as aliasing and is illustrated in Figure 6.1. To recover the *true* signal of the PSD the effects of aliasing have to be removed. The first step

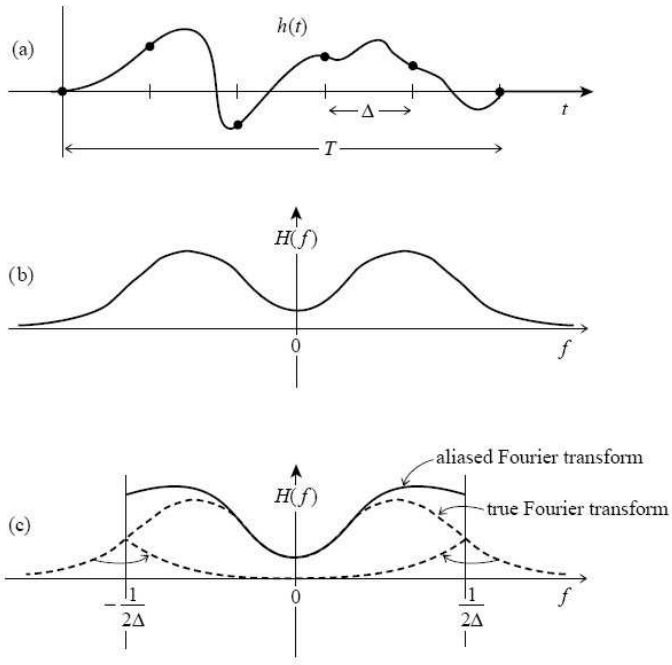

Figure 6.1: Sampling a signal give an aliasing effect on the Fourier transformed signal. a) The continuous signal sampled for every Δ. b) The true Fourier transform $H(f)$ (c) The aliasing effect folds the signal outside f_{nq} into the spectra. The Figure is adopted from Press et al. [2007, p. 606].

is to cut-off all frequencies beyond the f_{nq} limit in the PSD. The second step is to try to estimate the folding effects. The sampling can be seen as a running mean filtering of the data. The running mean has the function

$$r(x) = \frac{\text{rect}\left(\frac{x}{\Delta}\right)}{\Delta} \ , \tag{6.11}$$

here rect is the boxcar function. The Fourier transform of r is given by

$$R(k) = \frac{2\sin\left(\frac{k\Delta}{2}\right)}{k\Delta} \ , \tag{6.12}$$

where k is the wave number [Spiegel and Liu, 1999, eq. 34.37]. Compared with the derived PSD of the isotopic signal an estimate of the aliasing effect from cutting can be calculated by evaluating the expression

$$|R(k)|^2 = \exp(-k^2\sigma^2) \ , \tag{6.13}$$

at f_{nq} giving

$$\sigma^2_{cut} = \frac{2\ln\left(\frac{\pi}{2}\right)}{\pi^2}\Delta^2 \ . \tag{6.14}$$

σ^2_{cut} should be subtracted from the estimated isotopic diffusion length of a ice core section. As long as the sampling is the same for both δ^{18}O and δD the differential diffusion is unaffected by the sampling correction.

6.2.3 Measuring Noise and Cut-Off

Mass spectrometer measurements of water isotopes in ice cores have a certain measuring noise associated with them. Typically the error is around $0.04 - 0.07$ ‰ for δ^{18}O and $0.5 - 1$ ‰ for δD [Johnsen, 2008]. The measuring noise is seen as a flat white noise tail in the PSD of the isotopic signal. Due to the nice behavior of white noise this measuring noise can easily be removed from the PSD by subtracting the noise level from the raw PSD. When determining the diffusion length of the spectrum only the part of the spectrum until the noise tail can be used. The cut-off frequency is then defined as the maximum frequency of the PSD which can be used to determine the diffusion length. Depending on the estimated PSD the cut-off may be chosen to be less than the beginning of the white noise tail.

6.2.4 Climate Variability Correction

To estimate the PSD the isotopic data have to consist of a certain number of samples, which is cover the accumulation history of several hundred years depending on the depth. However the climate is not always stable over this time-span and the isotope record has inter-annual oscillations, see Figure 6.2. The PSD tends to overestimate the low-frequency part of the spectrum resulting in a wrong estimate of the diffusion length. This low frequency

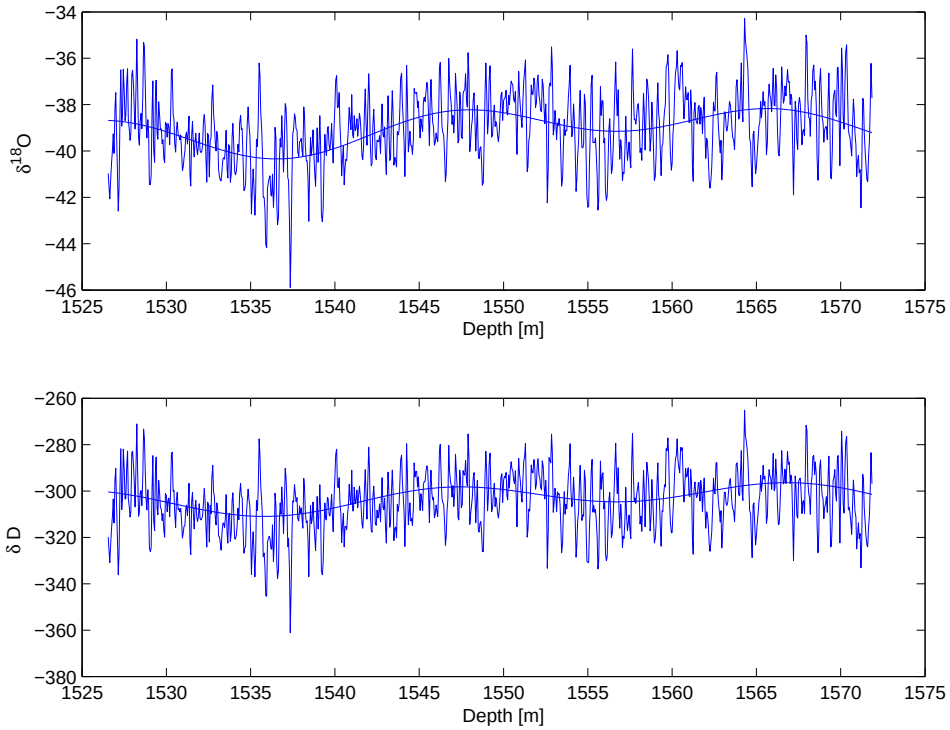

Figure 6.2: The raw isotopic record from NG-trans4a section is shown as a function of depth. As seen by the fitted superposition of sin curves is the record subject to a long scale climate variability.

part of the spectrum, caused by climate trends in the record, must therefore be removed. The trend is estimated by fitting a superposition of sin-waves onto the raw record. Calculating the PSD of this trend gives an estimate of the trend seen in the raw PSD. The raw and trend PSD are compared and all points where more than 10 % of the power in the raw PSD is caused by the climatic trend are removed to form a climate trend corrected PSD.

6.3 Data Processing

As mentioned in the beginning of this chapter the need for both the δ^{18}O and δD records limits the number of sections available for this study. In the GRIP and NGRIP ice cores only about 22 sections are measured with the resolution needed to determined the diffusion length. Table 6.1 summarizes the data files used along with a short description of the physical properties for each sections. In the following discussions the abbreviation noted in the table is used as reference to the section in question.

A number of ways to calculate the Fourier Transform from data has been developed. Three of the methods are used to determine which one is the must reliable when working with the short data series available for differential diffusion analysis.

6.3.1 Fast Fourier Transform

A widely used algorithm for the numerical Fourier transform of a function is the Fast Fourier Transform (FFT). The FFT algorithm divides data into sub data sets, subsequently calculates the transform of the sub data sets and finally recombines the sub data sets into the full data set. The splitting is often done by separating the even and uneven data points. By splitting the raw data set into two, the computation time is approximately halved, even smaller subset reduce the time even further [Lathi, 1998; Bracewell, 2000]. A FFT algorithm is implemented in Matlab and is the one used to calculate the Fourier transform.

The PSD is calculated from the Fourier Transform using Equation (6.5). Assuming that the measuring noise is white, the average power of the white measuring noise tail can be subtracted to remove the measuring noise. In addition to the measuring noise correction the PSD is corrected for the climate trend as described in Section 6.2.4.

The found PSD is then fitted to the expression

$$P_i(k) = P_{0_i} \exp\left(-k^2\sigma_i^2\right) + P_{\epsilon_i} \ , \tag{6.15}$$

Table 6.1: List of sections from the GRIP and NGRIP ice core, where both δ^{18}O and δD are measured. Some of the sections have been split into smaller sections after having reviewed the deuterium excess profile. In the following individual sections will be referred to as its abbreviation.

File	Section abbreviation	Core	Depth [m]	Length [m]	Time span	Avg. Depth [m]	Avg. Age [years b2k]	Δ [cm]	N	σ^2_{cut} [cm^2]
sum893-22pbag-new.dat	sum893-22pbag	GRIP	5.03-39.90	34.08	97	22.46	63	2.50	1363	0.57
sum91-50pbag-oxDxs.col	sum91-50pbag	GRIP	1590.61-1593.90	2.49	49	1592.26	11210	1.10	226	0.11
sum91-53pbag-ox-D-xs.dat	sum91-53pbag	GRIP	1638.45-1643.10	4.75	142	1640.78	12210	1.04	458	0.10
sum91-33pbag3565-xs.col	sum91-33pbag3565	GRIP	1960.22-1964.05	3.83	322	1962.13	23998	1.67	230	0.26
sum92-33pbag-4564ox-D-xs.dat	sum92-33pbag-4564	GRIP	2509.65-2514.03	4.39	809	2511.84	62592	1.67	263	0.26
sum92-33pbag-5a-oxDxs-cor.dat	sum92-33pbag-5a	GRIP	2624.60-2628.98	4.39	517	2626.79	80395	1.67	263	0.26
NG-98_sbs.txt	NG-98	NGRIP	91.33-111.10	19.78	104	101.21	419	2.50	791	0.57
NGRIP-1-22pbag_8.2kyr.txt	NG-8-2-kyr	NGRIP	1221.03-1237.50	16.48	171	1229.26	8244	2.50	659	0.57
NG-99_sbs.txt	NG-99	NGRIP	1322.00-1368.75	46.76	513	1345.38	9507	5.00	935	2.29
NGRIPYD_xsdata_1.dat	ngripYD1	NGRIP	1483.85-1492.45	8.61	140	1488.15	11621	5.00	172	2.29
NGRIPYD_xsdata_2.dat	ngripYD2	NGRIP	1492.45-1502.05	9.61	307	1497.25	11860	5.00	192	2.29
NGRIP-2-11pbag_trans3.txt	NG-trans3	NGRIP	1502.10-1526.50	24.41	859	1514.31	12464	5.00	488	2.29
NGRIP-2-11pbag_trans4a.txt	NG-trans4a	NGRIP	1526.55-1571.85	45.31	1176	1549.21	13474	5.00	906	2.29
NGRIP-2-11pbag_trans4b.txt	NG-trans4b	NGRIP	1571.90-1604.65	32.76	748	1588.28	14361	5.00	655	2.29
ngrip-35pbag-LGM-all.bcol	ngripLGM	NGRIP	1810.62-1818.85	8.24	526	1814.73	24656	1.57	525	0.23
NGRIP-2-11pbag-IS9-1.txt	NG-IS9-1	NGRIP	2085.70-2095.80	10.20	735	2090.75	39812	5.00	204	2.29
NGRIP-2-11pbag-IS9-2.txt	NG-IS9-2	NGRIP	2095.80-2100.05	4.26	212	2097.93	40267	5.00	85	2.29
NGRIP-2-11pbag-IS9-3.txt	NG-IS9-3	NGRIP	2100.05-2109.05	9.01	641	2104.55	40674	5.00	180	2.29
NGRIP-2-11pbag-IS12.txt	NG-IS12	NGRIP	2162.95-2227.65	64.71	3642	2195.30	45714	5.00	1294	2.29
NGRIP-2-11pbag-IS19-1.txt	NG-IS19-1	NGRIP	2499.80-2522.40	22.61	2617	2511.10	71369	5.00	452	2.29
NGRIP-2-11pbag-IS19-2.txt	NG-IS19-2	NGRIP	2530.00-2545.46	15.46	1870	2537.73	71369	5.00	309	2.29
NGRIP-2-11pbag-IS25.txt	NG-IS25	NGRIP	2946.05-2967.70	21.66	2743	2956.88	110940	5.00	433	2.29

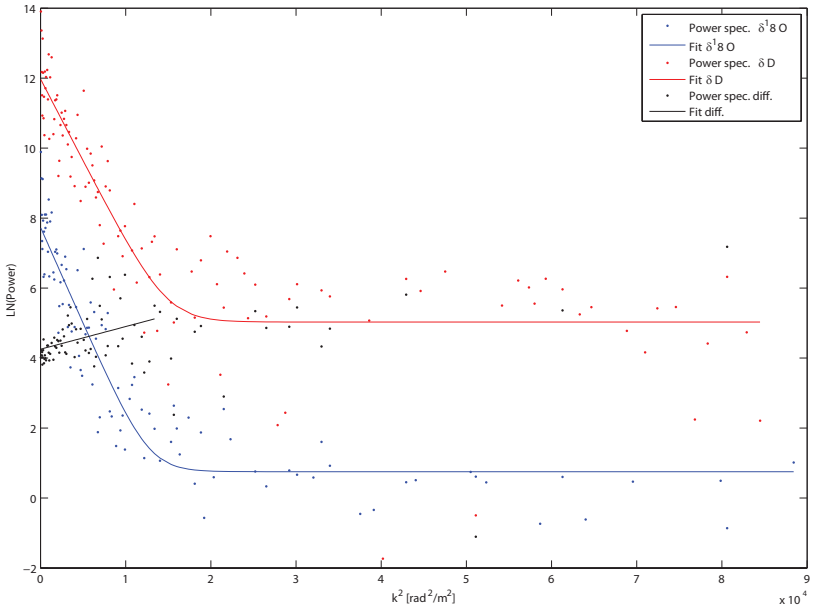

Figure 6.3: A typical non-normalized FFT PSD of a section, here the sum91-53pbag is shown. The variability of the spectral point is typical of the PSD's estimated using the FFT algorithm.

which has similar properties as the power of Equation (6.7) and allows additional room for the flat noisy tail in Figure 6.3 for δ^{18}O and δD . To determine the differential diffusion length the noisy tail is neglected and only the curved part of the signal is fitted to the expression

$$P_{diff} = \frac{P_D}{P_{^{18}O}} = \frac{P_{0_D}}{P_{0_{^{18}O}}} \exp\left(k^2 \Delta\sigma^2\right) \quad . \tag{6.16}$$

The calculated values of the diffusion lengths are listed in Table 6.2 along with the uncertainties. As shown in Figure 6.3 the PSD estimated by the FFT algorithm is rather noisy due to the selected order of the FFT which is chosen to be the number of samples in the ice core section. The estimated PSD has not been normalized to represent true power.

Uncertainty in the fit

The linear fit is encumbered with an uncertainty. This uncertainty is estimated from the 68% confident boundary or one standard deviation given the number of degrees of freedoms (DOF)

$$N_{DOF} = \frac{N_{fit}}{2} - 2 \ , \tag{6.17}$$

where N_{fit} is the number of point involved in the fit. The $\frac{N}{2}$ fraction is an inheritance of the periodicity in the Fourier Transform and the -2 by being a linear fit involving two parameters [Johnsen, 2008].

Section	$\sigma^2_{^{18}O}$ [cm^2]	σ^2_D [cm^2]	$\Delta\sigma^2$ [cm^2]
sum893-22pbag	73.44 ± 4.41	64.35 ± 3.36	12.01 ± 1.94
sum91-50pbag	14.47 ± 4.76	8.15 ± 1.81	1.21 ± 0.27
sum91-53pbag	4.72 ± 0.39	4.65 ± 0.37	1.27 ± 0.26
sum91-33pbag3565	1.94 ± 0.19	1.58 ± 0.17	0.28 ± 0.04
sum92-33pbag-4564	2.65 ± 0.24	2.26 ± 0.20	0.19 ± 0.09
sum92-33pbag-5a	5.05 ± 0.73	4.95 ± 0.62	0.09 ± 0.88
NG-98	34.36 ± 2.26	30.02 ± 1.96	9.32 ± 0.10
NG-8-2-kyr	16.57 ± 1.17	16.70 ± 1.11	2.31 ± 3.34
NG-99	25.92 ± 1.48	22.67 ± 1.42	3.16 ± 0.99
ngripYD1	40.60 ± 11.66	27.36 ± 7.12	1.83 ± 0.57
ngripYD2	11.98 ± 2.43	9.13 ± 2.40	1.24 ± 0.19
NG-trans3	10.68 ± 1.39	9.59 ± 1.65	1.53 ± 0.15
NG-trans4a	12.95 ± 0.91	10.62 ± 0.96	2.25 ± 0.25
NG-trans4b	14.85 ± 1.53	13.71 ± 2.00	1.45 ± 0.16
ngripLGM	3.61 ± 0.22	3.01 ± 0.15	0.62 ± 0.07
NG-IS9-1	19.32 ± 6.33	23.28 ± 8.98	0.97 ± 0.18
NG-IS9-2	6.20 ± 4.96	10.41 ± 7.63	0.05 ± 1.18
NG-IS9-3	5.94 ± 6.31	1.08 ± 4.74	0.52 ± 0.22
NG-IS12	7.24 ± 2.45	7.76 ± 3.22	0.90 ± 0.22
NG-IS19-1	6.17 ± 2.26	7.51 ± 2.80	0.69 ± 0.16
NG-IS19-2	NaN ± NaN	26.08 ± 6.45	0.67 ± 0.54
NG-IS25	NaN ± NaN	NaN ± NaN	NaN ± NaN

Table 6.2: The found diffusion length for the FFT. With subtracted cutting error.

6.3.2 Autocorrelation Method

A second method for calculating the PSD uses the *Wiener-Khinthine Theorem*, which states that the Fourier transform of a function's autocorrelation sequence is the PSD of the function and can be calculated as

$$P(\omega) = \Delta \sum_{m=-\infty}^{\infty} r_{xx}[m] \exp\left(-i2\pi\omega m\Delta\right) \quad , \tag{6.18}$$

where r_{xx} is the autocorrelation sequence and m is the lag. Assuming that the PSD is bandlimited to $\pm f_{nq}$ the inverse transform of the autocorrelation sequence reveals the autocorrelation at zero lag represents the average power of the process,

$$r_{xx}[0] = \int_{-f_{nq}}^{f_{nq}} P(\omega)\mathrm{d}\omega \ . \tag{6.19}$$

If the autocorrelation sequence is strictly real $r_{xx}[-m] = r_{xx}[m]$ the PSD can be calculated from the cosine transform

$$P(\omega) = 2\Delta \sum_{m=0}^{\infty} r_{xx}[m] \cos\left(2\pi\omega m\Delta\right) \quad , \tag{6.20}$$

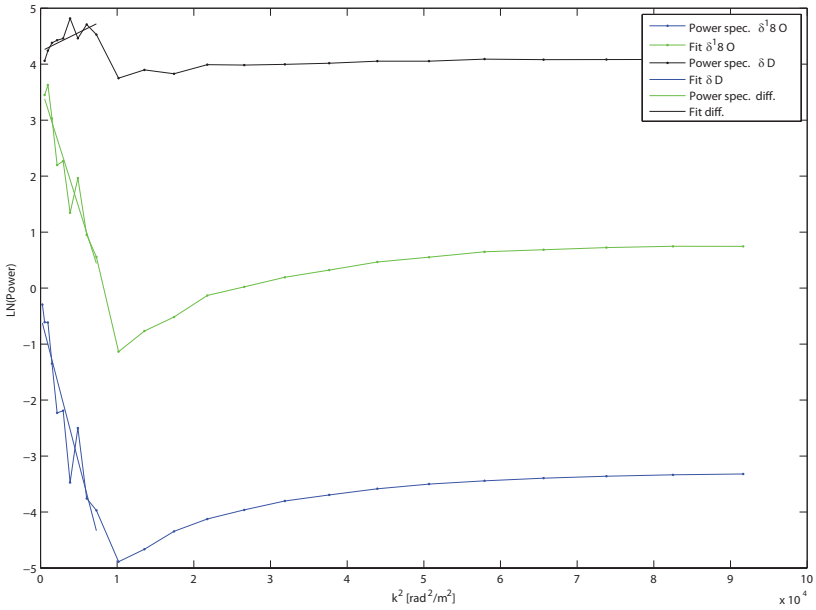

Figure 6.4: Autocorrelation Method Power Spectrum of sum91-53pbag, with 24 lags. The cut-off frequency is clearly seen in the three parameters.

making it an easy way of calculating the PSD. Also the removal of white noise is fairly simple using the autocorrelation method. By definition the white noise is uncorrelated with itself for all lags and its autocorrelation function is a delta function at the zero lag with a magnitude of the white noise variance. Thus, the measuring noise can be removed by subtracting the white noise variance from the zero lag autocorrelation of the function before the cosine transform is calculated. The white noise variance can be estimated from the the PSD of a white noise signal by

$$P_w = \Delta \mathrm{var}_w \ , \tag{6.21}$$

where var_w is the variance resulting in

$$r_w[0] = \mathrm{var}_w = 2P_w f_{nq} \tag{6.22}$$

[Marple, 1987, p. 117].

Figure 6.4 shows an example of the calculated PSD of a ice core section using the autocorrelation method. As for the differential diffusion estimated by FFT algorithm the noise tail is neglected and diffusion lengths are found by fitting Equation (6.16) to the differential PSD and

$$P_i(k) = P_{0_i} \exp\left(-k^2\sigma_i^2\right) \tag{6.23}$$

to the PSD of the two isotopes. The results of the spectrum analysis are shown in Table 6.3. To calculate the PSD the order of the autocorrelation sequence needs to be determined. For all the sections the PSD has been calculated for 20 to 60 lags, and the lag with the lowest uncertainty in the fitted $\Delta\sigma^2$ has been chosen.

Section	$\sigma^2_{^{18}O}$ [cm^2]	σ^2_D [cm^2]	$\Delta\sigma^2$ [cm^2]	Lag
sum893-22pbag	70.99 ± 14.10	60.05 ± 16.30	10.20±0.79	60
sum91-50pbag	6.15 ± 8.67	4.60 ± 8.01	1.55±0.67	26
sum91-53pbag	5.34 ± 0.73	4.35 ± 0.61	0.76±0.30	39
sum91-33pbag3565	2.14 ± 0.25	1.78 ± 0.24	0.36±0.07	24
sum92-33pbag-4564	2.11 ± 0.66	1.84 ± 0.67	0.27±0.07	20
sum92-33pbag-5a	4.99 ± 2.72	4.90 ± 2.58	0.08±0.45	21
NG-98	65.53 ± 5.73	55.43 ± 5.09	10.10±1.22	31
NG-8-2-kyr	38.62 ± 16.09	36.23 ± 15.53	2.38±0.97	32
NG-99	24.84 ± 2.32	23.13 ± 2.20	2.42±0.43	26
ngripYD1	26.69 ± 5.48	24.71 ± 4.81	1.82±0.57	22
ngripYD2	9.94 ± 1.44	8.27 ± 1.45	1.67±0.33	31
NG-trans3	8.88 ± 1.01	7.37 ± 0.98	1.24±0.27	26
NG-trans4a	14.47 ± 1.31	11.36 ± 1.24	2.85±0.24	59
NG-trans4b	13.95 ± 1.86	11.56 ± 1.82	2.00±0.33	51
ngripLGM	3.29 ± 0.56	3.32 ± 0.43	0.34±0.11	40
NG-IS9-1	5.17 ± 6.60	2.78 ± 5.35	0.67±0.94	35
NG-IS9-2	6.45 ± 8.74	5.59 ± 8.15	0.86±1.98	35
NG-IS9-3	2.04 ± 1.76	1.17 ± 1.89	0.87±0.27	35
NG-IS12	3.52 ± 1.26	2.95 ± 0.99	0.97±0.35	35
NG-IS19-1	4.24 ± 5.16	2.40 ± 5.25	1.84±0.43	32
NG-IS19-2	NaN ± NaN	NaN ± NaN	NaN±NaN	NaN
NG-IS25	NaN ± NaN	NaN ± NaN	NaN±NaN	NaN

Table 6.3: The diffusion lengths using the autocorrelation method with subtracted cutting error.

Uncertainty in the fit

From the use of the autocorrelation to estimate the PSD, each point in the estimated PSD is independent of the neighboring points. Hence the uncertainty of the fit is given by one standard deviation given the number of degrees of freedoms (DOF)

$$N_{DOF} = N_{fit} - 2, \tag{6.24}$$

where N_{fit} is the number of points in the fit [Taylor, 1996, p. 189].

6.3.3 Burg's Algorithm

The third method applied to estimate the PSD is the autoregressive method known as Burg's Algorithm or the Maximum Entropy Method (MEM). The method is presented by Burg [1967] and is described in more detail by Andersen [1974] along with a simple way of applying the algorithm on an equal spaced data set $x_1, x_2, ..., x_N$. The algorithm uses the prediction error filter

$(1, -a_{m1}, ..., -a_{mm})$ to estimates the PSD

$$P(\omega) = \frac{P_m \Delta}{\left| 1 - \sum_{n=1}^{m} a_{mn} \exp\left(-i 2\pi \omega n \Delta\right) \right|} \ , \tag{6.25}$$

limited to the interval $\pm f_{nq}$. Here P_m is the output power of the $m+1$ long prediction error filter. The prediction error filter coefficients are calculated as solutions to the matrix equation

$$\begin{bmatrix} \varphi_0 & \varphi_1 & \cdots & \varphi_m \\ \varphi_1 & & \ddots & \vdots \\ \vdots & & & \varphi_1 \\ \varphi_m & \cdots & \varphi_1 & a_0 \end{bmatrix} \begin{bmatrix} 1 \\ -a_{m1} \\ \vdots \\ -a_{mm} \end{bmatrix} = \begin{bmatrix} P_m \\ 0 \\ \vdots \\ 0 \end{bmatrix} \ , \tag{6.26}$$

where φ is the autocorrelation coefficient at a given lag. Following Andersen [1974] the matrix Equation (6.26) is solved by iteration and P_0 is estimated by the average power

$$P_0 = \frac{1}{N} \sum_{n=1}^{N} x_n^2 \ . \tag{6.27}$$

Equation (6.26) has $m+2$ unknowns to be solved from $m+1$ equations, thus an additional term is needed to compute a unique solution to this problem. Burg [1967] suggested to select the filter coefficients which minimize the average power seen through the filter, which for step $m-1 \rightarrow m$ can derived to be

$$\pi_m = \frac{1}{2} \frac{1}{N-m} \sum_{n=1}^{m} \left[\left(x_n - \sum_{k=1}^{m} a_{mk} x_{n+k} \right)^2 + \left(x_{n+m} - \sum_{k=1}^{m} a_{mk} x_{n+m-k} \right)^2 \right] . \tag{6.28}$$

The iteration of Equation (6.26) gives the dependence of the individual filter coefficients on each other

$$a_{mk} = a_{m-1k} - a_{mm} a_{m-1m-k} \ . \tag{6.29}$$

Assuming $a_{m0} = -1$ and $a_{mk} = 0$ for $k \geq m$, this dependence holds for all m. Using this the minimization with respect to a_{mm} simplifies to

$$a_{mm} = \frac{2 \sum_{n=1}^{N-m} \left[\sum_{k=0}^{m} a_{m-1m-k} x_{n+m-k} \sum_{k=0}^{m} a_{m-1m-k} x_{n+k} \right]}{2 \sum_{n=1}^{N-m} \left[\sum_{k=0}^{m} \left(a_{m-1m-k} x_{n+m-k} \right)^2 + \sum_{k=0}^{m} \left(a_{m-1m-k} x_{n+k} \right)^2 \right]} \ , \tag{6.30}$$

and resolves the calculation of a_{mn} in Equation (6.25). Equation (6.26) and (6.29) can also be combined to the regressive formulation of P_m

$$P_m = P_{m-1}(1 - a_{mm}^2) \ , \tag{6.31}$$

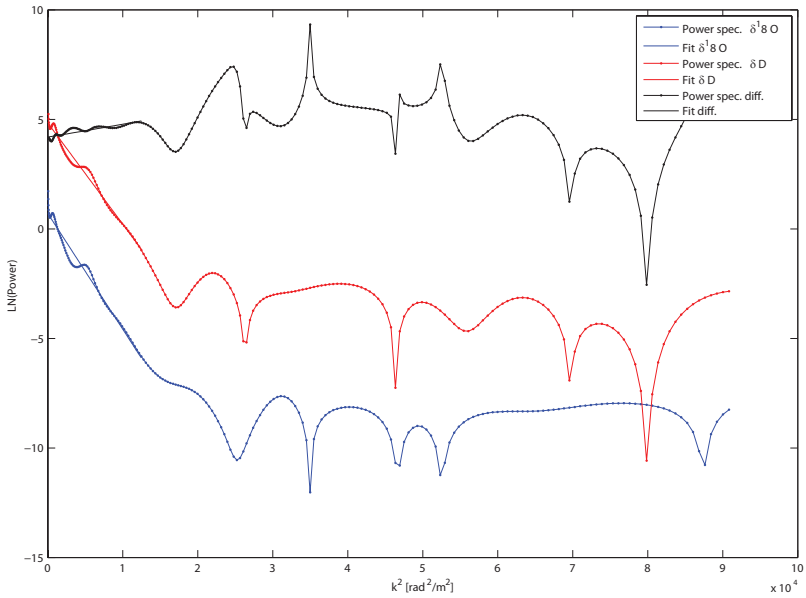

Figure 6.5: Burg's algorithm PSD of sum91-53pbag section. The high variability in the white noise tail is driven by the removal of the measuring noise induces an exaggeration of the local minimums.

which gives the final iterative algorithm of calculating the PSD [Andersen, 1974].

The method has proven to be reliable to handle especially short data sets [Andersen, 1974], which makes it a good candidate for use in spectral analysis of isotopic records from ice cores. As for the autocorrelation method Burg's algorithm also needs a selection of an order to which it is calculated. Different methods of order selection have been developed for autoregressive models. The one applied here is the *Akaike Information Criterion* (AIC).

$$AIC(m) = N \ln(e_m) + 2m \ , \tag{6.32}$$

where e_m is the estimated error variance [Marple, 1987]. The lag minimizing AIC is chosen to be used in the PSD estimation. After having established the methodology behind Burg's algorithm the isotopic data are processed to calculate the PSD and the same procedure as in Section 6.3.2 was used to fit data. Figure 6.5 shows the calculated PSD along with the fit and Table 6.4 lists all the found diffusion lengths using this method.

Uncertainty in the fit

By being an autoregressive model the points in the PSD are not independent of the neighboring points. Hence the DOF can not be estimated from the points in the fit but must be estimated from the number of poles in the fit. Given by the number of sinuosities involved in the fit [Johnsen, 2008]

$$N_{DOF} = N_{sin} - 2 \ . \tag{6.33}$$

Table 6.4: The found diffusion lengths from Burg's algorithm. In the final column is the found order from AIC given for both δ^{18}O and δD . The NG-IS9-2 interstadial section σ^2_D was found to be 1.39 ± 5.17, with the chosen cut-off of the differential diffusion length. But when subtracting the cutting error is subtracted the diffusion length became negative, which is rejected an abbreviated NaN.

Section	$\sigma^2_{^{18}O}$ [cm^2]	σ^2_D [cm^2]	$\Delta\sigma^2$ [cm^2]	Order
sum893-22pbag	61.33 ± 10.28	50.86 ± 11.24	10.47 ± 3.23	49 29
sum91-50pbag	8.02 ± 0.82	7.14 ± 0.55	0.95 ± 0.55	30 23
sum91-53pbag	5.17 ± 0.26	4.50 ± 0.20	0.62 ± 0.12	20 20
sum91-33pbag3565	1.80 ± 0.10	1.51 ± 0.10	0.29 ± 0.05	20 20
sum92-33pbag-4564	2.03 ± 0.15	1.98 ± 0.13	0.05 ± 0.11	60 45
sum92-33pbag-5a	5.20 ± 0.92	5.14 ± 0.92	0.07 ± 0.22	27 20
NG-98	64.08 ± 11.00	54.76 ± 11.00	10.16 ± 1.44	28 28
NG-8-2-kyr	20.27 ± 1.12	28.09 ± 1.12	2.36 ± 0.88	40 21
NG-99	23.80 ± 1.34	21.17 ± 1.25	2.63 ± 0.31	23 23
ngripYD1	25.02 ± 8.15	23.92 ± 9.64	1.92 ± 1.77	24 25
ngripYD2	9.67 ± 0.79	8.00 ± 0.79	1.67 ± 0.17	21 21
NG-trans3	5.12 ± 8.33	5.22 ± 8.10	1.33 ± 1.13	33 33
NG-trans4a	13.52 ± 1.19	11.32 ± 0.90	2.05 ± 0.66	20 28
NG-trans4b	14.93 ± 0.95	13.14 ± 0.80	1.50 ± 0.30	21 21
ngripLGM	3.43 ± 0.12	2.99 ± 0.12	0.44 ± 0.12	25 25
NG-IS9-1	3.02 ± 1.28	1.99 ± 1.26	1.03 ± 0.23	30 30
NG-IS9-2	1.95 ± 5.50	NaN ± NaN	2.84 ± 3.93	60 58
NG-IS9-3	5.36 ± 3.73	4.38 ± 4.57	1.17 ± 1.09	20 20
NG-IS12	5.67 ± 4.14	5.29 ± 4.23	0.38 ± 0.67	26 26
NG-IS19-1	8.54 ± 1.86	8.53 ± 1.99	0.33 ± 0.23	20 20
NG-IS19-2	16.07 ± 8.51	13.11 ± 6.90	1.11 ± 3.05	20 20
NG-IS25	46.52 ± 7.74	45.43 ± 7.32	1.10 ± 1.45	25 31

7 Results and Discussion

The previous chapters have all contributed with small pieces to the puzzle of estimating past temperatures on the Greenlandic ice sheet from differential diffusion. The paleotemperatures will be estimated based on the limited number of sections available from the GRIP and NGRIP ice cores.
The three PSD estimators did not give a clear picture of which method is superior to the others. A detailed discussion of the methods will be given in the first part of this chapter. Before turning to the main topic of temperature reconstruction considerations of the deep ice diffusion will be discussed.

7.1 Spectral Estimates of Differential Diffusion

The estimated differential diffusion lengths found by the three PSD estimators are listed in Table 7.1 to ease the individual comparisons. Judging from the variation in the estimated diffusion lengths and uncertainties, none of the methods are superior to the others. Following Taylor [1996, p. 175] a weighted mean solution can be calculated by weighting the uncertainties

$$\Delta\sigma^2_{mean} = \frac{\sum w_i \Delta\sigma_i^2}{\sum w_i} \ , \tag{7.1}$$

where the weights are $w_i = \frac{1}{\epsilon_i^2}$, and ϵ is the fitted uncertainty of an independent measurement. Hence the uncertainty on the weighted mean is

$$\epsilon_{mean} = \frac{1}{\sqrt{\sum w_i}} \ . \tag{7.2}$$

The deviation from the weighted mean is used as a measure for the comparison of the three methods. Figure 7.1 shows this deviation as a function of the number of samples in the section. The deviations are scattered in the plotting area. In order to see any common features of the methods a

Table 7.1: Spectral estimates of differential diffusion using the three methods. A weighted mean solution is also listed. In the case not all of the methods were able to determine the diffusion, the weighted mean is simply found from the available diffusion estimate.

Section	$\Delta\sigma^2_{FFT}$	$\Delta\sigma^2_{Auto}$	$\Delta\sigma^2_{Burg}$	$\Delta\sigma^2_{mean}$
sum893-22pbag	12.01 ± 1.94	10.20 ± 0.79	10.47 ± 3.23	10.46 ± 0.71
sum91-50pbag	1.21 ± 0.27	1.55 ± 0.67	0.95 ± 0.55	1.20 ± 0.23
sum91-53pbag	1.27 ± 0.26	0.76 ± 0.30	0.62 ± 0.12	0.73 ± 0.10
sum91-33pbag3565	0.28 ± 0.04	0.36 ± 0.07	0.29 ± 0.05	0.30 ± 0.03
sum92-33pbag-4564	0.19 ± 0.09	0.27 ± 0.07	0.05 ± 0.11	0.20 ± 0.05
sum92-33pbag-5a	0.09 ± 0.88	0.08 ± 0.45	0.07 ± 0.22	0.07 ± 0.19
NG-98	9.32 ± 0.10	10.10 ± 1.22	10.16 ± 1.44	9.33 ± 0.10
NG-8-2-kyr	2.31 ± 3.34	2.38 ± 0.97	2.36 ± 0.88	2.37 ± 0.64
NG-99	3.16 ± 0.99	2.42 ± 0.43	2.63 ± 0.31	2.59 ± 0.24
ngripYD1	1.83 ± 0.57	1.82 ± 0.57	1.92 ± 1.77	1.83 ± 0.39
ngripYD2	1.24 ± 0.19	1.67 ± 0.33	1.67 ± 0.17	1.50 ± 0.12
NG-trans3	1.53 ± 0.15	1.24 ± 0.27	1.33 ± 1.13	1.46 ± 0.13
NG-trans4a	2.25 ± 0.25	2.85 ± 0.24	2.05 ± 0.66	2.53 ± 0.17
NG-trans4b	1.45 ± 0.16	2.00 ± 0.33	1.50 ± 0.30	1.54 ± 0.13
ngripLGM	0.62 ± 0.07	0.34 ± 0.11	0.44 ± 0.12	0.52 ± 0.05
NG-IS9-1	0.97 ± 0.18	0.67 ± 0.94	1.03 ± 0.23	0.98 ± 0.14
NG-IS9-2	0.05 ± 1.18	0.86 ± 1.98	2.84 ± 3.93	0.42 ± 0.98
NG-IS9-3	0.52 ± 0.22	0.87 ± 0.27	1.17 ± 1.09	0.67 ± 0.17
NG-IS12	0.90 ± 0.22	0.97 ± 0.35	0.38 ± 0.67	0.88 ± 0.18
NG-IS19-1	0.69 ± 0.16	0.52 ± 0.43	0.33 ± 0.23	0.57 ± 0.13
NG-IS19-2	0.67 ± 0.54	NaN ± NaN	1.11 ± 3.05	0.68 ± 0.53
NG-IS25	NaN ± NaN	NaN ± NaN	1.10 ± 1.45	1.10 ± 1.45

second order polynomial is fitted to the deviations for each method. The second order polynomial is chosen to emphasize the simplest structure of the deviations. A first order polynomial would be the natural choice but showed no trend in the data. The polynomial roots are of special interest and may indicate how well a method handles a certain number of samples.

A general summary and comparisons of the methods are given below:

FFT Algorithm: The spectral resolution of the FFT algorithm is high and results in the lowest average uncertainty of the three methods. As seen in Figure 7.1 the method has two roots within the span of samples in a section, one at 334 samples and one at 1325 samples. A drawback is the noisiness of the calculated spectra by the FFT algorithm as shown in Figure 6.3, which is representative for the estimated PSD by the FFT. Also removing measurement noise, which is done by subtracting the mean of the measuring noise tail from the estimated PSD, from the PSD is not ideal and results in enhanced local minima especially at high frequencies. As long as the red part of the spectrum is orders of magnitudes larger than the tail, this is not a problem. However, this is not always the case as seen from the estimated PSD of actual ice core data, which affects the estimated diffusion length.

Autocorrelation method: The Autocorrelation method is limited by the

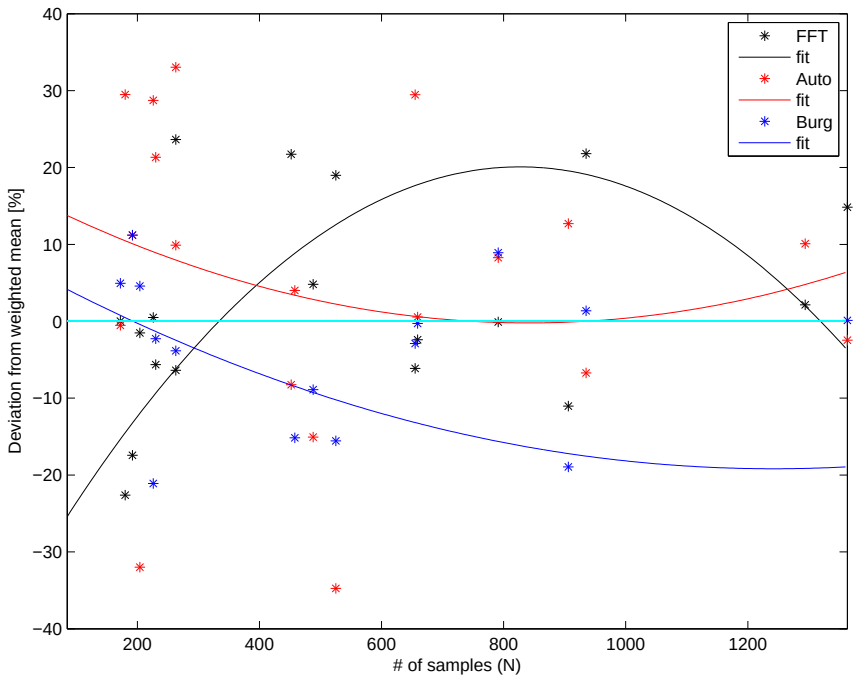

Figure 7.1: The deviation from the weighted mean is plotted for the three methods. A second order polynomial has been fitted to the points to emphasize a tendency in data. Outliers above 100% have been removed to simplify the plot.

number of points being cosine transformed, which is equal to the number of lags selected. Thereby the statistics of the fitted diffusion length estimate are limited, but the selected points have the advantage of being independent. Furthermore the robustness of removing the measuring noise gives the Autocorrelation method an advantage compared to the other two methods.
Relying on the deviation from the weighted mean, the Autocorrelation method seems to be better for resolving longer data sets than the other two methods. The two roots of the polynomial are almost identical and lie around 850 samples.

Burg's algorithm: The Burg's algorithm has the lowest root of the fitted polynomials in Figure 7.1 at about 200 samples. The autoregressive nature of this method seems to be a robust way to suppress the noisiness of the estimated PSD of isotopic data. This is seen by the ability of the method to retrieve the diffusion signal from all ice core sections, even the deep ones where the differential diffusion is close to the detection minimum of the methods. However, Burg's algorithm has the same problem as the FFT regarding the correction for measuring noise.

The short discussion above indicates that none of the methods are superior to the others. Furthermore none of the methods points to the same value of the differential diffusion length, but each are within the uncertainties of the others. To highlight one method, Burg's algorithm is the only one able

to resolve the deep sections. It can also be seen that the number of samples in a section is a main factor in determining the precision of a method and the Autocorrelation method is a good alternative for longer sections since it handles the measuring noise in a robust way. The weighted mean is an unsupervised way of combining the three PSD estimators to estimate the differential diffusion length. However, the computational demands will increase with a larger number of sections.
An alternative solution could be to subtract the measuring noise from the zero lag autocorrelation when calculating the prediction error filter in Burg's algorithm. This is an approach which is seemingly straight forward, but must be postponed to future work. It should be investigated thoroughly before trying other methods of PSD estimation.

7.2 Ice Diffusivity in the NGRIP Core

The estimated diffusion lengths from the NGRIP sections are compared with the modelled diffusion from Section 5.4 in Figure 7.2. The estimated diffusion lengths in the figure have been found using Burg's algorithm. Similar plots for the FFT algorithm and Autocorrelation method are shown in Appendix B. All estimated diffusion lengths are within the uncertainties of the model solution and no additional diffusion is seen in the Holocene. This contradicts the finding of Johnsen et al. [2000] for the GRIP ice core.

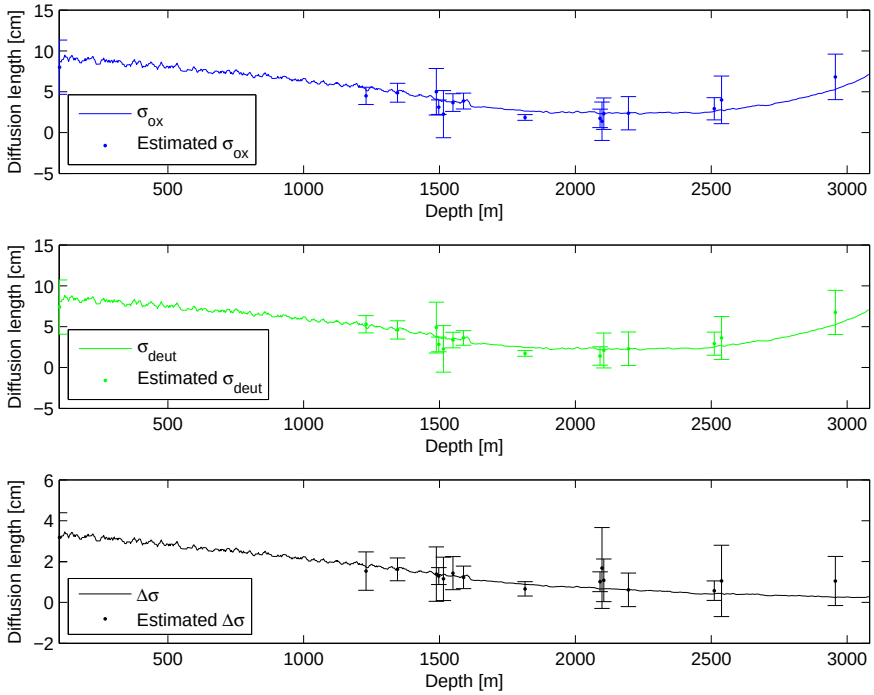

Figure 7.2: The estimated diffusion lengths found using Burg's algorithm compared to the modelled diffusion lengths for the NGRIP ice core. Similar figures for the FFT and the Autocorrelation methods can be found in Appendix B.

The last seven sections in the NGRIP are all dated to Greenland interstadials. When analyzing the differential diffusion length of these deep sections, the estimated differential diffusion length is generally larger than the model[1]. An explanation for the longer differential diffusion length could be that the sections have experienced a warmer climate than modelled by the isotope borehole temperature reconstruction, which may not be fully able to resolve the fast climate shift at the interstadials. More sections are needed to confirm this suspicion.
As mentioned previously the ice self diffusion is playing an important role in the observed diffusion below the depth of about 2100 meters. Below this depth, the estimated differential diffusion lengths become almost nonexistent as seen from the error bars. Hence the temperature reconstruction based on the differential diffusion is proposed to be limited to ice above 2100 meters or about 40 kyr in the NGRIP ice core.

7.3 Paleoclimatic Record from Differential Diffusion

The estimated differential diffusion length is stretched according to Equation (5.21) to estimate the differential diffusion length of the section when it was located at the effective pore close-off in the firn column. The strain rate used in the equation is modelled by the ss09sea[2]. To estimate the surface temperature from Figure 5.3 the accumulation history is needed, which is found by stretching the annual layer thickness from GICC05 according to the strain rate from the ss09sea. The calculated differential diffusion length at the effective pore close-off is listed in Table 7.2 for the weighted mean solution along with the estimated temperatures.
To compare the estimated temperatures to existing temperature reconstructions the weighted mean solution is plotted in Figure 7.3 against the isotope temperature reconstruction forced to fit the measured borehole thermometry at the drill site of the GRIP [Johnsen et al., 1995] and NGRIP ice cores [Johnsen, 2008], respectively.

7.3.1 GRIP Record

Only three sections from the GRIP ice core have been available for this study in the depth interval between the effective pore close-off and the depth of 2100 m. The weighted mean solution of each of the three GRIP sections

[1]The two deep sections from the GRIP ice core mentioned in Chapter 6 are discussed in Johnsen et al. [2000] for case the of δ^{18}O diffusion and will not be discussed further.

[2]The ss09sea is preferred compared to the Monte Carlo solution given in Chapter 4, because a high time resolution is needed.

Table 7.2: The strain corrected differential diffusion length $\Delta\sigma$ [cm] for the weighted mean solution is listed along with the estimated surface temperatures T [°C] using the three PSD estimators. The weighted mean solution is listed in the last three columns. The estimated deviations from the temperatures are calculated from the uncertainty in the fitted diffusion lengths.

		FFT			Auto			Burg			Mean		
	σ_{tau}	min	T	max	min	T	max	min	T	max	min	T	max
sum91-50pbag	9.71	-37.56	-33.94	-30.90	-38.60	-30.20	-24.57	-49.31	-37.42	-30.67	-37.10	-34.01	-31.46
sum91-53pbag	6.62	-41.25	-38.03	-35.36	-51.56	-45.06	-40.57	-50.50	-47.72	-45.42	-47.47	-45.59	-43.87
sum91-33pbag3565	6.48	-54.48	-52.57	-50.96	-52.19	-49.50	-47.25	-54.48	-52.19	-50.23	-53.16	-51.94	-50.76
NG-98	9.34	-34.21	-34.06	-33.89	-34.73	-32.81	-31.12	-34.98	-32.71	-30.71	-34.20	-34.05	-33.87
NG-8-2-kyr	8.28	NaN	-37.68	-24.20	-45.40	-38.11	-33.11	-44.74	-38.23	-33.65	-42.59	-38.19	-34.72
NG-99	10.95	-35.20	-29.52	-25.38	-36.49	-33.61	-31.20	-34.30	-32.37	-30.69	-34.09	-32.55	-31.26
ngripYD1	9.98	-42.53	-37.34	-33.44	-42.66	-37.40	-33.51	-68.28	-36.70	-26.88	-40.78	-37.34	-34.53
ngripYD2	8.34	-51.41	-49.32	-47.50	-48.36	-45.54	-43.16	-46.94	-45.54	-44.23	-47.94	-46.93	-45.88
NG-trans3	8.37	-46.51	-45.14	-43.87	-50.95	-47.86	-45.31	-69.04	-47.00	-38.73	-47.00	-45.72	-44.62
NG-trans4a	15.51	-36.76	-35.04	-33.50	-32.83	-31.56	-30.34	-41.78	-36.37	-32.28	-34.38	-33.31	-32.35
NG-trans4b	10.25	-39.87	-38.29	-36.87	-36.27	-33.66	-31.40	-40.95	-37.80	-35.19	-38.64	-37.37	-36.22
ngripLGM	5.47	-54.53	-53.08	-51.77	-64.45	-60.09	-56.89	-60.79	-57.15	-54.30	-56.39	-55.12	-53.97

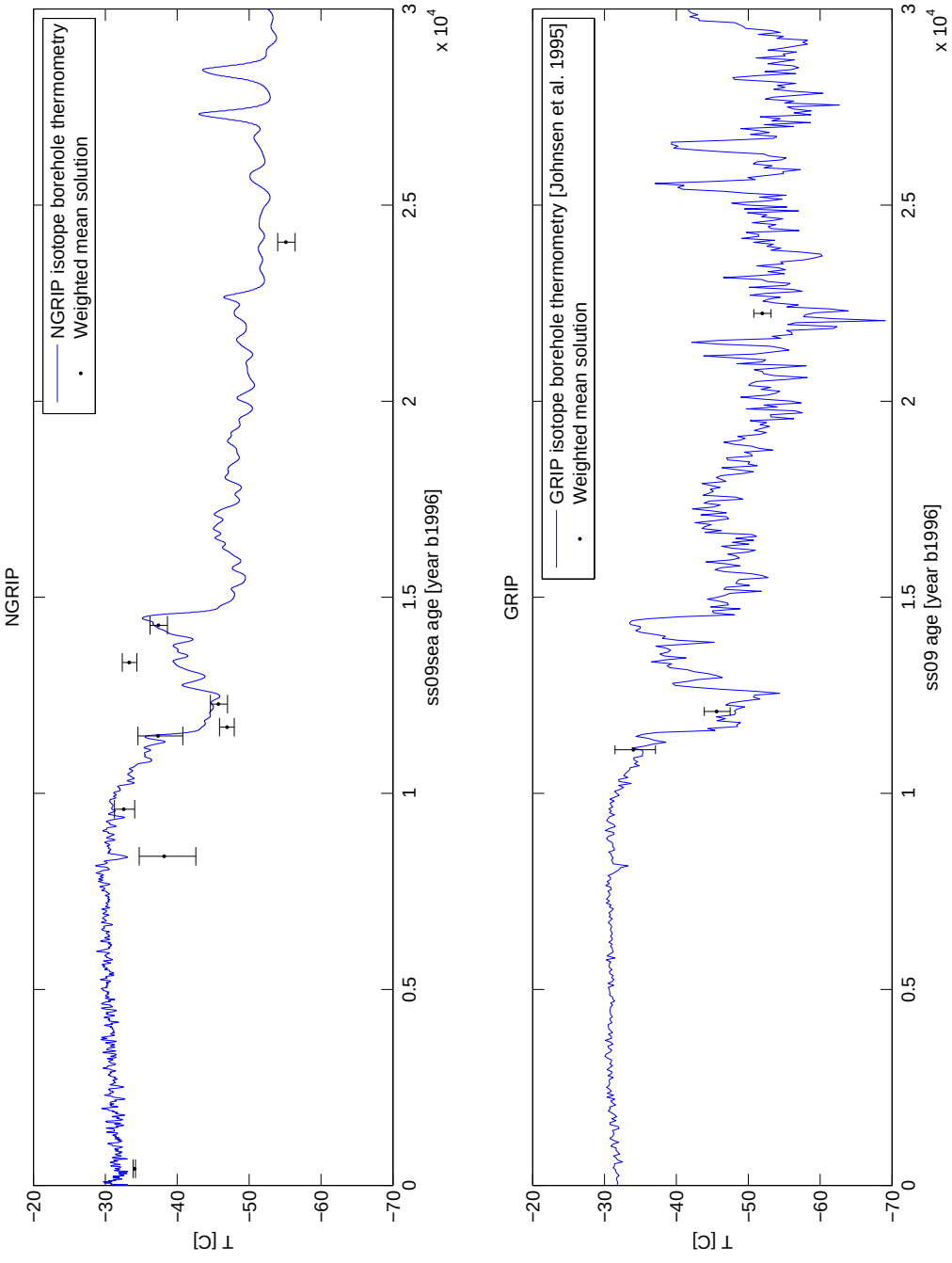

Figure 7.3: Temperature reconstruction of the two ice cores, NGRIP in the upper panel and GRIP in the lower, compared with the combined isotopic borehole thermometry. The non symmetric uncertainties in the temperature estimates are due to the uncertainties in the estimated $\Delta\sigma^2$ combined with the logarithmic nature of Figure 5.3.

is depicted in the lower panel of Figure 7.3. Both of the sections sum91-50pbag and sum91-53pbag are in agreement within 2 K of the Johnsen et al. [1995] temperature reconstruction. Whereas the section sum91-33pbag3565 is about 7 K warmer than predicted by Johnsen et al. [1995] at the LGM. This must be a result of the section covering about 300 years including some of the warmer climate predating the LGM.

7.3.2 NGRIP Record

Above the depth of 2100 meters 11 sections are available from the NGRIP ice core but the last two are too close to the 2100 meter boundary to be trusted as seen by the NG-IS9-2 section, which have error bars below zero. Thereby only nine sections are available from the NGRIP ice core for the temperature reconstruction. When comparing the two reconstructions for NGRIP in Figure 7.3, the differential diffusion length reconstruction is about 2 K colder than the isotope borehole solution, but similar within the uncertainties of the two methods. However, at the 8.2 kyr event the deviation is 4.5 K colder than the isotope borehole temperature. The isotope borehole temperature reconstruction seems to underestimate the cold shift of this event by only showing about a 3 K shift. Leuenberger et al. [1999] found the climate shift at 8.2 kyr to be between 5.4 K and 11.7 K using $\delta^{15}N$ to calibrate the $\delta^{18}O$ paleothermometer, which is in better agreement with the differential diffusion temperature estimate. The other big climate shift from the YD to the early Holocene is recorded by the differential diffusion temperature as a 10 K shift. This lies between the 7 K seen in the GRIP δ^{18}O record and the 15 K seen by Severinghaus et al. [1998] in the GRIP $\delta^{15}N$.
The only section showing a warmer temperature based on the differential diffusion is the section covering the Allerød, which is about 5 K warmer than the borehole estimate and will be discussed further in Section 7.4.

7.4 Processing Long Records

The 22 sections available for this study of differential diffusion in Greenlandic ice cores has made it possible to manually look at each PSD produced and to select the white noise tail and cut-off frequency. If a continuous record of fine cuts in both δ^{18}O and δD is available that spans the full ice core length this manual procedure is not possible. An automated method of estimating the beginning of the measuring noise tail and selecting the diffusion length cut-off frequency has to be invented to handle large data sets. A number of approaches have been tested to estimate the cut-off frequency during the early phases of this study, but none of them have proven to be reliable on all of the data sets used. For example, the approaches have been to look for a certain variance limit associated with the white noise tail, the variation from point to point, or filtering the PSD's to see a cut-off point, all without

giving a clear answer to where the cut-off frequency should be placed. Not even the more well behaving Burg's algorithm has shown a clear response to the methods applied. More work is needed to see if any statistical way of determining the cut-off frequency is possible. This could, for example, be to apply some sort of iteration method where the PSD is evaluated a number of times before determining the final cut-off frequency which fits the section the best. The diffusion length cut-off frequency will be discussed further in Section 7.5.5.

Another question, when working with longer data sets is how to divide the data into smaller pieces which can be processed by the chosen PSD algorithm. To investigate this, a long data set is needed. Fortunately the sections ngripYD1, ngripYD2, NG-trans3, NG-trans4a and NG-trans4b are a continuous record of 5 cm samples, spanning 124.7 m of ice cores with 2494 samples covering most of the transition into the Last Glacial. Thus this record is ideal to test how to subdivide the data and to find a running mean differential diffusion length. Based on the advantages discussed in Section 7.1, Burg's algorithm has been chosen for this test. As seen in Figure 7.1 Burg's algorithm behaves nicely in a short data set around 200 samples. 200 is selected as the window size N of the running mean estimation of diffusion lengths. The window is moved ΔN samples. The process is repeated until the differential diffusion length is determined for the full data set revealing a more detailed estimation of the differential diffusion length. In Figure 7.4 both the estimated $\Delta\sigma^2$ in the upper panel and the temperature reconstruction in the lower panel are shown. The NGRIP isotopic borehole thermometry is also shown for comparison. To pinpoint the depth scale on the age scale the figure is showing the Younger Dryas, Allerød and Bølling periods, corresponding to the green area in Figure 1.2. The two reconstructions are following each other well as for the discrete temperature reconstruction. By choosing a window size of 200 samples and having a sampling size of 5 cm, each point in the figure estimates the mean of ten meters of ice. Thereby some stretching may be needed to match the GICC05 chronology and the isotope borehole thermometry reconstruction.

As for the section NG-trans4a the Allerød is again seen as being just as warm or even warmer than the Bølling, which is not observed in previous temperature reconstructions from isotopes. It is hard to say which of the two reconstructions in Figure 7.4 should be trusted as the best temperature reconstruction of this time period. But the period is also known to spell trouble in Greenlandic ice flow modelling. The problems may be ascribed to a change in the moisture source or trajectory, where more of the accumulation is coming from North in the winter time and precipitating under a stronger inversion layer [Jouzel et al., 1997]. Since the transition from the Holocene into the Last Glacial suffers from strong climatic shifts, the period is not an ideal place to test the appliance of the running mean differential diffusion estimation. Despite this, the temperature reconstruction deter-

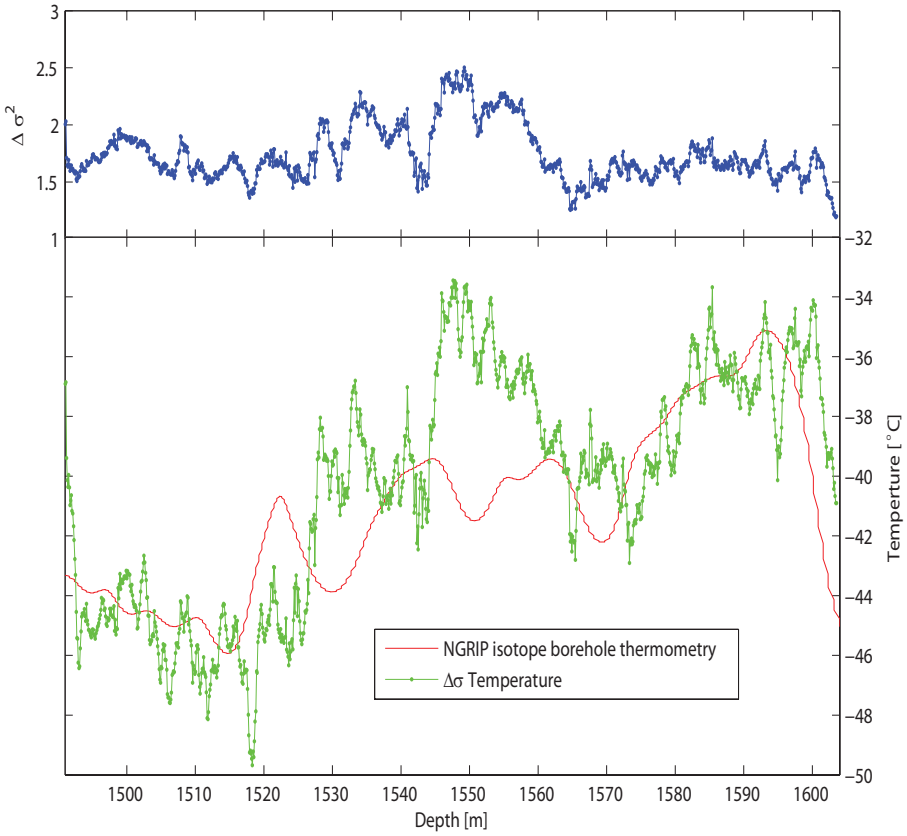

Figure 7.4: Running mean estimation of the differential diffusion length. The estimated differential diffusion length is using a 30 lag Burg's algorithm, a window size of $N = 200$ and $\Delta N = 2$. In the top panel is the estimated differential diffusion length and in the lower panel is this diffusion length converted into a temperature estimate. A warming not seen by the isotopes is seen by the diffusion record in the Allerød, which seems to have the same magnitude as the Bølling. In the power spectrum no clear cut-off nor measuring noise tail is found, hence the differential diffusion length is estimated from the full spectrum below the Nyquist frequency.

mines similar surface temperatures as the borehole isotope reconstruction, confirming the applicability of the differential diffusion method.

7.5 Bias in the Presented Paleothermometer

The paleoclimatic reconstruction based on the differential diffusion length has removed many of the biasing elements described in Chapter 2 for the δ^{18}O paleoclimatic record. Still the method is not fully independent of error sources. Most of them are associated with the evolution of the ice sheet and the ice flow with respect to the core in question.

7.5.1 Firn Depth

To calculate the diffusion length for a given temperature and accumulation point the effective pore close-off depth in the firn is needed. In this work an effective pore close-off has been defined to a density of 804 $\frac{\text{kg}}{\text{m}^3}$, but deviations from this value in the actual firn column will affect the predicted temperature. A 10 % decrease in the close-off density is equivalent to a 0.2 K increase in the estimated temperature for a section in a depth of 1500 m.

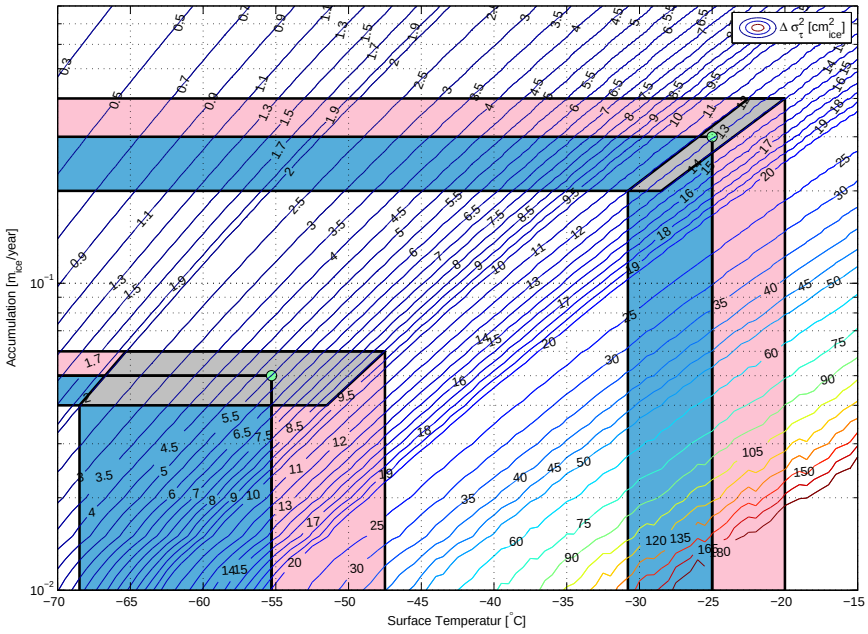

Figure 7.5: Exaggerated example of how an error in the strain will effect the estimated temperature an ice core section. The logarithmic nature of the isolines ensurers that the temperature estimate is better constrained in the warm sector than in the cold.

7.5.2 Flow Model Induced Uncertainties

Along with the uncertainties associated with the fitted diffusion lengths the flow model also introduces an uncertainty via an error on the estimated strain rate used to stretch the sections. This affects the estimation of the temperature based on Figure 5.3. In Figure 7.5 two examples are shown where the uncertainty in the accumulation and strain rate estimate affects the temperature estimation. The uncertainty in the accumulation is along the vertical axis and the uncertainty in the estimated strain is either increasing or decreasing the estimated differential diffusion length. The two grayish areas represent the solution space of a temperature estimate given the two uncertainties. Seen in this exaggerated example, the semi-logarithmic nature of the contour plot contributes to the a better constrained temperature estimate in the warm part (reddish area) than in the cold part (blueish area). This gives the determined temperature an unequal uncertainty due to the flow model uncertainties. This is the same response as the uncertainty caused by the estimated diffusion lengths that are plotted as error bars in Figure 7.3.

7.5.3 Ice Sheet Evolution

The temperature reconstructions have to be corrected for the evolution of the surface elevation to give a real estimate of climate changes at the drill site according to the lapse rate. Due to the limited number of sections in the two cores the temperature estimate is given without any correction of the

surface elevation. The models calculating the surface elevation evolution are not all agreeing on the magnitude of the surface elevation change [Vinther et al., 2008a]. But when a long continues record of the differential diffusion length is available, the estimated temperature record has to be corrected for the elevation to yield a climatic record. Different methods can be used to examine the elevation history at an ice core site. The total gas content in the ice is dependent on the elevation of the site where the gas is encapsulated. The isotope record can also be used to some extent. When comparing the δ^{18}O records for the Renland and the Agassiz ice cores with the ones from the central part of Greenland, Vinther et al. [2008a] find a surface elevation 10 kyr b2k at NGRIP approximately 200 m higher than at present. This is higher than most models predict but in agreement with the total gas content measured in the ice [Vinther et al., 2008a]. Such an increase in the surface elevation gives a cooling of the site of about 2 K by the dry adiabatic lapse rate. This emphasizes a need for an accurate past surface elevation profile to interpret the climate signal retrieved from the ice cores.

7.5.4 Sample Size of the Measured Water Isotopes

The effect of cutting discrete samples vanishes in the differential diffusion length. The sample size is affecting the Nyquist frequency which decreases when the sample size increases. If the Nyquist frequency is too small the white noise tail of the measuring noise tends to disappear. For the deep sections of the 5 cm samples from the NGRIP ice core the tail is starting to disappear and in some of PSD the tail is absent. Thereby the 5 cm samples may be a reasonable limit for the sample size. If the sample size is large then the measuring noise has to be estimated from a priori knowledge of uncertainty of the mass spectrometer measurements.

7.5.5 Cut-off

As described in Section 6.2.3 the cut-off frequency has been hard to select in an automated way. The selected cut-off for the linear fit of the diffusion length has also proven difficult to select even by hand. Two of the sections are shown in Figure 7.6, where the estimated differential diffusion length is given as a function of the cut-off frequency. The two sections show that the differential diffusion length fluctuates as a function of the cut-off frequency and is far from constant. One might argue that these findings are compromising the method, but as the figure shows the uncertainties also varies in the frequency range. At the frequency bands (reddish area) with almost constant estimates of the differential diffusion lengths the uncertainties are seen to reach a minimum. Thus, these areas must be the appropriate places to estimate the differential diffusion length of the section. Similar values are observed when comparing the mean of the reddish area to the values found

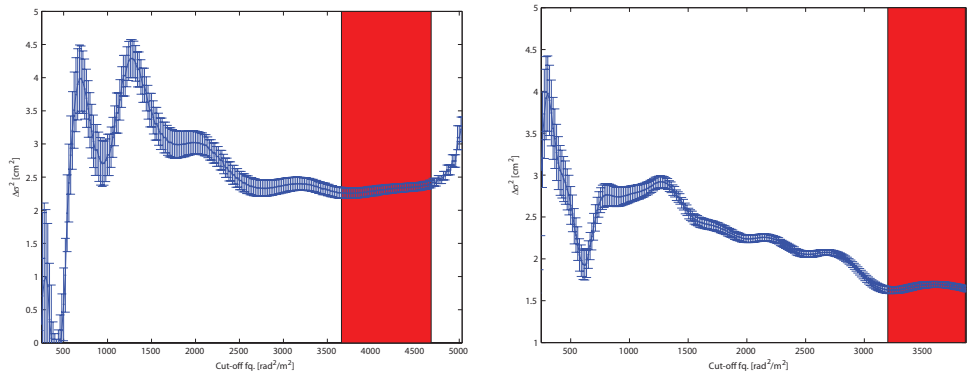

(a) NG-8-2-kyr

(b) NG-trans4a3

Figure 7.6: The area for the fit is important for the found value of $\Delta\sigma^2$. Here two of the ssections are plotted as a function of cut-off frequency and estimated diffusion length from the cut-off. As seen is the diffusion length varying with the cut-off frequency, but having more or less stable periods indicated in red.

by hand in Table 7.1. These findings further support the idea discussed in Section 6.2.3 of making some sort of iteration process to automate the estimation of the diffusion length. However they also verify that the hands on approach done in this study is feasible.

8 Conclusion

This study examined isotopic diffusion employing different methods to give a comprehensive picture of the processes involved in estimating the paleoclimate record of the Greenlandic ice sheet from the diffusion of water isotopes. It involves four independent parts of Glaciology all needed as pieces of the puzzle of reconstruction of paleotemperatures from the diffusion processes. The findings of the four areas, densification, ice flow, firn and ice diffusion, and spectral analysis of the isotopic record will be concluded individually.

The simple empirical Herron-Langway-model is found to be superior to the more complex Arnaud-model in estimating the firn densification. Hence the Herron-Langway-model is the one used to estimate the densification in firn.

To govern the ice flow and thinning at the drill site a Dansgaard-Johnsen model has been used to describe the horizontal velocity field and the flow parameters have been estimated using Monte Carlo methods. In this study the accumulation has been included in the Monte Carlo method as a model parameter in the inverse problem solution, whereas in other ice flow studies the accumulation has been estimated from the δ^{18}O record in the ice core. The uncoupling of accumulation from the δ^{18}O causes the model to be more computational demanding and the time resolution had to be reduced to the point where the flow model is no longer capable of accounting for the rapid climatic changes that happened in the transition from the Holocene into the Last Glacial. However, the model verifies the coupling of the accumulation to the isotopes as done by ss09sea. ss09sea is then used when an estimate of the strain rate is needed.

The modelled densification and ice flow are used to model the diffusion in the firn and ice matrix. The isotopic diffusion in the firn is found to be dependent on the surface temperature fluctuations propagation into the

firn column. This results in a longer diffusion length than predicted using isothermal firn in equilibrium with the annual mean temperature. The temperature reconstruction from a combined isotope and borehole thermometry and the modelled strain rate from the ss09sea is used to model the diffusion length in the ice matrix. The temperature reconstruction based on the diffusion processes is proposed to be limited to sections above 2100 meters.

To estimate the diffusion length from actual ice core data, three different methods of numerical power spectral density estimation have been applied without finding a superior method. However, Burg's algorithm is the only one able to retrieve the diffusion signal from all 22 sections from the GRIP and NGRIP ice cores. However, compared to the Autocorrelation method it lacks a better way of removing the measuring noise.

Based on a weighted mean of the three power spectral estimators the paleoclimatic record is retrieved from 12 ice core sections. When comparing the estimated temperature from differential diffusion for the NGRIP ice core with the combined isotope and borehole thermometry temperature reconstruction the differential diffusion length reconstruction estimate is about 2 K colder, whereas the three sections in the GRIP ice core is estimated a little warmer than the combined isotope and borehole thermometry temperature reconstruction. Accounting for the uncertainties in the two methods of estimating paleoclimate the derived temperatures are found to be equivalent. Out of the 12 sections two sections stand out, both in the NGRIP record. For the section covering the Allerød warming the estimated temperatures are found to be equivalent to the Bølling and about 5 K warmer than the isotopic reconstruction. On the other hand, the temperature estimate of the section covering the 8.2 kyr event is estimated to be 4.5 K colder than the isotopic borehole reconstruction predicts but the differential diffusion temperature estimate is in agreement with other studies of the 8.2 kyr event.

The diffusion processes investigated here can be seen as a new ice core paleothermometer directly measuring the surface temperature in the time span of an ice core section. It may be applied as a continuous temperature reconstruction of the last 40 kyr when the needed isotopic data is available. However, the tested method is not the final solution for an ice core paleothermometer based on differential diffusion lengths. Further development is needed.

9 Outlook

The study of the differential diffusion length as paleoclimatic proxy can be developed even further in the future to provide a strong tool to estimate the temperatures of snow covered areas back in time. However, different areas have to be better understood to ensure the creditability of the method.

The power spectra density estimation has to be developed to give a better estimate of the diffusion length. One way could be, as proposed in Chapter 7 correct Burg's algorithm for the measuring noise at the zero lag autocorrelation. This method will hopefully be able to handle short sections which are needed to estimate the running mean solution of the diffusion length when analyzing long continual records of both δ^{18}O and δD. Hopefully a long record will be available in the near future with the processing of the new NEEM ice core from the Northwestern part of the Greenlandic ice divide. Especially, a detailed study of the early Holocene will be of interest to see if the trend with the estimated temperature from the differential diffusion method is a real trend or just statistical fluctuation in the system.

In this thesis only three stable isotopes in oceanic water is mentioned, however oxygen has a rare third stable isotope ^{17}O which is now beginning to be measured in ice cores. A $^{17}O - excess$ has been defined by Landais et al. [2008],

$$^{17}O - excess \equiv \delta'^{17}O - 0.528\delta'^{18}O \ , \tag{9.1}$$

where δ' is the modified δ-fractionation:

$$\delta' \ln(\delta + 1) = \ln\left(\frac{R}{R_{ocean}}\right) \ . \tag{9.2}$$

It has been shown that the $^{17}O - excess$ is highly dependent on the moisture source [Landais et al., 2008]. If $^{17}O - excess$ can be measured in same resolutions as δ^{18}O and δD , a differential diffusion length based on ^{17}O

could be an additional parameter to estimating surface temperatures from diffusion processes. However, if one calculates the diffusion length using the fractionation found by Barkan and Luz [2007] is the difference between $\sigma_{^{17}O}$ and $\sigma_{^{18}O}$ is small. Hence the differential diffusion length based on ^{17}O may be defined as

$$\Delta\sigma_{17}^2 \equiv \sigma_{^{17}O}^2 - \sigma_D^2 \ , \tag{9.3}$$

in order to estimated by the methodes persented in this thesis.

10

Danish Summery - Dansk Resume

Iskapper fra både Antarktis og Grønland kan give indblik i fortidens klima ved at indeholde tidligere tiders sne i form af is. Denne information kan hentes frem ved at bore ned gennem iskappen og analysere iskerners kemiske og fysiske egenskaber. Et af de vigtigste parametre for at bestemme temperaturen tilbage i tiden ved borestedet er den stabile vand isotop oxygen-18, som kan sættes i direkte forbindelse med temperaturen i den sky, hvorfra sne er faldet. Denne temperaturafhængighed er imidlertid behæftet med en række usikkerheder.

I dette speciale testes en ny metode til at bestemme overflade temperaturen ved borestedet på baggrund af de to vand isotoper ^{18}O og deuterium. Metoden bestemmer overfladetemperaturen udfra diffusionssignalet af disse isotoper og ikke direkte udfra isotopsignalet. Dette kræver modeller for både transformationen fra sne til is, som sker i firn laget, is flydningen omkring borehullet og selve diffusionen af isotoperne i firn og is. Derudover skal metoder til at estimere diffusionsparametre i isen udvikles. Dette speciale omhandler disse fire områder.

På bagrund af de anvendte modeller og metoder, jf. ovennævnte problemstillinger, har det været muligt at bestemme overflade temperaturen fra 12 forskellige sektioner fra både GRIP og NGRIP iskernerne. Det begrænsede antal prøver, skyldes at deuterium ikke er målt i tilstrækkelig opløsning til at kunne bruges i denne type af undersøgelser. Overflade temperaturerne for de 12 prøver er blevet estimeret og sammenholdt med en kombineret borehuls- og isotoptemperatur rekonstruktion. De to temperaturerekonstruktioner stemmer overens.

Derved ses at metoden er istand til at kunne estimere overfladetemperaturen direkte fra diffusionsprocesserne, men den meget begrænsede datamængde,

som ligger til grund for verificeringen af metoden lægger op til, at der skal arbejdes videre med metoden så snart flere data er tilgængelige.

Appendices

A

Analysis and Data for the Flow model

This appendix deals with considerations of the inverse problem formulation for the flow model presented in Chapter 4. The forward algorithm is tested and the problems of not using the Occam's inversion a priori knowledge has been elaborated. The data set used in the inversion has also been listed in this appendix.

A.1 Testing the Forward Algorithm

In order to verify the forward algorithm and test its response to different scenarios the model have been run several times with different input param-

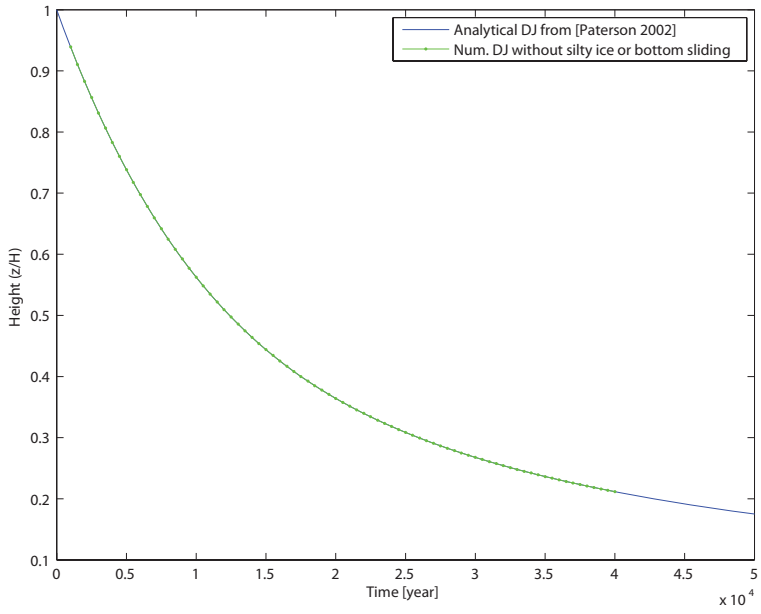

Figure A.1: Numerical vs. analytical DJ-model. In both calculations the bottom sliding and a silty layer is neglected. The Analytical DJ-model is derived by Paterson [2002, p. 278]

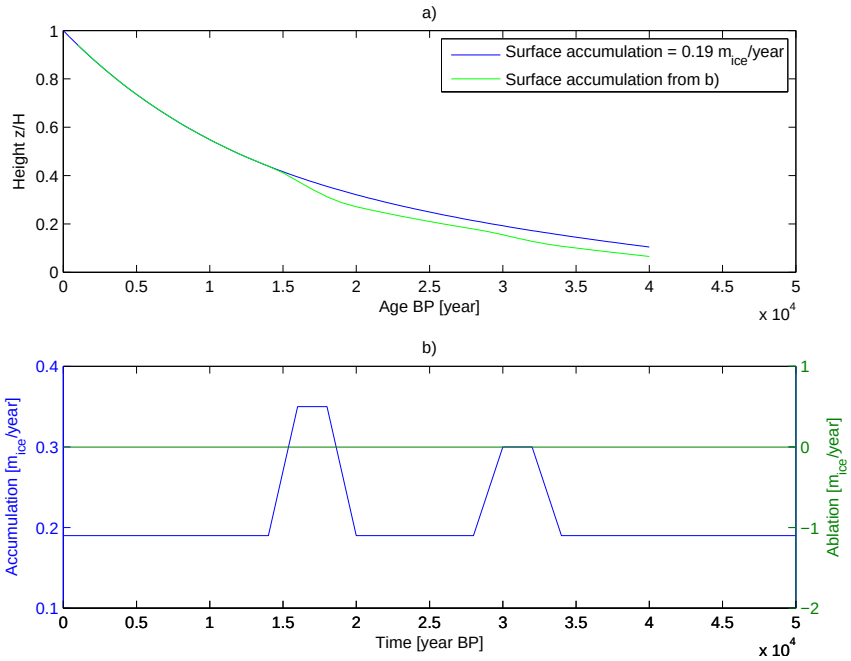

Figure A.2: Effect of Accumulation pattern on the predicted ages. The blue curve in a) is the ages with a constant accumulation of 0.19 $\frac{m_{ice}}{year}$ and the green curve is with an accumulation pattern depicted in b). The increased accumulation is resulting in younger ice deeper in the ice sheet, because the ice height is assumed to be constant.

eters.

Figure A.1 shows how the numerical forward model matches the analytical solution of the DJ-model given by Paterson [2002]. In the numerical solution the basal ablation, basal sliding and the silty layer thickness have all been neglected. Hence non of this are included in the analytical derived model by Paterson [2002]. The result of the comparison of the two models, emphasizes the forward models numerical capability of representing the DJ-flow model. In addition to the comparison with the analytical solution from Paterson [2002], two numerical experiments have been set up to test the forward modes response to changes in the climate parameters compared with a constant climate. Figure A.2 shows the models response to an increase in the accumulation over a time span, which reacts by speeding up the downwards motion and calculating a younger age at the a given age after the increase in accumulation. It is also seen how the model stabilizes when the accumulation is back at the present level. The opposite effect is seen in Figure A.3 where the surface elevation is increased over a time span and then decreased again, making the ice older at a certain depth after the elevation increase. Both of the responses are in consensus with the expected behavior of an ice sheet, which along with the a number of other trail runs give the imposition of a healthy forward algorithm to be used to estimating the age of a particle in a certain depth in the ice sheet.

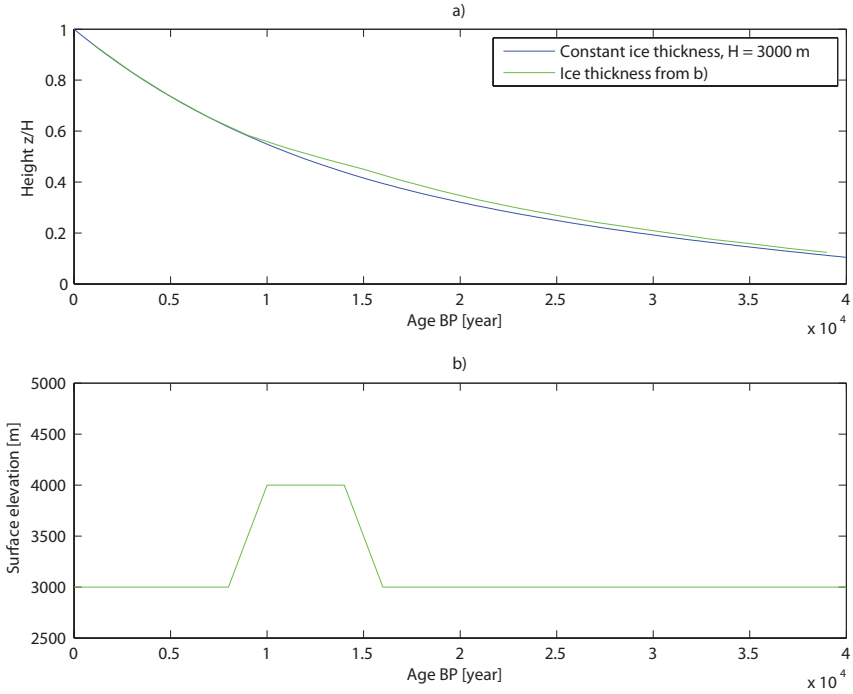

Figure A.3: In this run the ice height is suddenly increased by 1000 meter. Despite it being unrealistic this shows how the particles get older at a certain depth due to the increased ice thickness.

A.2 Inverse modelling with out Occam

As mentioned in Chapter 4 it was a naive hope that the Monte Carlo method could find a seemingly physical solution to the parameterizations of the flow model, with as little a priori information forcing of the system. But as seen in Figure A.4 the accumulation and surface elevation are cancelling

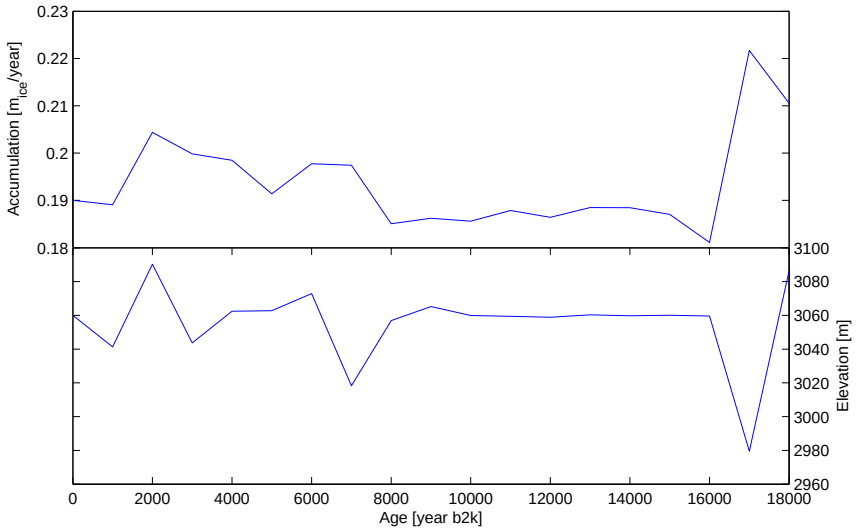

Figure A.4: Modelled accumulation and surface elevation without Occam. The anti-correlation is clearly seen in oldest part of the MC.

out the effect of each other, because of the strong physical coupling of the two parameters. Therefore the additional a priori information of the Occam inversion scheme, is needed in the Monte Carlo simulation of the flow and this additional information is used in Chapter 4 to predict the parameters determining the chronology seen at the NGRIP drill site.

A.3 NGRIP and NEEM Depth vs. Age Data

The depth-age data from GICC05 dating of the NGRIP ice core have been used to determine the age of radar echo layers seen in the transect between NGRIP and the new NEEM ice core. This data set provides a manageability depth-age record for the Monte Carlo inversion of the flow parameters of NGRIP done in Chapter 4 and are listed below.

AGE b2k	Depth NEEM	Depth NGRIP
1.3714566e+03	-3.2121489e+02	-2.7351481e+02
1.9492951e+03	-4.1602087e+02	-3.7215017e+02
2.3610659e+03	-4.8689324e+02	-4.4105746e+02
2.7334871e+03	-5.7464464e+02	-5.0078028e+02
3.1799343e+03	-6.1810865e+02	-5.7063037e+02
3.3476482e+03	-6.4512923e+02	-5.9662429e+02
3.5179277e+03	-6.7218893e+02	-6.2256159e+02
3.7921026e+03	-7.2625295e+02	-6.6382067e+02
3.9644185e+03	-7.4341449e+02	-6.8917918e+02
4.7682259e+03	-8.5409796e+02	-8.0226203e+02
5.0476411e+03	-8.9660946e+02	-8.3988447e+02
5.9170819e+03	-9.8285349e+02	-9.5518231e+02
6.2789879e+03	-1.0312744e+03	-1.0001937e+03
7.1046466e+03	-1.1175854e+03	-1.1014145e+03
7.4894323e+03	-1.1556186e+03	-1.1465460e+03
8.1636417e+03	-1.2293452e+03	-1.2219060e+03
8.5583922e+03	-1.2492346e+03	-1.2602852e+03
1.0161228e+04	-1.3438120e+03	-1.3961458e+03
1.1415554e+04	-1.3930701e+03	-1.4769922e+03
1.2574877e+04	-1.4337522e+03	-1.5173140e+03
1.4588612e+04	-1.4726011e+03	-1.5999221e+03

B

Diffusion lengths

In Section 7.2 the modelled diffusion lengths are compared to the found diffusion lengths using Burg's algorithm, but as mentioned in the section the two other power spectral density estimators have also been used to intrepid the ice diffusion found in the NGRIP ice core. Figure B.1 a. and b. show the model comparison of both the FFT method and the Autocorrelation method. The two Figures shows same overall picture as Figure 7.2 with different uncertainties depending on the data points involved in the power spectral density estimation.

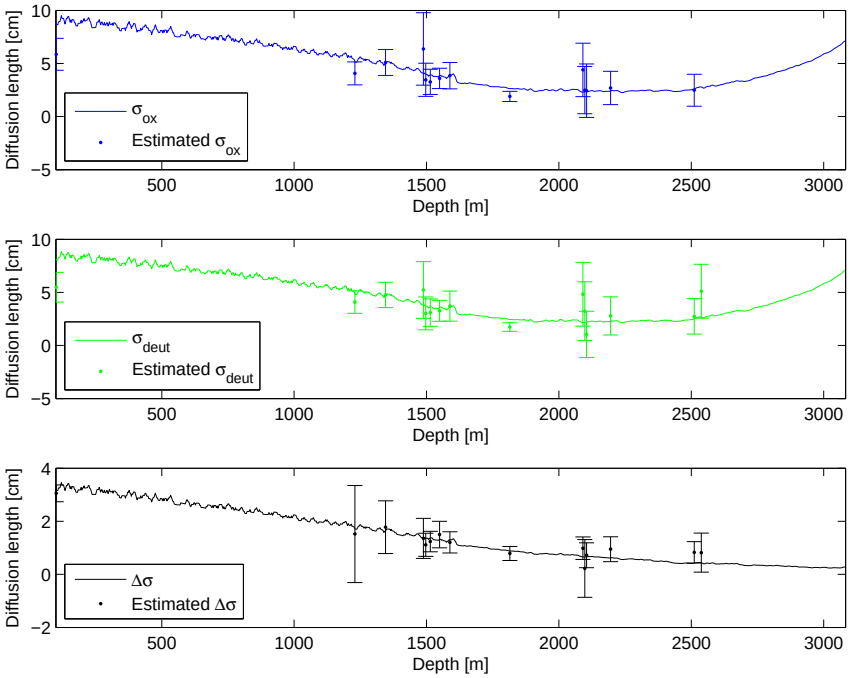

(a) FFT

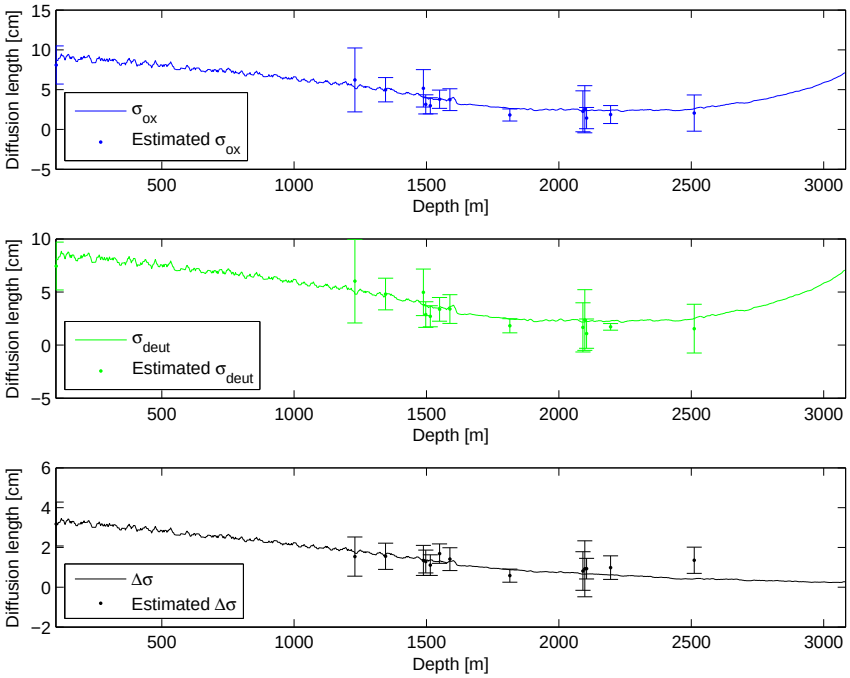

(b) Autocorrelation

Figure B.1: The found diffusion lengths using the a. FFT and b. Autocorrelation method are plotted on the NGRIIP depth scale against the modelled diffusion lengths from Chapter 5.

Bibliography

Alley, R. B. (1987). Firn Densification By Grain-Boundary Sliding: A First Model. *Journal De Physique*, Colloque C1, supplément au n3(48):249–256.

Andersen, N. (1974). On the Calculation of Filter Coefficients for Maximum Entropy Spectral Analysis. *Geophysics*, 39:69–72.

Arnaud, L., Lipenkov, V., Barnola, J. M., and Duval, P. (2000). Physical modeling of the densification of snow/firn and ice in theupper part of polar ice sheets. *Physics of Ice Core Records*, 159:285–305. Edited by T. Hondoh, Hokkaido University Press, Sapporo.

Arzt, E. (1982). Influence of an increasing particle coordination on the densificationof spherical powders. *ACTA METALLURG.*, 30(10):1883–1890.

Arzt, E. (1983). Practical application of hot-isostatic pressing diagrams: Four casestudies. *Metallurgical Transactions A*, 14:211–221.

Bamber, J. L., Layberry, R. L., and Gogineni, S. P. (2001). A new ice thickness and bed data set for the Greenland ice sheet.Measurement, data reduction, and errors. *Journal of Geophysical Research*, 106:33773–33780.

Barkan, E. and Luz, B. (2007). Diffusivity fractionations of $H_2^{16}O/H_2^{17}O$ and $H_2^{16}O/H_2^{18}O$ in air and their implications for isotope hydrology. *Rapid Communications in Mass Spectrometry*, 21(18):2999–3005.

Barnola, J. M., Pimienta, P., Raynaud, D., and Korotkevich, Y. S. (1991). CO_2-climate relationship as deduced from the Vostok ice core:are-examination based on new measurements and on a re-evaluationofthe air dating. *Tellus B*, 43 Issue 2:83–90.

Benson, C. S. (1969). *Stratigraphic studies in snow and firn, Greenland ice sheet*. SIPRE Res. Rep. 69. Chapter VI.

Boyle, E. A. (1997). Cool tropical temperatures shift the global δ^{18}O-T relationship: An explanation for the ice core δ^{18}O-borehole thermometryconflict? *Geophysical Research Letters*, 24:273–276.

Bracewell, R. N. (2000). *The Fourier Transform And Its Applications*. McGraw-Hill Higher Education.

Buchardt, S. L. and Dahl-Jensen, D. (2007). Estimating the basal melt rate at NorthGRIP using a Monte Carlotechnique. *Annals of Glaciology*, 45:137–142.

Burg, J. P. (1967). Maximum entropy analysis. In *37th Annual Meeting, Soc. Explor. Geophysics, Oklahoma City, Oklahoma*.

Cappa, C. D., Hendricks, M. B., DePaolo, D. J., and Cohen, R. C. (2003). Isotopic fractionation of water during evaporation. *Journal of Geophysical Research (Atmospheres)*, 108:4525–+.

Charles, C. D., Rind, D., Jouzel, J., Koster, R. D., and Fairbanks, R. G. (1994). Glacial-interglacial changes in moisture sources for greenland: Influenceson the ice core record of climate. *Science*, 263(5146):508–511.

Constable, S., Parker, R., and Constable, C. (1987). Occam's inversion: A practical algorithm for generating smooth modelsfrom electromagnetic sounding data. *Geophysics*, 52(3):289–300.

Craig, H. (1961a). Isotopic variations in meteoric waters. *Science*, 133(3465):1702–1703.

Craig, H. (1961b). Standard for reporting concentrations of deuterium and oxygen-18innatural waters. *Science*, 133(3467):1833–1834.

Cuffey, K. M. and Steig, E. J. (1998). Isotopic diffusion in polar firn: implications for interpretationofseasonalclimate parameters in ice-core records, with emphasisoncentral Greenland. *Journal of Glaciology*, 44:273–284.

Dahl-Jensen, D., Gundestrup, N., Gogineni, S., and Miller, H. (2003). Basal melt at NorthGRIP modeled from borehole, ice-core and radio-echosounder observations. *Annals of Glaciology*, 37(1):207–212.

Dahl-Jensen, D., Gundestrup, N. S., Miller, H., Watanabe, O., Johnsen, S. J., Steffensen, J. P., Clausen, H. B., Svensson, A., and Larsen, L. B. (2002). The NorthGRIP deep drilling programme. *Annals of Glaciology*, 35:1–4.

Dahl-Jensen, D., Mosegaard, K., Gundestrup, N., Clow, G., Johnsen, S. J., Hansen, A. W., and Balling, N. (1998). Past temperatures directly from the greenland ice sheet. *Science*, 282(5387):268–271.

Dansgaard, W. (1953). The abundance of 18O in atmospheric water and water vapor. *Tellus*, 5(4):461–469.

Dansgaard, W. (1964). Stable isotopes in precipitation. *Tellus*, 16:436–468.

Dansgaard, W., Clausen, H. B., Gundestrup, N., Hammer, C., Johnsen, S. F., Kristinsdottir, P. M., and Reeh, N. (1982). A new greenland deep ice core. *Science*, 218(4579):1273–1277.

Dansgaard, W., Johnsen, S., Clausen, H., and Gundestrup, N. (1973). Stable isotope glaciology. *Meddelelser om Grønland*, 197(2):1–53.

Dansgaard, W. and Johnsen, S. J. (1969). A flow model and a time scale for the ice core from Camp Century,Greenland. *Journal of Glaciology*, 8:215–223.

Dansgaard, W., Johnsen, S. J., Clausen, H. B., Dahl-Jensen, D., Gundestrup, N. S., Hammer, C. U., Hvidberg, C. S., Steffensen, J. P., Sveinbjornsdottir, A. E., Jouzel, J., and Bond, G. (1993). Evidence for general instability of past climate from a 250-kyr ice-corerecord. *Nature*, 364(6434):218–220.

Dansgaard, W., Johnsen, S. J., Moller, J., and Langway, C. C., J. (1969a). One thousand centuries of climatic record from camp century on thegreenlandice sheet. *Science*, 166(3903):377–380.

Dansgaard, W., Merlivat, L., and Roth, E. (1969b). Stable isotope measurements on firn cores. *Meddelelser om Grønland*, 177(2):62–76.

Ditlevsen, P. D., Kristensen, M. S., and Andersen, K. K. (2005). The Recurrence Time of Dansgaard-Oeschger Events and Limits on thePossible Periodic Component. *Journal of Climate*, 18:2594–2603.

EPICA Members (2004). Eight glacial cycles from an Antarctic ice core. *Nature*, 429:623–628.

Fisher, D. A., Reeh, N., and Clausen, H. B. (1985). Stratigraphic noise in the time series derived from ice cores. *Annals of Glaciology*, 7:76–83.

GICC05 (2005). The greenland ice core chronology 2005. Technical report, Centre for Ice and Climate, University of Copenhagen. Available at `http://www.iceandclimate.nbi.ku.dk/data/`.

Gouveia, W. and Scales, J. (1997). Resolution of seismic waveform inversion: Bayes versus Occam. *Inverse Problems*, 13(2):323–349.

Greve, R. (1997). Application of a polythermal three-dimensional ice sheet model tothe greenland ice sheet: Response to steady-state and transient climatescenarios. *Journal of Climate*, 10(5):901–918.

Hammer, C. (1980). Acidity of polar ice cores in relation to absolute dating, pastvolcanism, and radio-echoes. *Journal of Glaciology*, 25(93):359–372.

Herron, M. M. and Langway, C. C. (1980). Firn densification: An empirical model. *Journal of Glaciology*, 25(93):373–385.

Hooke, R. (2005). *Principles of Glacier Mechanics*. Cambridge University Press, Cambridge.

Huber, C., Leuenberger, M., Spahni, R., Flückiger, Jacquelineand Schwander, J., Stocker, T. F., Johnsen, Sigfus andLandais, A., and Jouzel, J. (2006). Isotope calibrated greenland temperature record over marine isotopestage3 and its relation to ch4. *Earth and Planetary Science Letters*, 243(3-4):504–519.

Hvidberg, C. S., Keller, K., Gundestrup, N. S., and Tscherning, C. C.and Forsberg, R. (1997). Mass balance and surface movement of the Greenland Ice Sheet atSummit,Central Greenland. *Geophysical Research Letters*, 24:2307–2310.

IPCC (2007). *Climate Change 2007: The Physical Science Basis. Contribution ofWorking Group I to the Fourth Assessment*. Cambridge University Press. Edited by S. Solomon, D. Qin, M. Manning, Z. Chen, M. Marquis, K.B.Averyt,M.Tignor and H.L. Miller.

Jaeger, J. C. (1969). *Elasticity, Fracture and Flow*. Methuen and Co.

Jean-Baptiste, P., Jouzel, J., Stievenard, M., and Ciais, P. (1998). Experimental determination of the diffusion rate of deuterated watervaporinice and application to the stable isotopes smoothing ofice cores. *Earth and Planetary Science Letters*, 158:81–90.

Johnsen, S., Dansgaard, W., and White, J. (1989). Origin of arctic precipitation under present and glacial conditions. *Tellus B*, 41.

Johnsen, S. J. (1977). Stable isotope homogenization of polar firn and ice. *Proc. Symp. on Isotopes and Impurities in Snow and Ice, I.U.G.G.XVI, General Assembly, Grenoble Aug. Sept. 1975*, pages 210–219. Washington 1977.

Johnsen, S. J. (2008). Personal communication.

Johnsen, S. J., Clausen, H. B., Cuffey, K. M., Schwander, G., and Creyts, T. (2000). Diffusion of stable isotopes in polar firn and ice: the isotope

effectinfirndiffusion. *Physics of Ice Core Records*, 159:121–140. Edited by T. Hondoh, Hokkaido University Press, Sapporo.

Johnsen, S. J., Dahl-Jensen, D., Dansgaard, W., and Gundestrup, N. (1995). Greenland palaeotemperatures derived from GRIP bore hole temperatureandicecore isotope profiles. *Tellus Series B Chemical and Physical Meteorology B*, 47:624–+.

Johnsen, S. J., Dahl-Jensen, D., Gundestrup, N., Steffensen, J. P., Clausen, H. B., Miller, H., Masson-Delmotte, V., Sveinbjörnsdottir, A. E., and White, J. (2001). Oxygen isotope and palaeotemperature records from six Greenland ice-corestations: Camp Century, Dye-3, GRIP, GISP2, Renland and NorthGRIP. *Journal of Quaternary Science*, 16:299–307.

Johnsen, S. J., Sveinbjörnsdóttir, A. E., Popp, T., White, J., Vinther, B. M., and Dahl-Jensen, D. (2006). Palaeotemperatures based on differential smoothing in isotopic firn diffusion. In *Geophysical Research Abstracts*, volume 8, page 10498.

Jouzel, J. (1999). Calibrating the isotopic paleonthermometer. *Science*, 286(5441):910–911.

Jouzel, J., Alley, R. B., Cuffey, K. M., Dansgaard, W., Grootes, P., Hoffmann, G., Johnsen, S. J., Koster, R. D., Peel, D., Shuman, C. A., Stievenard, M., Stuiver, M., and White, J. (1997). Validity of the temperature reconstruction from water isotopes inicecores. *Journal of Geophysical Research*, 102:26471–26488.

Jouzel, J. and Merlivat, L. (1984). Deuterium and oxygen 18 in precipitation: Modeling of the isotopiceffectsduring snow formation. *Journal of Geophysical Research*, 89(D7):11749–11758.

Kreyszig, E. (1999). *Advanced Engineering Mathematics 8th Edition*. John Wiley & Sons, Incorporated.

Landais, A., Barkan, E., and Luz, B. (2008). Record of $\delta^{18}O$ and ^{17}O-excess in ice from VostokAntarctica during the last 150,000 years. *Geophysical Research Letters*, 35:2709–+.

Lathi, B. (1998). *Signal Processing and Linear Systems*. Berkeley Cambridge Press, Carmichael.

Lauritzen, S. and Lundberg, J. (1999). Calibration of the speleothem delta function: an absolute temperaturerecord for the Holocene in northern Norway. *The Holocene*, 9(6):659.

Layberry, R. L. and Bamber, J. L. (2001). A new ice thickness and bed data set for the Greenland ice sheet2. Relationship between dynamics and basal topography. *Journal of Geophysical Research*, 106:33781–33788.

Leuenberger, M. C., Lang, C., and Schwander, J. (1999). Delta ^{15}N measurements as a calibration tool for the paleothermometerand gas-ice age differences: A case study for the 8200 B.P. eventon GRIP ice. *Journal of Geophysical Research*, 104:22163–22170.

Marple, S. L. (1987). *Digital Spectral Analysis*. Prentice-Hall, Englewood Cliffs.

Masson-Delmotte, V., Landais, A., Stievenard, M., Cattani, O., Falourd, S., Jouzel, J., Johnsen, S. J., Dahl-Jensen, D., Sveinsbjornsdottir, A., White, J. W. C., Popp, T., and Fischer, H. (2005). Holocene climatic changes in Greenland: Different deuterium excesssignalsat Greenland Ice Core Project (GRIP) and NorthGRIP. *Journal of Geophysical Research (Atmospheres)*, 110:14102–+.

Merlivat, L. (1978). Molecular diffusivities of $H_2^{16}O$, $HD^{16}O$, and $H_2^{18}O$ in gases. *J. Chem. Phys.*, 69(6):2864–2871.

Merlivat, L. and Jouzel, J. (1979). Global climatic interpretation of the deuterium-oxygen 18 relationshipfor precipitation. *Journal of Geophysical Research*, 84:5029–5033.

Moon, T. K. (1996). The expectation-maximization algorithm. *Signal Processing Magazine, IEEE*, 13(6):47–60.

Mosegaard, K. and Tarantola, A. (1995). Monte Carlo sampling of solutions to inverse problems. *Journal of Geophysical Research*, 100:12431–12448.

NGRIP Members (2004). High-resolution record of Northern Hemisphere climate extendinginto the last interglacial period. *Nature*, 431(7005):147–151.

Paterson, W. S. B. (2002). *Physics of Glaciers; Third edition*. Butterworth-Heinemann. Thrid edition 1994, reprinted with corrections 1998, 2001, 2002.

Popp, T. J. (2008). *The Speed and Timing of Climate Change: Detailed Ice Core Stable Isotope Records from NorthGRIP, Greenland and Mt. Moulton, West Antarctica*. PhD thesis, University of Colorado, Boulder.

Press, W. H., Teukolsky, S. A., Vetterling, W., and Flannery, B. P., editors (2007). *Numerical Recipes - The Art of Scientific Computing*. Cambridge University Press, Cambridge, third edition.

Ramseier, R. O. (1967). Self-diffusion of tritium in natural and synthetic ice monocrystals. *Journal of Applied Physics*, 38(6):2553–2556.

Reeh, N. (1988). A flow-line model for calculating the surface profile and the velocity,strain-rate, and stress fields in an ice sheet. *Journal of Glaciology*, 34:46–54.

Schwander, J., Sowers, T., Barnola, J.-M., Blunier, T., Fuchs, A., and Malaizé, B. (1997). Age scale of the air in the summit ice: Implication for glacial-interglacialtemperature change. *Journal of Geophysical Research*, 102(D16):19483–19494.

Schwander, J., Stauffer, B., and Sigg, A. (1988). Air mixing in firn and the age of the air at pore close-off. *Annals of Glaciology*, 10:141–145.

Severinghaus, J. P., Sowers, T., Brook, E. J., Alley, R. B., and Bender, M. L. (1998). Timing of abrupt climate change at the end of the younger dryas intervalfromthermally fractionated gases in polar ice. *Nature*, 391(6663):141–146.

Shackleton, N. and Opdyke, N. (1973). Oxygen isotope and paleomagnetic stratigraphy of equatorial Pacificcore V28-238: oxygen isotope temperatures and ice volumes on a 105 year and 10 6 year scale. *Quaternary Research*, 3(1):39–55.

Solgaard, A. M., Hvidberg, C. S., Clausen, H. B., and Reeh, N. (2007). An ice flow model of hans tausen ice cap, north greenland. *Geophysical Research Abstracts*, 9:07701.

Spiegel, M. and Liu, J., editors (1999). *Mathematical Handbook of Formulas and Tables*. McGraw-Hill, New York.

Steen-Larsen, H. C. (2007). A general procedure to infer surface and basal mass balance forminternal layering in an ice sheet and an application to the greenlandicesheet. Master thesis, University of Copenhagen.

Steen-Larsen, H. C., Waddington, E. D., and Koutnik, M. R. (2008). Formulating an inverse problem to infer the accumulation-rate patternfrom deep internal layering in an ice sheet using a monte carlo approach. *Journal of Glaciology*, In Press.

Steffensen, J. P., Andersen, K. K., Bigler, M., Clausen, H. B., Dahl-Jensen, D., Goto-Azuma, H. F. K., Hansson, M., Johnsen, S. J., Jouzel, J., Masson-Delmotte, V., Popp, T., Rasmussen, S. O., Röthlisberger, R., Ruth, U., Staufferand, B., Siggaard-Andersen, M.-L., Sveinbjörnsdóttir, A. E., Svensson, A., and White, J. W. C. (2008). High-resolution greenland ice core data show abrupt climate changehappensin few years. *Science*, 321(5889):680–684.

Tarantola, A. (2004). *Inverse Problem Theory and Methods for Model Parameter Estimation*. SIAM: Society for Industrial and Applied Mathematics.

Taylor, J. R. (1996). *An Introduction to Error Analysis: The Study of Uncertainties inPhysical Measurements*. University Science Books.

Vinther, B. M., Buchard, S. L., Clausen, H. B., Dahl-Jensen, D., Johnsen, S. J., Fisher, D. A., Koerner, R. M., Raynaud, D., Lipenkov, V., Andersen, K. K., Blunier, T., Rasmussen, S. O., Steffensen, J. P., and Svensson, A. M. (2008a). Significant holocene thinning of the greenland ice sheet. *In Preparation*.

Vinther, B. M., Clausen, H. B., Fisher, D. A., Koerner, R. M., Johnsen, S. J., Andersen, K. K., Dahl-Jensen, D., Rasmussen, S. O., Steffensen, J. P., and Svensson, A. M. (2008b). Synchronizing ice cores from the renland and agassiz ice caps tothe greenland ice core chronology. *Journal of Geophysical Research*, 113(D8).

Waddington, E. D., Neumann, T. A., Koutnik, M., Marshall, H.-P., and Morse, D. L. (2007). Inference of accumulation-rate patterns from deep layers in glaciersand ice sheets. *Journal of Glaciology*, 53(183):694–712(19).

Werner, M., Heimann, M., and Hoffmann, G. (2001). Isotopic composition and origin of polar precipitation in presentand glacial climate simulations. *Tellus Series B Chemical and Physical Meteorology B*, 53:53–+.

Whillans, I. M. and Grootes, P. M. (1985). Isotopic diffusion in cold snow and firn. *Journal of Geophysical Research*, 90:3910–3918.

Zwally, H. J. and Jun, L. (2002). Seasonal and interannual variations of firn densification and ice-sheetsurface elevation at the greenland summit. *Journal of Glaciology*, 48:199–207(9).

List of Figures

List of Tables

Nomenclature

Atm Atmospheric pressure, page 46

b2k Before year 2000, page 11

BA Bølling/Allerød, page 4

bp Before present, page 4

DEM Digital Elevation Model, page 26

DJ The Dansgaard-Johnsen Flow Model, page 22

DOF Degrees of Freedoms, page 62

ECM Electrical Conductivity Measurement, page 4

EM Expectation maximization, page 36

GCM General Circulation Model, page 10

GI Greenland Interstadials, page 4

GICC05 Greenland Ice Core Chronology 2005, page 3

GISP2 The Greenland Ice Sheet Project, page 1

GRIP Greenland Ice Core Project, page 1

GS Greenland stadia, page 4

HL The Herron-Langway-model of densification, page 15

IPCC The Intergovernmental Panel on Climate Change, page 1

IS Interstadial also abbreviated GI, page 61

kyr Kilo year, page 1

LGM Last Glacial Maximum, page 4

MEM Maximum Entropy Method, page 50

NEEM The North Greenland Eemian Ice Drilling, page 1

NGRIP North Greenland Ice Core Project, page 1

SMOW Standard Mean Ocean Water, page 5

YD Younger Dryas, page 4